Two-photon absorption laser induced fluorescence on carbon monoxide for spatially resolved temperature measurements

van de Steeg, Alex W.

Award date:
2018

Technische Universiteit
Eindhoven
University of Technology

/ Faculteit
Technische Natuurkunde
Postbus 513
5600 MB Eindhoven

/ Faculteit Technische Natuurkunde

Technische Universiteit
Eindhoven
University of Technology

Two-Photon Absorption Laser Induced Fluorescence on Carbon Monoxide

For spatially resolved temperature measurements

A.W. van de Steeg
PMP 18-01
January 2018

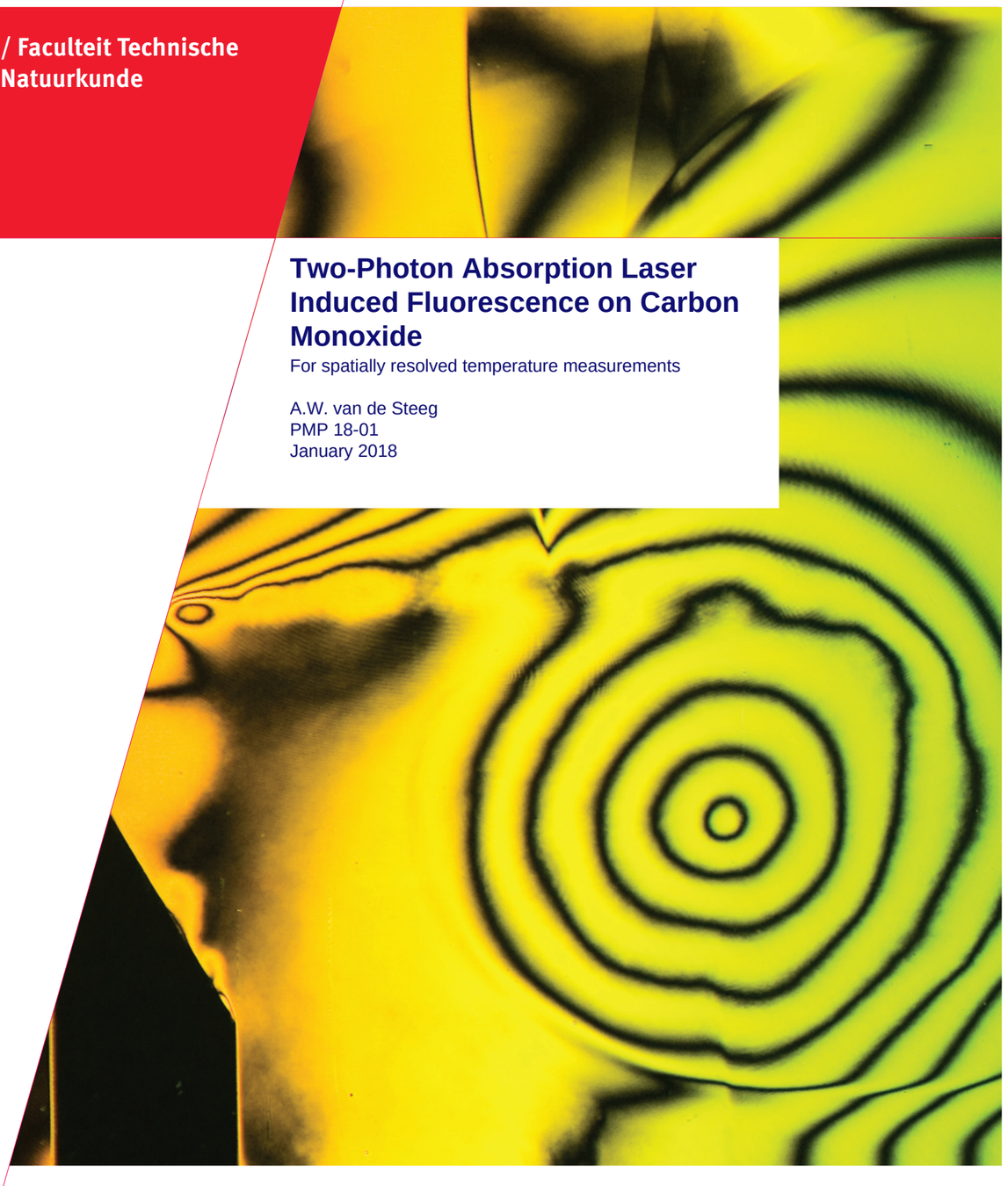

Where innovation starts

Two-photon Absorption Laser Induced Fluorescence on Carbon Monoxide

For spatially resolved temperature measurements

A.W. van de Steeg

January 2018 PMP 18-01

Under supervision of:

M.A. Damen, M.Sc.

Dr. R. Engeln

Abstract

The aim of this study is to measure the temperature of CO using two-photon absorption laser induced fluorescence (TALIF). This work is performed to study the dissociation of CO_2 to CO. This dissociation process is researched with the underlying idea to create renewable fuels from CO_2 and water, in order to solve the intermittency problem of renewable energy.

In the TALIF process two photons with the same energy get absorbed simultaneously by a molecule, thereby exciting this molecule. These molecules then de-excite, thereby emitting fluorescence. The combined energy of the photons must match the energy of an electronic transition in CO. Multiple electronic transitions were considered, however one was chosen due to its better characterization in literature. The theory of two-photon absorption is studied, which is then applied to create a simulation of the excitation spectrum of CO belonging to the chosen electronic level. In order to compare and validate the simulations of the excitation spectrum with experiments a working TALIF setup was built.

This setup couples a frequency tripled Nd:YAG laser into a dye laser, which emits laser light at 460nm. The 460nm light is frequency doubled to 230nm. This light is attenuated and subsequently focused into a reactor. The emitted fluorescence is imaged in a fiber at a 90° angle from this laser beam. This fiber is coupled into a photomultiplier tube.

Before the created simulation can be fitted to measurements several properties had to be researched and validated. At first, operation in the linear fluorescence regime was verified. Secondly it was found that the dye-laser does not scan reproducibly, which was resolved through a polynomial correction of the wavelength axis. The laser linewidth is included as a fitting parameter, since it does not follow the specifications of the laser. Finally both experimental data measured and data from literature are fitted to the simulation. For both cases the temperature follows within reasonable accuracy.

Acknowledgements

This work is mainly made possible due to the excellent supervision of Mark and Richard. This work was also greatly enhanced by the excellence of the technicians of PMP, mainly Janneke, for which I want to thank her. Furthermore I want to thank Marija for listening to my endless stream of complaints and problems during the long hours spent in the lab, as well as providing me with a much needed cup of coffee very often. Bart provided a very steady stream of good suggestions, which I could use for improving both my Matlab skills as well as the experimental setup. Finally I want to thank my friends and family for providing a lot of support during the sometimes tough phases of this project. Drinking coffee with Niek while both talking about our projects was a welcome refuge from the lab a lot of times. Sitting in a bar with Loek to talk about anything and everything was always awesome, and helped me put my mind at rest during the weekends. All in all I'm very satisfied with this work, which would not have been possible without the direct or indirect assistance of all the people involved.

Contents

1. Introduction

The motivation of this work lies in the field of climate change and renewables. Renewable energy sources are intermittent, and thus not constant in time, which poses a problem. This can among others be resolved by creating solar fuels. Therefore, next to a more detailed motivation, this chapter gives a brief introduction into these solar fuels. Furthermore an introduction is given into laser spectroscopy methods, which can be used to study the production of these fuels. Finally, this chapter details the aim of this study as well as a brief outline of the chapters it contains.

1.1 Motivation

Human accelerated climate change is one of the biggest challenges facing the world at this moment [1]. Climate change not only means the rising of average temperatures globally, it also causes for instance changes in weather patterns [2], giving longer periods of rain or draught. Extreme weather effects, such as hurricanes, will occur more often and be more powerful [3]. The rise in average temperature also means more ice will be lost in both polar regions, increasing the sea levels globally, leaving large areas at risk of flooding [4]. All these changes also mean more arable land is lost, leading to a scarceness of food [5].

Climate change is mainly driven by the emission of greenhouse gases, most notably CO_2, which is released when fossil fuels are burned [6]. The largest part of the global energy production relies on fossil fuels [7], thereby emitting large quantities of CO_2 into the atmosphere [8]. CO_2 absorbs radiation in the infrared very efficiently [9], therefore sunlight that has been reflected on earth's surface is absorbed by the CO_2 in the atmosphere, whereupon the radiation is re-emitted in all directions. This causes more energy to be retained on earth, thereby increasing the total energy and thus temperature on Earth. This correlation between CO_2 and global temperature is illustrated in Figure 1.

Figure 1a shows the global average temperature anomaly over the last decades, illustrating a rising global temperature. Figure 1b shows the amount of CO_2 in the atmosphere over a period of time. Large parts of the world have industrialized rapidly over the last decades, causing the rapid growth of the CO_2 density [10][11]. The two rising trends hint at a correlation between CO_2 concentration in the atmosphere and global average temperature. While these figures only show the possibility of a connection between CO_2 concentration and temperature, there is a broad consensus in the scientific world that this correlation actually exists [12].

The acceptance of human accelerated climate change due to the emission of greenhouse gases has increased over the past years [13]. This awareness, together with the will to combat climate change, have led to the Paris Agreement. In Paris, 2015, at the United Nations Climate Change Conference, 197 countries committed themselves to the energy transition [14]. This Paris Agreement states that the world has to reduce its reliance on fossil fuels by changing to different energy sources, emphasizing the use of renewables such as solar and wind energy. The goal of the agreement is to limit the global average temperature change to a maximum of 2°C [15].

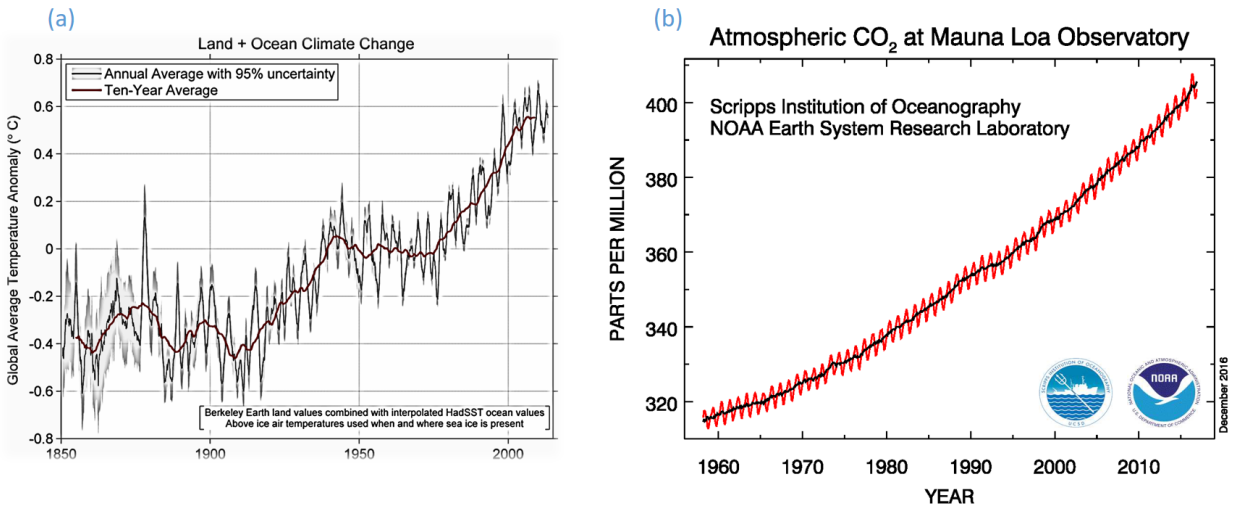

Figure 1 (a) Average land temperature anomaly as computed by Berkeley Earth through the Berkeley Earth Global Temperature index, 1850 to present. Figure taken from: http://berkeleyearth.org/land-and-ocean-data/ (12-13-2016). (b) Carbon dioxide concentration measured at Mauna Loa Observatory. Figure taken from National Oceanic & Atmospheric Administration, Earth System Research Laboratory, US Department of Commerce, https://www.esrl.noaa.gov/gmd/ccgg/trends/full.html (12-13-2016)

Several energy sources do not rely on fossil-fuels, and could be used as energy sources without greenhouse gas emission. There is nuclear fusion, nuclear fission and other renewable energy sources, most notably solar and wind energy. Nuclear fusion is still in the research phase, therefore not applicable at this point [16][17], however when it becomes available it provides a clean near-infinite energy source [18]. It is expected to take several decades before nuclear fusion becomes commercially available [19]. Nuclear fission however is already a commercial energy source. It does bring significant drawbacks, even though it provides around 11% of the global energy demand [20][21]. One major drawback is safety, Chernobyl and Fukushima have shown the dangers of nuclear fission [22]. A second large drawback is waste storage, nuclear waste remains dangerous for a long time, and storing it safely poses a big challenge [23]. Thirdly there is the reliance on other scarce resources. Where nuclear fusion relies on the near-infinite hydrogen, nuclear fission relies on uranium. It is estimated the uranium stock will only last for approximately 120 years [24]. The drawbacks of fission, and the unavailability of fusion rule out both nuclear options as solutions for the imminent energy transition.

Other emission-free energy sources which can be used for the energy transition are for example solar and wind energy. It is illustrative to compare the energy potential of these sources, shown in Figure 2. By far the most energy rich renewable is solar energy. The total average power of the sun on earth provides the world with approximately 1500 times more energy than the total global energy demand [25]. Other promising renewable energy sources are wind and hydropower, however their capacities are much less than that of solar energy. This figure is also illustrative of the finiteness of fossil fuels and nuclear fission.

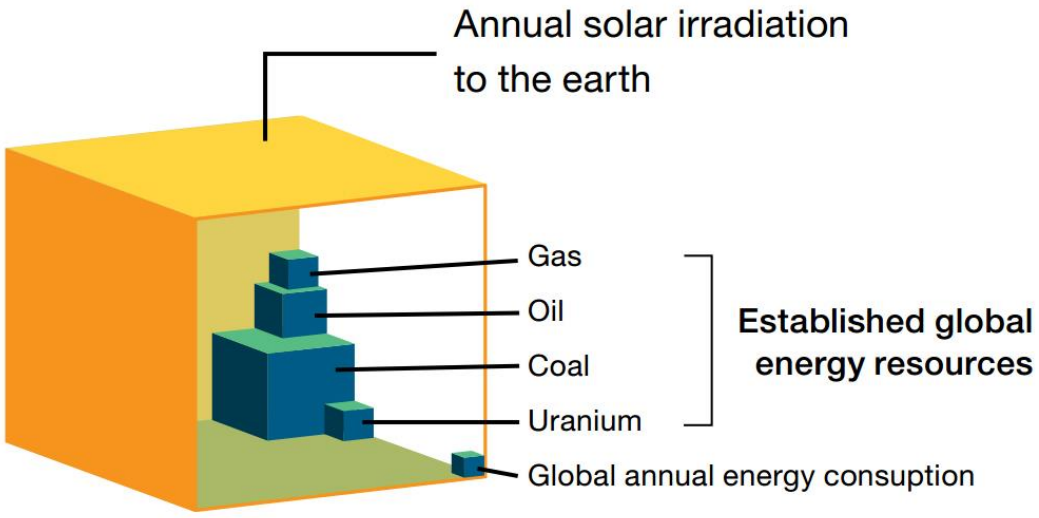

Figure 2 Energy potential of different energy sources, indicated in different cubes. The overlapping cube represents the annual solar irradiation to earth. Picture taken from: Eco Solar Equipment Ltd [26]

This figure shows that solar energy is a very promising option for the energy transition. Some countries are investing heavily in energy transition, since the dangers of climate change are becoming more apparent by the year [27][28]. Two such countries are Germany and China. Germany has committed itself to renewables, and therefore relies for almost 30% of its energy production on solar and wind energy [29]. China however experiences the negative effects of pollution more and more due to its rapid industrialization [30]. To tackle this the government is investing heavily in renewables [31], making China the biggest producer of renewable energy globally [32]. Figure 3 illustrates the production of solar energy in different parts of the world over time, showing the rapid growth of solar energy production.

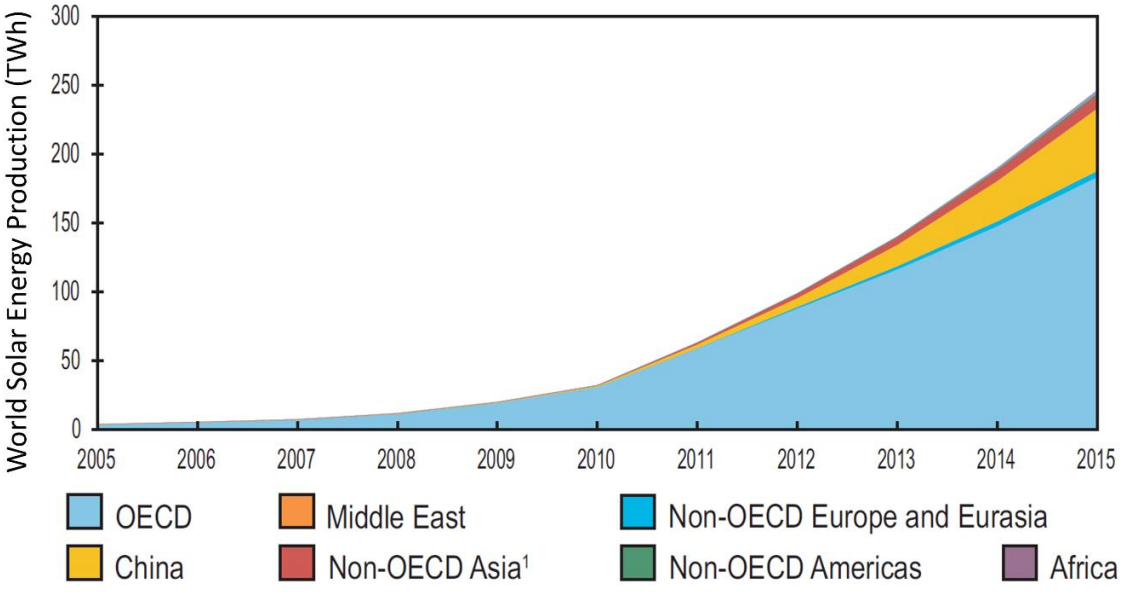

Figure 3 Total production of solar energy by region, over a time period, measured in TWh. Picture taken from International Energy Agency, "Key World Energy Statistics," 2017 [32]

Even though there is a global increase in the production of fossil-free energy, there are drawbacks. One of the major drawbacks that comes with the use of green energy sources is that they are intermittent. This means that neither the production of solar, nor that of wind energy is constant in time [33]. Intermittency makes these energy sources too unreliable to power significant portions of the world without any means to store the produced energy [34]. There is a certain point where large scale energy storage solutions have to be implemented as the reliance on intermittent energy sources grows [35]. Currently, no efficient large scale methods for energy storage are available, however different technologies are studied, with one of the most obvious storing energy in batteries.

Using batteries to store energy in a large scale brings significant drawbacks [36]. Batteries are environmentally unfriendly to produce and they require scarce elements. Another drawback is the low energy density of batteries, illustrated in Figure 4. This figure shows the energy densities of different types of batteries, together with those of regular fuels. The energy density of batteries is an order of magnitude smaller than that of regular fuels. A different solution to the intermittency problem is the production of solar fuels, a process that creates new hydrocarbons out of CO_2.

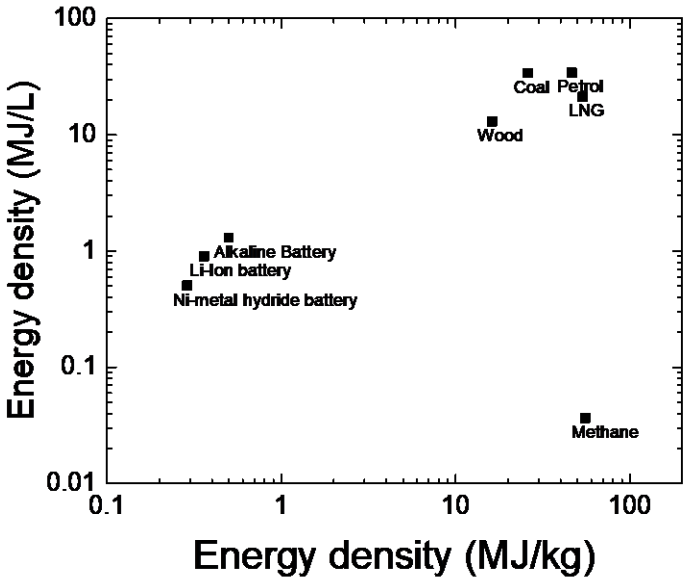

Figure 4 Energy densities of three kinds of batteries compared to different hydrocarbon fuels. Data from: [37][38]

1.2 Solar fuels

In Figure 5 the CO_2 cycle of solar fuels is shown. Renewable energy is used to convert CO_2 into hydrocarbons. The used carbon is re-emitted when the created hydrocarbons are burned to release their stored energy. The hydrocarbons are created in a liquid form, thus they can easily be stored and processed through an infrastructure already in place. This process is CO_2 neutral, since all of the carbon that is emitted in the cycle can be used to create new fuels.

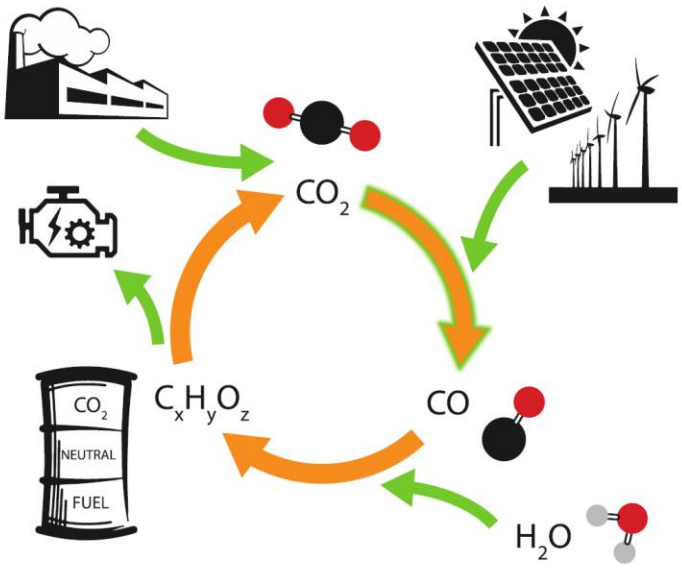

Figure 5 Solar fuel cycle, starting from CO_2; CO_2 is dissociated into CO using green energy. Further processing of the CO, together with H_2O results in new fuels, which can then be used as regular fossil fuel.

As a solution to the intermittency problem solar fuels have significant advantages over batteries. One of the biggest advantages is that the world currently already runs on hydrocarbons, namely fossil fuels. Therefore if solar fuels would come to the market, the current infrastructure can still be used. A second advantage of solar fuels is that hydrocarbons have a much higher energy density than batteries [39], which was illustrated in the previous section.

The production of new hydrocarbons starts with the dissociation of CO_2 to CO. The CO is then combined with water in the Fischer-Tropsch process to create liquid hydrocarbons [40]. The dissociation of carbon dioxide to carbon monoxide is one of the most energy demanding as well as one of the least understood steps in the solar fuel cycle [41], therefore a lot of the research done on solar fuels goes into the dissociation of CO_2.

Dissociation of CO_2 to CO is a highly endothermic process [42], which requires temperatures of several thousand K in regular thermal processes [43]. Therefore an environment that more easily allows for this process to happen is searched for. A plasma, or gas discharge, is considered as such an environment. A plasma is an ionized gas, therefore ions, electrons and radicals are present [44]. Due to the presence of these species a different chemistry can occur that would not happen in a normal gas, such as the dissociation of CO_2 into CO.

There are multiple pathways through which the dissociation of CO_2 to CO can occur [45]. Two of these pathways are discussed, direct electron impact and vibrational pumping. Figure 6 illustrates these two pathways through the potential diagram of CO_2. CO_2 is dissociated by direct electron impact when a high-energy electron of the plasma collides with the CO_2 molecule. This is an almost instantaneous process, which means no change in the distance between the different atoms is possible. This process is therefore illustrated by a vertical arrow in Figure 6. Due to the potential curves of the involved species, CO and excited atomic oxygen are produced. Excess energy is released as heat when the atomic oxygen relaxes to the ground state. This therefore leads to an inefficient process, which can only occur through collisions with electrons having more than 7eV [46].

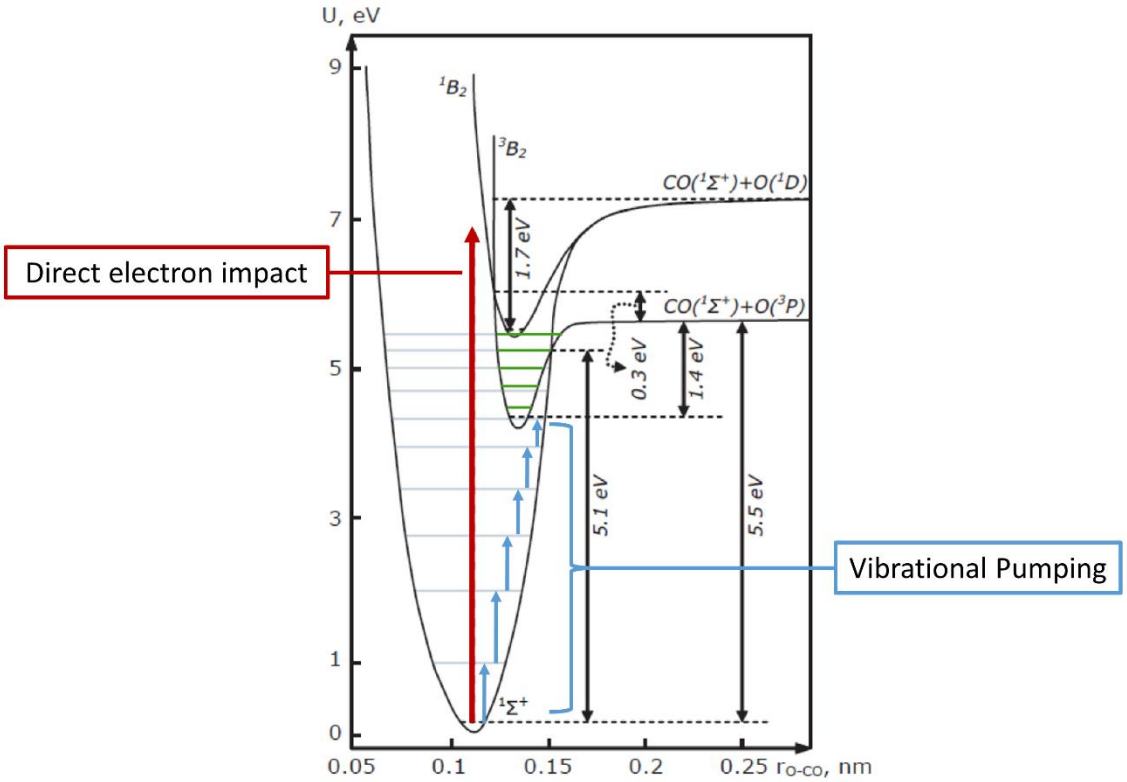

Figure 6 Potential curves of CO_2 and CO with arrows indicating the processes of direct electron impact (red) and vibrational pumping (blue).

Vibrational pumping, shown on the right of Figure 6, is a process where low-energy electrons, in the range of 1-2eV vibrationally excite the CO_2 stepwise. Once a high enough excitation level is reached the potential curves of CO_2 and the dissociation products start to overlap, at which point they can dissociate. This process does not create species in excited states, making the process more efficient then direct electron impact [46]. Dissociation though a combination of the two processes is also possible. The CO_2 is vibrationally excited by a low-energy electron and subsequently dissociated through direct electron-impact. This process is more efficient than dissociation by one high-energy electron.

The dissociation of CO_2 to CO has been studied quite extensively, however attempts at creating a process with both a high dissociation degree and high efficiency have been relatively unsuccessful, which is illustrated in Figure 7. This figure shows the energy efficiency as a function of the conversion rate for different experiments using different reactor types and geometries. It is possible to obtain either a high energy efficiency, or a high conversion rate. A high energy efficiency can be reached when the total energy put into each converted molecule is exactly tailored to the dissociation energy. A high conversion rate can be obtained by having a large amount of energy put into each molecule to convert as much molecules as possible. Generally speaking a large power input gives a high temperature, which results in a high dissociation degree due to mostly thermal processes. The benchmark to compare plasma processes with is given by the maximum thermal efficiency. This is the maximum efficiency that can be obtained by heating CO_2, which can be computed to be a little more than 45% [47][48]. Any efficiency obtained below this threshold can be explained by purely thermal chemistry.

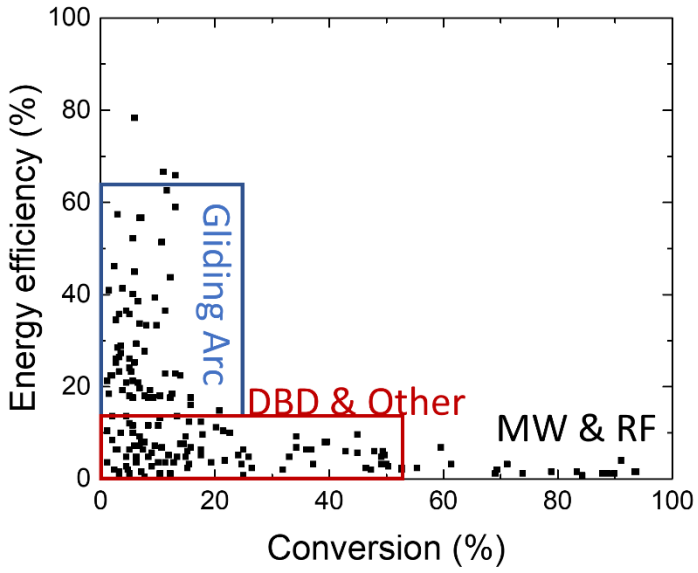

Figure 7 Energy efficiency of the dissociation of CO_2 versus the conversion rate (amount of CO_2 dissociated to the total amount of CO_2). Data points compiled from different experiments. Data from [47].

Many different discharge types and geometries have been used to obtain these results. The dielectric barrier discharge (DBD) was one of the first reactor types to be studied for solar fuel research, since it is applied in ozone production [49]. The DBD gives too low energy efficiencies to be applied industrially. Currently multiple other plasma types are being researched, the glow, gliding arc and microwave discharges.

A glow discharge operates at low pressure and has a low gas throughput, however for studies on vibrational kinetics in a plasma it is suitable [47], since it is a very uniform discharge. The gliding arc reportedly has a very good dissociation efficiency, which is why it has gained attention in recent years [50]. The highest reported efficiency and throughput has been reported in the microwave discharge [51]. To study the dissociation of CO_2 in any of these types of discharges it is vital to have a diagnostic to measure the production of CO. The following section gives a brief introduction into the diagnostic applied for this purpose.

1.3 Plasma Diagnostics

There are several criteria that have to be met when selecting a diagnostic to study the production of CO for the production of solar fuels. Firstly, the diagnostic must have spatial resolution, due to the non-uniformity of most discharges. Secondly it must be non-intrusive, and thirdly it needs to be applied *in-situ*.

These three requirements rule out conventional diagnostics that are applied to plasmas, such as probes. Probes are ruled out since they are inherently intrusive. Another frequently applied diagnostic, optical emission spectroscopy, only detects emission in the visible regime. Emission in this wavelength range is not guaranteed for the species of interest. Infrared absorption is a technique frequently applied to study plasmas, however it generally concerns line-of-sight measurements [52]. Therefore it lacks the required spatial resolution. A possible diagnostic is therefore searched in the category of laser diagnostics.

Laser induced fluorescence (LIF) would be a perfect option for studying the production of CO, since it provides spatial resolution, as well as information on the temperatures involved. Next to that when applied carefully it is non-intrusive, and it is inherently *in-situ* [53]. The only problem with using one-photon LIF on CO is that the excited electronic singlet states of CO lie in the vacuum ultraviolet (VUV) [54]. Theoretically one-photon LIF would still be applicable, it just makes it experimentally challenging. A way to circumvent this is by using two-photon absorption laser induced fluorescence (TALIF). Two photons simultaneously excite the CO, where both photons have an energy below the VUV threshold. TALIF therefore is the diagnostic applied in this study.

1.4 Aim of this study

Information on temperature is a requirement when applying TALIF to measure densities. Obtaining temperatures using TALIF is therefore the focus of this work. The goal of this study is to develop a working TALIF setup which can measure excitation spectra, and to create a simulation to compute these spectra. The computed excitation spectrum can then be fitted to the experimental data to give temperatures.

1.5 Outline

This study concerns CO, which is a diatomic molecule. Therefore in the first sections, of the next chapter, sections 2.1 and 2.2, the theory of rotations, vibrations and transitions in diatomic molecules is treated. Subsequently a mathematical evaluation of the theory of one-photon LIF is given, starting with the three level scheme in section 2.3. From the three-level scheme the theoretical fluorescence yield and detected signal can be computed, detailed in section 2.4 and 2.5. The theory is then expanded upon to include two-photon processes in section 2.6. The theory chapter ends with a brief explanation of Kasha's rule in section 2.7 and the explanation of the two relevant types of spectra in this work, given in section 2.8.

Chapter 3 focuses on the spectrum of CO. In section 3.1 different possible excitation schemes for TALIF on CO are studied. Two of these are then singled out and compared. Finally one excitation scheme is chosen to work with in the remainder of this work. For a better understanding of the diagnostic a simulation is developed in sections 3.2 and 3.3. Section 3.2 starts by calculating the excitation spectrum of the chosen scheme. Section 3.3 then further builds upon this to calculate the complete fluorescence spectrum as emitted CO for a fixed excitation wavelength.

Chapter 4 discusses the experimental setup that is used in these experiments, as well as the measurement procedure. The experimental setup is split into two sections, section 4.1 and 4.2. The first section focuses on the generation of the excitation pulse and section 4.2 focuses both on the detection of the fluorescence as well as the vacuum system. Finally the applied procedure to measure an excitation spectrum is discussed in section 4.3.

Data analysis in TALIF is considered in chapter 0. The simulation created in section 3.2 is transformed into a Matlab function. This simulation can be fitted to measured data to obtain the temperature. However there are several things that have to be verified before this can be applied. Section 5.1 starts by a calibration of the laser wavelength, which is followed in 5.2 by a consideration of the laser linewidth. In section 5.3 the linearity of the system is validated, and in section 5.4 the option of a bandpass filter is studied. Finally in the last section 5.5, the fitting process is tested on an actual measurement, as well as on data taken from literature.

The last chapter, chapter 6, gives the conclusions and an outlook. The outlook concerns possible improvements to the experimental setup as well as future measurements.

2. Theory

The general theory of laser induced fluorescence and diatomic molecules is treated in this chapter. Carbon-monoxide, which is the molecule studied in this work, is a diatomic molecule. Therefore the rotational and vibrational structure of these molecules is discussed. This theory is then extended to include transitions. A mathematical treatment of LIF starts by the evaluation of a three-level scheme. Further evaluation of this three-level scheme gives the fluorescence yield. All of these theoretical component are finally combined in the theory of two-photon LIF. A last theoretical aspect detailed in this chapter are the two different types of spectra which are relevant for this work.

2.1 Rotational and vibrational states in diatomic molecules

This study details two-photon LIF on CO, which is a diatomic molecule. Compared to atomic species the spectra of diatomic molecules is more complex due to the existence of vibrational and rotational states which further subdivides electronic levels [55]. The structure of rotations and vibrations in diatomic molecules is therefore treated in this section.

2.1.1 Rotational states

A rigid diatomic molecule, such as CO, can rotate around any axis through the center of mass. The rotational energy of such a system can be expressed as [56]

$$E_{rot} = \frac{J(J+1)\hbar^2}{2MR^2}. \quad (1)$$

In this equation *J* is the rotational quantum number, with $|J|^2 = J(J+1)\hbar^2$, where *J* can only have discrete values, *M* is the reduced mass, $M = \frac{M_A M_B}{M_A + M_B}$, with M_A and M_B the mass of the two atoms, and R is the internuclear distance. This equation holds for a rigid situation, where the internuclear distance is constant. However in reality the internuclear distance is not constant in time, with an equilibrium position of R_e. To find an expression for the variation of R around its equilibrium, the centrifugal force, $F_c = -M\omega^2 R$, has to be considered. This force has to be compensated by the restoring force, $F_r = -dE_{pot}/dR$, holding the atoms together. Around the equilibrium, R_e, the potential energy function, E_{pot}, can be approximated by a parabolic function. This leads to a linear restoring force, given by $F_r = -k(R - R_e)\hat{R}$. Equating these forces gives

$$M\omega^2 R = \frac{J(J+1)\hbar^2}{MR^3} = k(R - R_e). \quad (2)$$

This is simply writing the centrifugal force down and equating it to the restoring force, which is given by the parabolic potential. This can further be rewritten to:

$$R = R_e + \frac{J(J+1)\hbar^2}{MkR_e^3} = R_e(1 + x) \quad (3)$$

with $x = \frac{J(J+1)\hbar^2}{MkR_e^4} \ll 1$. This can be interpreted as the internuclear distance being changed by the molecular rotation. This leads to an additional term for the rotational energy, which is determined by the parabolic potential, resulting in a rotational energy as shown in equation (4).

$$E_{rot} = \frac{J(J+1)\hbar^2}{2MR^2} + \frac{1}{2}k(R - R_e)^2 \quad (4)$$

Since $x \ll 1$ the $1/R^2$ term can be expanded into a power series, where the rotational energy becomes

$$E_{rot} = \frac{J(J+1)\hbar^2}{2MR_e^2} - \frac{J^2(J+1)^2\hbar^4}{2M^2kR_e^6} + \frac{3J^3(J+1)^3\hbar^6}{2M^3k^2R_e^{10}} + \cdots, \quad (5)$$

which essentially means that the rotational energy is only a function of *J*, since the other factors are constants:

$$E_{rot}(J) = B_eJ(J+1) - D_eJ^2(J+1)^2 + H_eJ^3(J+1)^3 - \cdots \quad (6)$$

with rotational constants B_e, D_e and H_e, which can be directly taken from (5). Current day spectroscopic techniques are accurate enough that even the third order term in this expansion has to be taken into account for some experiments. For many electronic and vibrational states in diatomic molecules the constants B_e, D_e and sometimes H_e are reported in literature.

2.1.2 Vibrational states

For vibrations in a non-rotating molecule the quantum number J is zero, using this in the radial part of the three dimensional Schrödinger equation in the adiabatic approximation, gives the solution of the regular harmonic oscillator. This is provided that the potential is parabolic, which is a good first approximation. The energy levels then become [57]

$$E(v) = h\omega\left(v + \frac{1}{2}\right) \quad (7)$$

where v is the vibrational quantum number, being a positive integer. The solution of the radial wave equation becomes

$$S(R) = \psi_{vib}(R, v) = \exp\left(-\frac{\pi M\omega}{hR}\right) \cdot H_v(R) \quad (8)$$

where $H_v(R)$ are Hermitian polynomials. A parabolic potential is a good approximation close to the equilibrium position, R_e. However the larger R becomes, the more it starts to deviate from the parabolic shape. A better approximation for the potential is the Morse potential [58]:

$$E_{pot}(R) = E_D\big(1 - \exp\big(-a(R - R_e)\big)\big)^2. \quad (9)$$

Here E_D is the dissociation energy and a is a fitting parameter, since this is an empirical result. In Figure 8 the Morse potential is compared to the previously assumed parabolic potential. It can be seen that the Morse potential has a much more realistic shape compared to the harmonic oscillator.

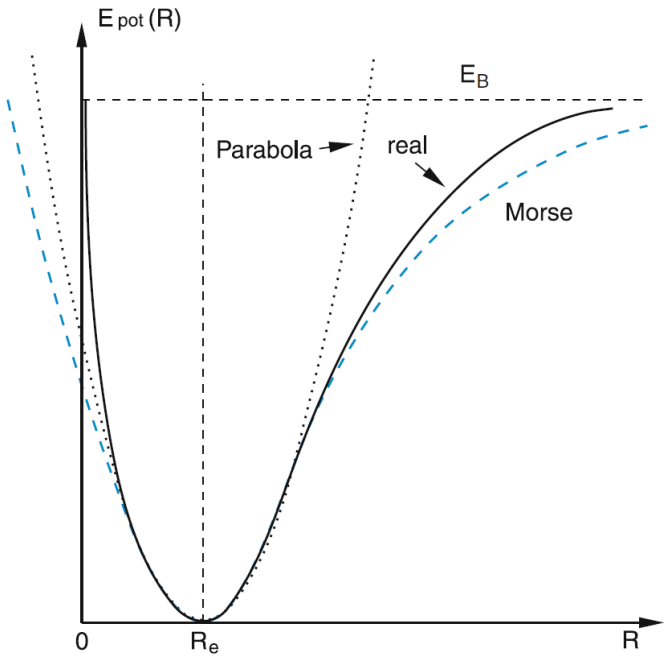

Figure 8 Morse potential compared to the harmonic oscillator (parabolic potential), as well as the real measured potential. Indicated is also the dissociation energy, E_B.. Figure taken from: Demtroder, W., "Atoms, Molecules and Photons" [56]

Solving the radial part of the Schrodinger equation using the Morse potential gives the following energy eigenvalues:

$$E_{vib}(v) = \hbar\omega_0\left(v+\frac{1}{2}\right) - \frac{\hbar^2\omega_0^2}{4E_D}\left(v+\frac{1}{2}\right)^2, \qquad (10)$$

where the Morse potential is a more accurate representation of reality compared to the harmonic oscillator for $\lim_{R\to\infty} E_{pot}$. The harmonic oscillator goes to infinity, whereas the Morse potential converges on the dissociation energy. This however means that the spacing between vibrational energy levels decreases for increasing vibrational quantum number v [55], which is in accordance with experimental results [59].

The vibrational energy levels can be expressed in spectroscopic constants, similarly to the rotational constants B_e, D_e and H_e,

$$E_{vib}(v) = \omega_e\left(v+\frac{1}{2}\right) - \omega_e x_e\left(v+\frac{1}{2}\right)^2 \qquad (11)$$

with $\omega_e = \frac{\omega_0 h}{2\pi}$ and $\omega_e x_e = \omega_e^2 \frac{1}{4E_d}$ as vibrational constants. These constants are similar in their use as those for rotational states, since their values for specific states in molecules can be found in literature. For the CO molecule these constants can be found in the detailed work by Krupenie [54].

2.1.3 Interaction between vibrational and rotational states

So far rotating molecules that do not vibrate and vibrating molecules that do not rotate have been studied. However real molecules can simultaneously rotate and vibrate. Since the vibrational frequency is usually some two orders of magnitude larger than the rotational frequency [55] a molecule undergoes

many vibrations within one rotational period. This means the distance between the two nuclei of the diatomic molecule changes periodically during one rotation. The total energy of the molecule, thus the sum of the rotational, vibrational and potential energy, has to be constant in time. However there is an exchange in these different energies during the periodic motion that the molecule undergoes.

Mathematically this can be approached by starting at equation (1), where *R* is no longer constant. The average of *R* is

$$\langle R \rangle = \int \psi_{vib}^{*} R \psi_{vib} dR \qquad (12)$$

and the average of $1/R^2$ is

$$\langle 1/R^2 \rangle = \int \psi_{vib}^{*} \frac{1}{R^2} \psi_{vib} dR. \qquad (13)$$

Substituting this in equation (1) gives the mean rotational energy, averaged over one vibrational period,

$$\langle E_{rot}(v) \rangle = \frac{J(J+1)}{2M} \int \psi_{vib}^{*}(v) \frac{1}{R^2} \psi_{vib}(v) dR. \qquad (14)$$

The rotational energies can be expressed by a rotational constant, B_v, which is averaged over the vibrational motion,

$$B_v = \frac{\hbar}{4\pi c M} \int \psi_{vib}^{*}(v,R) \frac{1}{R^2} \psi_{vib}(v,R) dR. \qquad (15)$$

For a Morse potential this can be expressed as follows [56],

$$B_v = B_e - \alpha \left(v + \frac{1}{2} \right) \qquad (16)$$

where B_e is the lowest order rotational constant derived in section 2.1.1, and $\alpha \ll B_e$. Since the vibrational period is on a different timescale than the rotational timescale its influence on the rotational constants is relatively small. A similar strategy can be applied to obtain an average centrifugal constant,

$$D_v = \frac{\hbar^3}{4\pi c k M^2} \int \psi_{vib}^{*} \frac{1}{R^6} \psi_{vib} dR\,. \qquad (17)$$

This can be related to the centrifugal constant of (6) as well by

$$D_v = D_e - \beta_e \left(v + \frac{1}{2} \right). \qquad (18)$$

For a general potential instead of the Morse potential higher order constants have to be introduced. The energy value for a rotational-vibrational level then becomes a combination of the two given by equations (6) and (11)(13), namely

$$E(v,J) = E_e + \left(\omega_e \left(v + \frac{1}{2} \right) - \omega_e x_e \left(v + \frac{1}{2} \right)^2 + \omega_e y_e \left(v + \frac{1}{2} \right)^3 + \cdots \right) + (B_v J(J+1) - D_v J^2 (J+1)^2 + H_v J^3 (J+1)^3 - \cdots), \qquad (19)$$

with E_e the energy associated with the electronic level concerned. For a Morse potential this reduces to

$$E^{Morse}(v,J) = E_e + \omega_e \left(v + \frac{1}{2} \right) - \omega_e x_e \left(v + \frac{1}{2} \right)^2 + B_v J(J+1) - D_v J^2 (J+1)^2. \qquad (20)$$

The five constants in this expansion describe the energy of all the levels up to where the Morse potential is no longer a valid approximation.

In 1932 Dunham introduced an expansion to calculate the energy values for any state in a diatomic molecule though a set of constants [60]. This was later called the Dunham expansion. The generic potential can be expressed as

$$E_{pot}(R) = \sum_{\mathrm{n}} a_n (R - R_e)^n \, , a_n = \frac{1}{n!} \left(\frac{\partial^n E_{pot}}{\partial R^n} \right)_{R_e} . \qquad (21)$$

Which be rewritten to energies depending on v and J as

$$E(v, J) = \sum_k \sum_i Y_{ik} \left(v + \frac{1}{2} \right)^i (J(J+1) - \Lambda)^k \qquad (22)$$

where Y_{ik} are fit parameters chosen in such a way that the energy values calculated through this equation match those measured in experiments. Λ is a molecular quantum number which represents the orbital angular momentum projected on the molecular axis [61].

If the Morse potential is applied as a generic potential the spectroscopic constants are returned, which can be seen in Table 1. The coefficient Y_{00} gives the energy of the electronic state.

Table 1 The relationship between the first coefficients of the Dunham expansions and the spectroscopic coefficients derived for the Morse potential.

$Y_{10} \approx \omega_e$	$Y_{20} \approx \omega_e x_e$	$Y_{30} \approx \omega_e y_e$
$Y_{01} \approx B_e$	$Y_{02} \approx D_e$	$Y_{03} \approx H_e$
$Y_{11} \approx -\alpha_e$	$Y_{12} \approx -\beta_e$	$Y_{21} \approx \gamma_e$

The Dunham expansion provides a complete set of constants to fully describe energy values for rotational and vibrational states within an electronic state. In most cases however the Morse potential is an accurate enough representation of the potential curve of a diatomic molecule.

2.2 Structure of transitions

In the previous section the structure of vibrational and rotational states is discussed, this is expanded in this section to include the theory of electronic transitions in diatomic molecules, which details transition probabilities and selection rules.

Transition probabilities for a transition $E_i \leftrightarrow E_k$ can be described by the square of dipole matrix elements [57]. Since molecules have a more complex energy structure than atoms, which is due to rotational and vibrational levels, their matrix elements are more complicated to calculate. The general equation for the dipole matrix element of a transition is

$$\boldsymbol{M}_{ik} = \int \int \psi_i^* \boldsymbol{p} \psi_k d\tau_{el} d\tau_N \qquad (23)$$

where $\boldsymbol{p}$ is the transition dipole operator, and the integration extends over all electronic coordinates, as well as nuclear coordinates. This is at first simplified by assuming only one of the electrons is involved in the transition. That means the integration over $d\tau_{el}$ only needs to be performed over one electron. The dipole element can be written as

$$\boldsymbol{p} = \boldsymbol{p}_{el} + \boldsymbol{p}_N, \qquad (24)$$

where it is split in a contribution of the electrons and a contribution of the nuclei.

The wave functions ψ_i and ψ_k can be separated into the product

$$\psi(r,R) = \phi(r,R)\,\chi_N(R) \qquad (25)$$

of the electronic wave function ϕ, which signifies the rigid molecule at fixed distance *R*, and the nuclear wave function χ_N, which only depends on the nuclear coordinates. Inserting equations (24)and (25)in equation (23) and rearranging gives

$$\boldsymbol{M}_{ik} = \int \chi_i^* \left(\int \phi_i^* p_{el} \phi_k d\tau_{el} \right) \chi_k d\tau_N + \int \chi_1^* p_N \left(\int \phi_i^* \phi_k d\tau_{el} \right) \chi_k d\tau_N. \qquad (26)$$

The distinction can be made between two separate cases. Firstly there is the case where there is no change in the electronic state, and there is only a change in rovibronic quantum numbers, these transitions lie in the infrared regime, $2 < \lambda < 20\mu\mathrm{m}$, since the energy associated with such a transition is relatively small [62]. The second case is when there is a change in the electronic quantum number. These transitions have a much higher energy, usually in the visible, or UV range [62].

Since laser induced fluorescence considers light in the visible or near UV regime it is safe to assume only electronic transitions are important. Thus the second case has to be considered, which means the integral over the electronic coordinates of the second term in (26) is zero, since ϕ_i and ϕ_k are orthonormal. The matrix element therefore becomes

$$\boldsymbol{M}_{ik} = \int \chi_i^* \left(\int \phi_i^* p_{el} \phi_k d\tau_{el} \right) \chi_k d\tau_N = \int \chi_i^* M_{ik}^{el}(R) \chi_k d\tau_N \,. \qquad (27)$$

The electronic part of this matrix element is dependent on the internuclear distance, however often this dependence is quite weak [56], and M_{ik}^{el} can be expanded in a Taylor series. This yields

$$M_{ik}^{el} = M_{ik}(R_e) + \left(\frac{dM_{ik}^{el}}{dR} \right)_{R_e} (R - R_e) + \cdots. \qquad (28)$$

In a first approximation only the first term, which is independent on *R* is considered. This constant can then be taken out of the integral of (27). The nuclear wave function can be split as $\chi_N = \psi_{vib} \cdot Y(\theta,\phi)$. The matrix element then becomes

$$\boldsymbol{M}_{ik} = M_{ik}^{el}(R_e) \int \psi_{vib}^*(v_i) \psi_{vib}(v_k) dR \cdot \int Y_{J_i}^{M_i} Y_{J_k}^{M_k} \sin(\theta)\, d\theta d\phi. \qquad (29)$$

The intensity of a spectral emission line is proportional to the square of $\boldsymbol{M}_{ik}$,

$$I\left(n_i, v_i, J_i \leftrightarrow n_k, v_k, J_k\right) = \left|M_{ik}^{el}\right|^2 \cdot FC(v_i, v_k) \cdot HL(J_i, J_k) \qquad (30)$$

where *FC* stands for the Franck-Condon factor and *HL* stands for the Hönl-London factor.

The factor $\left|M_{ik}^{el}\right|^2$ depends on the electronic wave functions of $|i\rangle$ and $|k\rangle$. The Franck-Condon factor is determined by overlap of the vibrational wave functions in the upper and lower electronic state, $|\psi_{vib}(v_i)\rangle$ and $|\psi_{vib}(v_k)\rangle$, respectively, and can be expressed as

$$FC(v_i, v_k) = \left| \int \psi_{vib}^*(v_i) \psi_{vib}(v_k) dR \right|^2. \qquad (31)$$

The last factor making up the line intensity is the Hönl-London factor, which is determined by the overlap of the rotational wave functions in the upper and lower state, expressed as

$$HL((J_i, J_k) = \left| \iint Y_{J_i}^{M_i} Y_{J_k}^{M_k} \sin(\theta)\, d\theta d\phi \right|^2. \quad (32)$$

This factor depends on the rotational angular momenta. All three of these factors have to be non-zero in order for a transition to take place.

2.2.1 The vibrational structure of transitions and the Franck-Condon principle

The Franck-Condon factors govern the vibrational structure of transitions, since they are determined by the overlap in vibrational wave functions, as shown in equation (30). In practice, the Franck-Condon factors govern how the absorption or fluorescence is distributed among the different vibrational modes. This can be more clearly understood by looking at a classical model describing vibrational transitions. This model starts with the assumption that the photon process happens in a time interval that is short compared to one vibrational period [63]. In a potential diagram these transitions can then be represented by a vertical arrow, since there will be no change in the radius. A valid assumption is furthermore that the momentum of the absorbed or emitted photon is small compared to the total momentum of the vibrating nuclei, therefore this momentum, *p*, is unchanged. This also means the kinetic energy, $\frac{p^2}{2M}$, remains constant. Working out the energy balance of this transition then leads to

$$h\nu = E'(\nu') - E''(\nu'') = E'_{pot}(R) - E''_{pot}(R) + E'_{kin}(R) - E''_{kin}(R). \quad (33)$$

When using the assumption that the kinetic energy is unchanged the energy balance changes to

$$h\nu = E'_{pot}(R^*) - E''_{pot}(R^*). \quad (34)$$

This model gives a classical interpretation of electronic transitions in molecules, where such a transition only occurs if the two radii and their kinetic energies are equal. Quantum mechanically the probability for a transition is highest at this point, upon which the Franck-Condon principle is based.

Figure 9 illustrates the Franck-Condon principle. Vertical arrows indicate instantaneous transitions. The wave functions of the vibrational states are indicated in the figure as well. This illustrates that the transition probability is highest when the overlap in vibrational wave function is highest.

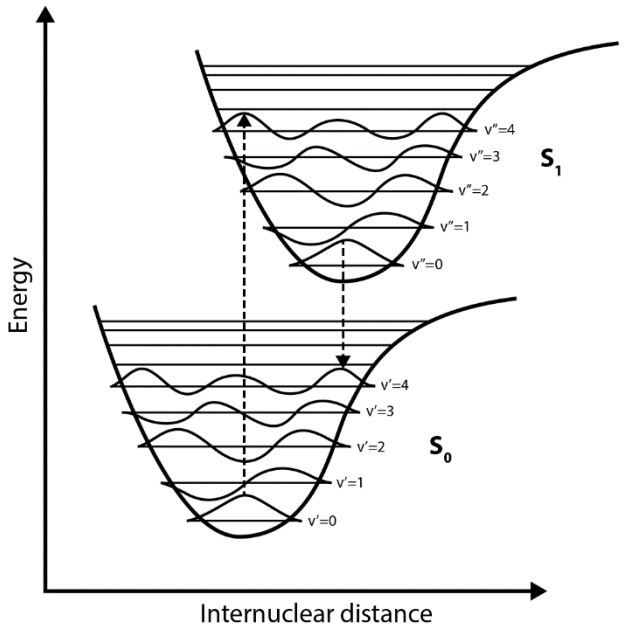

Figure 9 Illustration of the Franck-Condon principle, showing transition between two electronic states as straight arrows. Wihtin the electronic levels different vibrational states are indicated, together with their potentials. Figure adapted from [64]

The fact that the probability for a transition is related to the overlap of the vibrational wave functions translates also into the Franck-Condon factors. Mathematically, the probability that an electronic transition takes place in the interval *dR* around *R* is given by

$$P(R)dR = \frac{\psi'_{vib}(R)\psi''_{vib}(R)dR}{\int \psi'_{vib}(R)\psi''_{vib}(R)dR}, \qquad (35)$$

which has a maximum for $R = R^*$. The FC has a maximum for $\Delta v = 0$ if the two potential curves have a similar *R*-dependence. In that case the FC factors for $\Delta v \neq 0$ are much smaller. The maximum FC factor shifts to different Δv the more the curves differ from each other. The calculation of the Franck-Condon factors is described Bates [65] and Lefebvre-Brion [66]. From a list of tables the FC factors can be calculated if several spectroscopic constants are known. For most band systems of CO the FC factors are known, at least to a reasonably high vibrational number.

2.2.2 Rotational structure of transitions

All allowed transitions, $J_i'' \leftrightarrow J_k'$ between a specific rotational state J_k', in a vibrational level, v', in the upper electronic state and J_k'' of v'' of the lower electronic state form a band. Such a band usually consists of many rotational lines. There are three different branches to identify different rotational transitions in these bands. There is the Q-branch, for $\Delta J = 0$, the R-branch with $\Delta J = +1$ and the P-branch with $\Delta J = -1$. Q-branches are only allowed when there is a change in electronic angular momentum, thus $\Delta\Lambda \neq 0$ [56].

The energy of a transition $(n_i, v_i, J_i) \leftrightarrow (n_k, v_k, J_k)$ can be calculated using the rotational constants for both bands, which leads to an energy given by:

$$E_{n',v',J'\to n'',v'',J''} = E_{n',v'\to n'',v''} + B'_v J'(J'+1) - D'_v J'^2 (J'+1)^2 - \left(B''_v J''(J''+1) - D''_v J''^2 (J''+1)^2\right). \quad (36)$$

Here $E_{n',v'\to n'',v''}$ is the energy associated with a transition from the electronic and vibrational ground state *i*, to the excited electronic and vibrational state *k*. This energy can be obtained from the Dunham coefficients and the energy difference between the electronic bands.

The line strength of a transition from one specific rotational state to another specific rotational state is governed by the Hönl-London factor, first described by Hönl and London in 1925 [67]. These factors describe the rotational part of the matrix element describing a transition. For the general case, using the Wigner-Eckart theorem, the Hönl-London factors scale with the square of the *3-j* symbol,

$$HL \propto \begin{pmatrix} J_f & 1 & J_i \\ -\Omega_f & q & \Omega_i \end{pmatrix}^2 \quad (37)$$

where J_i and J_f are the *J*-values for the initial and final state in the transition, and Ω_i and Ω_f are molecular quantum numbers depicting the projection of the total nuclear angular momentum on the internuclear axis [68]. q is the difference between these quantum numbers, thus $q = 0$ for $\Delta\Omega = 0$ and $q = \pm 1$ for $\Delta\Omega = \pm 1$. This is however only a general result. Kovacs detailed the Hönl-London factor for various spin-orbit coupling cases [69]. In the case of CO the Hönl-London factors depend on quantum numbers *J* and Ω, where $\Omega = \Lambda + \Sigma$ [61], and can thus be computed.

2.3 Three level scheme of laser induced fluorescence

Laser induced fluorescence (LIF) is a spectroscopy technique used for the detection of certain species. Laser light with wavelength λ, corresponding to an excitation wavelength of the species under investigation, irradiates the gas sample. This excites only the molecules of the species of interest. These excited molecules can then fall back to their original state, or to another energy level, thereby emitting respectively the original wavelength or a longer wavelength. The falling back to another state and emitting a different wavelength than λ is called fluorescence. This process is schematically shown in Figure 10 as a three-level system, signifying three electronic levels, thereby ignoring rotational and vibrational states which build up these electronic levels. Here the Einstein coefficients, B_{ij} and A_{ij} are shown, for i and j the different states $|1\rangle, |2\rangle,$ and $|3\rangle$.

This three level system can be used to describe the LIF process. The population and depopulation rates are given by the Einstein coefficients. B_{12} describes absorption, B_{21} stimulated emission, A_{21} and A_{23} spontaneous emission. Quenching, symbolized by Q_i, describes all the processes that depopulate a state through different means than emission. This includes photo-ionization, collisions and dissociation.

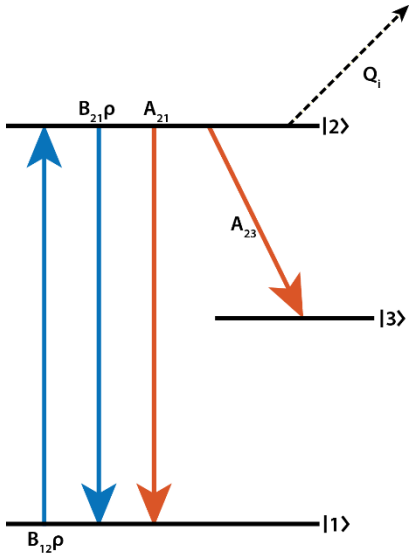

Figure 10 Schematic display of an energy diagram depicting laser induced fluorescence where absorption, stimulated emission and two spontaneous emission routes are shown, indicated by their respective Einstein coefficients.

The rate equations for this three-level system can be expressed using the Einstein coefficients as:

$$\begin{aligned}\frac{\partial n_1(t)}{\partial t} &= -n_1(t)B_{12}\rho_\nu(t) + n_2(t)(B_{21}\rho_\nu(t) + A_{21}) \\ \frac{\partial n_2(t)}{\partial t} &= n_1(t)B_{12}\rho_\nu(t) - n_2(t)(B_{21}\rho_\nu(t) + A_{21} + A_{23} + Q_i) \\ \frac{\partial n_3(t)}{\partial t} &= A_{23}n_2(t).\end{aligned} \qquad (38)$$

Here $n_i(t)$ is the number density of each state i in m^{-3}, Q_i is the quenching coefficient depopulating $|2\rangle$ in s^{-1}, A_{ij} and B_{ij} are the Einstein coefficients in s^{-1} and $\mathrm{J}^{-1}\mathrm{m}^3\mathrm{s}^{-2}$ respectively. The difference in these units is caused by the addition of the laser power density, ρ_ν, in $\mathrm{Js}^{-1}\mathrm{m}^{-3}$. A relation exists between the coefficients for absorption and stimulated emission, $B_{12} = g_2/g_1 B_{21}$, with g_2 and g_1 the degeneracy of states $|1\rangle$ and $|2\rangle$ [70]. In reality depopulation of state $|3\rangle$ to the ground state should also be added, however this is left out for simplicity.

Assuming photo-ionization, photo-dissociation or other light-induced chemistry can be neglected, the quenching term, Q_i, can be expressed as the sum of collisional quenching effects from different species [71][72]:

$$Q_i = \sum_q Q_i^q = \sum_q \langle v_q \rangle \sigma_q n_q. \qquad (39)$$

Here $\langle v_q \rangle$ is the average velocity of a particle with respect to the particle of interest, σ_q is the quenching cross section, or the collision cross-section, and n_q is the number density of particle type q.

A pulsed laser with a pulse length in the nanosecond range is used in this study. Hence the assumption is made that a molecule can only be excited once during one laser pulse. If a molecule would be excited multiple times the following process could occur: de-excitation from $|3\rangle$ to $|1\rangle$, successive excitation to $|2\rangle$ and de-excitation to $|3\rangle$ again. This would give multiple fluorescence signals from the same

molecule. Furthermore, convection is neglected. Convection of particles into the detection volume during a laser pulse increases the population of $|1\rangle$. It also increases the depopulation of $|2\rangle$ through additional collisional quenching. These effects have typical rates of respectively $10^7 \mathrm{s}^{-1}$ and $10^5 - 10^6 \mathrm{s}^{-1}$ [73]. The Einstein A coefficient of a short lived state of several nanoseconds is in the range of $10^8 \mathrm{s}^{-1}$, showing that convection might not be trivial. It is however not taken into further account, since that would be outside the scope of this work.

An important aspect is the spectral shape of the laser, which has an effect on the absorption rate $B_{ij}\rho_v(t)$. If $\rho_v(t)$ is not constant over the spectral interval of the absorption line an overlap integral of the laser with this line needs to be computed. This can be defined as follows[74]:

$$\rho_v(t,\nu) = \rho_L(t)\epsilon(\nu - \nu_L) \text{ with } \int_{-\infty}^{\infty} \epsilon(\nu - \nu_L) = 1 \quad (40)$$

$$B_{ij}(\nu) = B_{ij} b\big(\nu - \nu_{ij}\big) \text{ with } \int_{-\infty}^{\infty} b(\nu - \nu_L) = 1 \quad (41)$$

Here $b\big(\nu - \nu_{ij}\big)$ is the normalized absorption line profile centered at ν_{ij}, which is given by Doppler and pressure broadening. $\epsilon(\nu - \nu_L)$ is the normalized laser line profile and ρ_L is the time dependent laser power density. The absorption rate is now given as:

$$R_{ij}(t) = B_{ij}\rho_L(t) \int_{-\infty}^{\infty} \epsilon(\nu - \nu_L) b\big(\nu - \nu_{ij}\big) d\nu = B_{ij}\rho_L(t)\phi \quad (42)$$

Here ϕ is the overlap integral of the laser and absorption line profiles. $\rho_L(t)$ is the laser power density, which can be defined as:

$$\rho_L(t) = \frac{E_p F(t)}{cA}, \quad (43)$$

here E_p is the energy of the laser pulse, $F(t)$ the normalized time profile of the pulse, c the speed of light, and A the cross-sectional area of the laser beam. The absorption is often described in terms of a cross section, σ_{ij}:

$$\sigma_{ij} = \frac{h\nu_{ij}}{c} B_{ij}, \quad (44)$$

where *h* is Planck's constant, ν_{ij} is the absorption frequency, and B_{ij} is the Einstein coefficient of the absorption process.

The system of equations in (38) can be solved assuming that all particles are in the ground state before the laser is pulse arrives. This imposes the following boundary conditions:

$$n_1(0) = N, \qquad n_2(0) = n_3(0) = 0 \quad (45)$$

with *N* the initial number density, which all reside in state $|1\rangle$. A pulsed laser is used where it is assumed the power profile of the laser, $F(t)$, is a block function with height $1/\tau_p$. The pulse starts at $t = 0$ and ends at $t = \tau_p$. After the laser pulse, $\rho_L\big(t > \tau_p\big) = 0$ again. Therefore, after the laser pulse equation (38) reduces to:

$$\frac{\partial n_2(t)}{\partial t} = -(A_{21} + A_{23} + Q_2) n_2(t) \quad (46)$$

signifying that state $|2\rangle$ is not affected by photon induced processes anymore, population of this state is only lost to quenching and emission. This differential equation can be solved to an exponential:

$$n_2(t) = C \exp\left(-\frac{t}{\tau_{eff}}\right). \quad (47)$$

Here C is an integration constant and τ_{eff} is the effective lifetime of state $|2\rangle$, defined as $(A_{21} + A_{23} + Q_2)^{-1}$. This quantity can be expressed in the natural lifetime ($\tau_i = (A_{21} + A_{23})^{-1}$) and the quenching coefficient Q_i as

$$\frac{1}{\tau_{eff}} = \frac{1}{\tau_i} + Q_i. \quad (48)$$

If the effective lifetime of state $|2\rangle$ is much shorter than the time between laser pulses, state $|2\rangle$ will be all but depleted when the next pulse starts. This means the boundary conditions of equation (40) are valid for each pulse. Measuring the effective lifetime provides a technique to account for quenching if the natural lifetime is known. This method is known as the Stern-Volmer method.

2.4 Fluorescence yield

Solving the system of equations for this three level system, shown in (38), gives the fluorescence yield. The system can be split into two different time segments, $0 < t \leq \tau_p$ and $t > \tau_p$, for which the equations have to be solved separately. The total LIF yield, *F*, can be expressed as the time-integrated decay of state $|2\rangle$ to state $|1\rangle$ and $|3\rangle$:

$$F = F_{21} + F_{23} = \int_0^\infty (A_{21} + A_{23}) n_2(t) dt. \quad (49)$$

In this equation it can be seen that the total fluorescence yield is only dependent on the population of state $|2\rangle$. Therefore an expression has be found for $n_2(t)$, which is done by solving the rate equations of this system, with boundary conditions shown in (45), which gives:

$$n_2(t) = \begin{cases} \frac{g_2}{g_1}\frac{2B_{21}\rho_L(t)N}{Y}\sinh\left(\frac{1}{2}Yt\right)\exp\left(-\frac{1}{2}(X + Q_2 + \Sigma A)t\right) & \text{if } 0 < t \leq \tau_p \\ \frac{g_2}{g_1}\frac{2B_{21}\rho_L(t)N}{Y}\sinh\left(\frac{1}{2}Yt\right)\exp\left(-\frac{1}{2}(X - Q_2 - \Sigma A)\tau_p\right)\exp\left(-t(Q_2 + \Sigma A)\right) & \text{if } t > \tau_p \end{cases} \quad (50)$$

with:

$$\Sigma A = A_{21} + A_{23}$$
$$X = B_{21}\rho_L(t)\phi\left(1 + \frac{g_2}{g_1}\right) \quad (51)$$
$$Y = \sqrt{(\Sigma A + Q_2 + X)^2 - 4(A_{23} + Q_2)B_{21}\frac{g_2}{g_1}\rho_L(t)\phi}\,.$$

Using this equation, the total LIF yield, expressed in (49), can now be evaluated as

$$F = \frac{\Sigma A}{Q_2 + \Sigma A}\left(\frac{g_2}{g_1}B_{21}\rho_L(t)\phi N\left[\frac{4\Sigma A}{K_1K_2} + \frac{K_1 - 2\Sigma A}{K_1 R}\exp\left(-\frac{1}{2}K_1\tau_p\right) + \frac{2\Sigma A - K_2}{K_2 R}\exp\left(-\frac{1}{2}K_2\tau_p\right)\right]\right) \quad (52)$$

where $K_1 = X + Q_2 + \Sigma A - Y$ and $K_2 = X + Q_2 + \Sigma A + Y$. Equation (52) shows that the fluorescence yield is a function of laser power density, ρ_L, which is plotted in Figure 11. Two regimes for the fluorescence yield can be identified when looking at this figure. For low laser power densities there is the linear regime, indicated with a tangent in Figure 11. A horizontal tangent, drawn at high laser power densities, indicates the saturated regime. This is where the fluorescence yield becomes independent of laser power density.

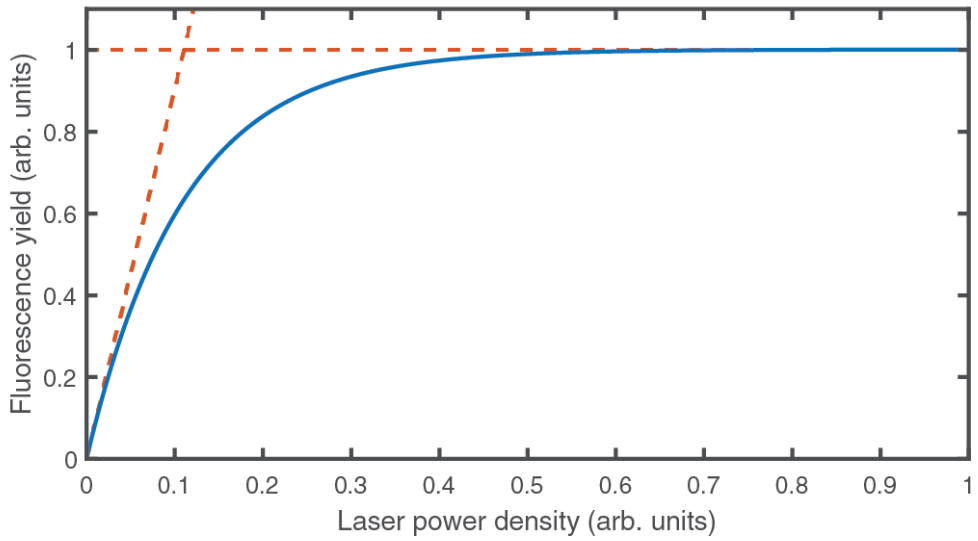

Figure 11 Fluorescence yield as a function of laser power density, both in arbitrary units. Tangent lines are drawn to indicate the linear regime at low power densities, and the saturated regime at high power densities.

2.4.1 Linear regime

To derive an approximation for the fluorescence yield in the linear regime two assumptions are made: $B_{21}\rho \ll A_{23}$ and $A_{21} \ll A_{23}$, signifying that spontaneous and stimulated emission to the ground state are both negligible, since the population of the excited levels relative to the ground state is negligible. This reduces the rate equations to:

$$\begin{aligned} \frac{\partial n_1(t)}{\partial t} &= -B_{12}\rho_L(t)\phi n_1(t) \\ \frac{\partial n_2(t)}{\partial t} &= B_{12}\rho_L(t)\phi n_1(t) - (A_{23} + Q_2)n_2(t) \\ \frac{\partial n_3(t)}{\partial t} &= A_{23}n_2(t). \end{aligned} \qquad (53)$$

Thereby changing the fluorescence yield to:

$$F = N\big(1 - \exp\big(-B_{12}\rho_L(t)\phi\tau_p\big)\big)\frac{A_{23}}{A_{23} + Q_2}. \qquad (54)$$

This expression can be reduced further by using the assumption that the population of $|1\rangle$ is much larger than that of the other states, which can be rephrased by stating that the population of state $|1\rangle$ is far from depletion, $B_{12}\rho_L(t)\phi\tau_p \ll 1$. This reduces equation (54) to:

$$F \approx N\left(1-\left(1-B_{12}\rho_L(t)\phi\tau_p\right)\right)\frac{A_{23}}{A_{23}+Q_2} = NB_{12}\rho_L(t)\phi\tau_p\,\frac{A_{23}}{A_{23}+Q_2}. \qquad (55)$$

Thereby confirming the linearity of the fluorescence yield with laser power in this regime.

2.4.2 Saturated regime

In the linear regime the ground state is far from depletion, whereas in the saturated regime the opposite is the case, the ground state is almost completely depleted by the laser. This leads to the assumptions that state $|2\rangle$ is populated much faster than it is depopulated, so $B_{12}\rho_L \gg A_{23}$ and $B_{12}\rho_L \gg A_{21}$. These assumptions reduce the rate equations of (38) for $t < \tau_p$ to:

$$\begin{aligned}\frac{\partial n_1(t)}{\partial t} &= \rho_L(t)\phi\big(B_{21}n_2(t)-B_{12}n_1(t)\big)\\ \frac{\partial n_2(t)}{\partial t} &= \rho_L(t)\phi(B_{12}n_1(t)-B_{21}n_2(t)\\ \frac{\partial n_3(t)}{\partial t} &= A_{23}n_2(t)\end{aligned} \qquad (56)$$

and for $t > \tau_p$:

$$\begin{aligned}\frac{\partial n_1(t)}{\partial t} &= A_{21}n_2(t)\\ \frac{\partial n_2(t)}{\partial t} &= -(A_{23}+A_{21}+Q_2)n_2(t)\\ \frac{\partial n_3(t)}{\partial t} &= A_{23}n_2(t).\end{aligned} \qquad (57)$$

This leads to a total fluorescence yield *F* of:

$$F = N\big(1+\tau_p\Sigma A\big)\frac{\Sigma A}{\Sigma A+Q_2}. \qquad (58)$$

Which shows that the fluorescence yield is independent of the laser power in this limit. Next to that it shows that state $|2\rangle$ is completely populated at the start of the laser pulse. Emission at a rate $N\,\Sigma A$ for the duration of the laser pulse occurs. Once the pulse is passed the entire population of $|2\rangle$ undergoes spontaneous emission once more, leading to an additional factor *N*. The main inaccuracy of this analysis comes from the temporal shape of the laser pulse. This is assumed to be a block-pulse, which is not physically realistic, but the best approximation present.

This theory explains why operation in the linear regime is preferential in a LIF experiment. In the saturated regime the ground state gets depleted, which means the excited levels are highly populated. A higher populated excited state makes it more probable that photo-chemistry, such as photo-ionization and photo-dissociation, becomes important. Not only that, but stimulated emission to state $|3\rangle$ by the excited molecules might become non-negligible. Stimulated emission by these molecules invalidates one of the main assumptions of the LIF theory, that the emitted light is omnidirectional.

2.5 Detected signal

The fluorescence yield as described in equation (52) is not necessarily the same as the signal that is detected. Usually less photons are detected than emitted by the system, due to for instance imperfect optics or not perfectly matched numerical apertures. Another cause for losses of photons might be that only one branch of fluorescence is detected by using bandpass filters. However it is also possible that more photons are detected if an intensifier is used.

The detection efficiency as a function of wavelength can be written as follows:

$$G(\lambda) = V_{det}\frac{\Omega}{4\pi}T(\lambda)\eta(\lambda). \qquad (59)$$

This states that the efficiency depends on the detection volume, V_{det}, the solid angle of detection, Ω, the transmittance of the optics as a function of wavelength, and the efficiency of the detector as a function of wavelength.

The total signal as detected can be expressed as a product of the fluorescence yield, *F*, and the efficiency, *G*. This assumes all the different fluorescence paths are detected, whereas it is possible that some fluorescence is not detected since filters are in place. An additional branching factor needs to be included to give the correct detected signal:

$$S_{LIF} = F \cdot \sum_i \frac{A_{2i}}{\sum A} \cdot G(\lambda_{2i}). \qquad (60)$$

Here the summation over i goes over all fluorescence paths that are detected. This modifies the detection efficiency. Not all possible wavelengths need to be taken into account, only the wavelengths corresponding to the fluorescence paths that are detected have to be considered.

2.6 Two Photon Absorption Laser Induced Fluorescence

One-photon LIF usually excites the species of interest to one of the first electronic states. However it can occur that these excited states lie above the vacuum UV limit ($E_{h\nu} > 6.5\text{eV}$). This means the light is not transmitted through air, making one-photon LIF experimentally challenging. For these particular cases two-photon LIF might be a suitable option.

The theory worked out so far, concerning laser induced fluorescence and transitions, only considers one-photon processes. This section starts by giving an extension to the three-level system as detailed in section 2.1. Two-photon transitions are the basis of TALIF, therefore the theory of one-photon transitions of the previous sections is also expanded upon.

2.6.1 Fluorescence yield and detected signal in two-photon processes

Two-photon absorption laser induced fluorescence can be the solution to avoid working in the vacuum UV regime. In TALIF the excitation to the excited state occurs through the absorption of two photons. The species is first excited to an intermediate level, $|v\rangle$, whereupon further excitation to state $|2\rangle$ occurs. Usually two-photons of the same energy are used in experiments, therefore the intermediate state lies energetically halfway in between states $|1\rangle$ and $|2\rangle$. It is also possible to use two photons of different energies, whose total energy sums up to the transition energy. In the remainder of this work it is assumed that in two-photon LIF processes the two photons have the same energy and polarization.

The general case of TALIF is illustrated in the schematic of Figure 12, where the different Einstein coefficients are indicated, together with the relevant states, as well as the quenching process, similar to Figure 10.

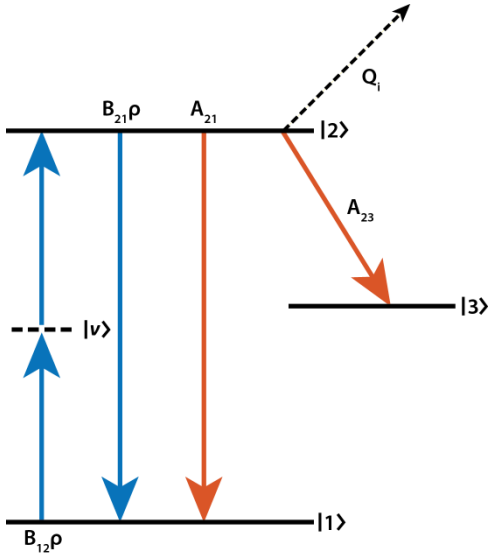

Figure 12 Schematic of a TALIF energy diagram, indicating the different Einstein coefficients for the different reactions involved.

Now a mathematical analysis can be performed on this system, similar to the analysis in sections 2.3 and 2.4. However there are some essential differences comparing two photon transitions to one photon transitions. At first the selection rules, the one-photon LIF selection rules have to be applied twice. In the general case this allows for $\Delta J = 0, \pm 1, \pm 2$ [75]. However for a $\Sigma - \Sigma$ transition in a diatomic molecule using linear polarization this reduces to $\Delta J = 0, \pm 2$ [66]. This also means that a one-photon transition back to the ground state becomes forbidden, since the selection rules for these are $\Delta J = \pm 1$ [76]. For the Einstein coefficients of Figure 12 this means B_{21} becomes almost zero. The rate equation for state $|1\rangle$ becomes

$$\frac{\partial n_1(t)}{\partial t} = -B_{12}\rho_\nu(t)n_1(t) \qquad (61)$$

with ρ_ν again the laser power density, B_{12} the Einstein coefficient for excitation and n_1 the density of molecules in the ground state. The excitation rate, $B_{12}\rho_\nu$ can be expressed as a function of the excitation cross section as

$$B_{12}\rho_\nu = G^{(2)}\sigma^2 g(\Delta\nu)\left(\frac{I_0(t)}{h\nu}\right)^2 \qquad (62)$$

with $g(\Delta\nu)$ the normalized line profile of the two-photon excitation, *G* is a photon statistic factor, which is equal to 2 for a multimode laser, such as a dye laser [77], σ the cross section, *h* Planck's constant and $I_0(t)$ the laser pulse power per area as a function of time.

The normalized line profile is composed of the convolution of the one-photon spectral profile, with photon energy ν_L, with the absorption line profile of the atom or molecule, with two-photon resonance frequency ν_A. With the spectral shape of the photons as $g_L(\nu_L)$ and that of the absorption line $g_A(\nu_A)$ this takes the following form [78]

$$g(\Delta\nu = 2\nu_L - \nu_A) = g_A(\nu - \nu_A) * g_L(\nu - \nu_L) * g_L(\nu - \nu_L). \quad (63)$$

An expression can also be derived for the population in the excited state, $|2\rangle$, similar to equation (38):

$$\frac{\partial n_2(t)}{\partial t} = B_{12}\rho_\nu(t)n_1(t) - (A_{21} + A_{23} + Q_i)n_2(t) \quad (64)$$

with A_{23} the Einstein coefficient for fluorescence to state $|3\rangle$ and Q_i once again the quenching coefficient. Therefore the fluorescence yield simplifies to:

$$F = (A_{21} + A_{23}) \int_0^\infty n_2(t)dt. \quad (65)$$

The cross sections for two-photon processes generally are much lower than for one-photon processes, therefore it can be assumed that state $|1\rangle$ is far from depletion. Therefore the assumptions made in section 2.4.1 are valid, and the system operates in the linear regime. Therefore the detected signal will become:

$$S_{TALIF} = F + G(\lambda) = N \frac{A_{21} + A_{23}}{A_{21} + A_{23} + Q_i} P^{(2)}\sigma^{(2)}g(\Delta\nu)\left(\frac{\langle I(t)\rangle}{h\nu_{23}}\right)^2 \tau_p\, G(\lambda). \quad (66)$$

It can be seen in this equation that the detected signal is proportional to the density of molecules in the ground state. Secondly the detected signal is proportional to the square of laser intensity.

2.6.2 Two-photon transitions and the intermediate state

One major difference between two-photon processes and one-photon processes is the presence of an intermediate state. This intermediate states has a significant impact, which follows when working out the transition probability. The general transition probability for a two-photon $|\mathrm{f}\rangle \leftarrow\leftarrow |\mathrm{i}\rangle$ process is given by [66]

$$P_{fi} \propto \left| \sum_j \frac{\langle f|\bar{\epsilon}\cdot\bar{\mu}\,|j\rangle\langle j|\bar{\epsilon}\cdot\bar{\mu}\,|i\rangle}{|E_{ji} - E|} \right|^2. \quad (67)$$

Here the sum is over intermediate states, $|\mathrm{j}\rangle$, $\bar{\mu}$ is an electric dipole operator, $\bar{\epsilon}$ is the vector displaying the electric field generated by the photons, and *E* is the energy of the photon. This assumes same energy and same polarization photons are involved in the process. In this equation two-photon absorption is described by the single-photon transition to virtual intermediate states, followed by a transition to the real final state. This method of describing two-photon absorption was first described by Göppert-Mayer [79].

A more simplified result, using spherical tensors instead of matrix elements is given by Hippler [80]:

$$\sigma_{J_f,J_i} \propto (2J_F + 1)(2J_i + 1) \sum_k (2k+1) \left| \begin{pmatrix} 1 & 1 & k \\ -p_2 & -p_1 & p_1 + p_2 \end{pmatrix} \right|^2 \left| \sum_{q_1+q_2} T^{(k)}_{q_1+q_2} \right|^2. \quad (68)$$

Here σ is the cross section of the transition, $J_{f,i}$ is the rotational quantum number of the different states, p_1 and p_2 specify the polarizations of the two photons, where $p = 0$ equals linear polarization. q is the change of quantum numbers Ω and Λ in each one-photon process involving the intermediate state. Therefore, $q_1 = \Omega_j - \Omega_i$ and $q_2 = \Omega_f - \Omega_j$. Finally, the $T^{(k)}_{q1+q_2}$ tensor contains all the information about the intermediate states.

For linearly polarized light, $p_1 = p_2 = 0$, the 3-j symbol is zero except for two terms, a $k = 0$ and a $k = 2$ term. This then reduces equation (75) to

$$\sigma_{J_f,J_i} \propto (2J_F + 1)(2J_i + 1)\left(\frac{1}{3}\left|\sum_{q_1+q_2} T^{(0)}_{q_1+q_2}\right|^2 + \frac{2}{3}\left|\sum_{q_1+q_2} T^{(2)}_{q_1+q_2}\right|^2\right). \quad (69)$$

This result shows that the cross section of a two-photon absorption transition is very dependent on the intermediate state. An illustration of this importance are two-photon $\Pi - \Pi$ transitions in diatomic molecules. These transitions are not only characterized by a $\Delta\Omega = 0$ component, but receive an additional $\Delta\Omega = \pm 2$ component, coming from the tensor describing the intermediate states. This gives rise to an interference effect, which is for example ignored in the work by Bray and Hochstrasser [75] and Freedman [81]. In such a $\Pi - \Pi$ transition, occurring through a Σ intermediate state, an additional term rises in the amplitude of the Q-branch, which alters the pattern of rotational branch intensities. This can be observed experimentally in the two-photon excitation of NO $C\,^2\Pi(v' = 0) \leftarrow\leftarrow X\,^2\Pi(v'' = 0)$ [80].

The changing of the cross-sections for two-photon transitions results in a change in the Hönl-London factors. The two-photon Hönl-London factors are different from those of single-photon transitions. Equation (76) can be simplified further to a product of two 3-j symbols,

$$HL \propto \begin{pmatrix} 1 & 1 & k \\ -q_2' & -q_1 & q_1' + q_2' \end{pmatrix}\begin{pmatrix} J_f & k & J_i \\ \Omega_f' & -q_1' - q_2' & -\Omega'_i \end{pmatrix}. \quad (70)$$

This general result is worked out by Bray and Hochstrasser [75], as well as by Chen & Yeung [82] to give Hönl-London factors that are a function of Λ, Ω, Σ and J_i and J_f, as well as the type of polarization. These intensity factors can therefore be applied, since all of these numbers are known for the involved transitions in CO.

2.7 Kasha's Rule

In a LIF experiment the excited state $|2\rangle$ gets populated by the laser. Due to the selection rules for rotational transitions only certain rotational states in $|2\rangle$ will be excited when a narrow linewidth laser is used. In state $|1\rangle$ a certain distribution of the occupation of the rotational states is present, a Boltzmann distribution if the system is in thermal equilibrium [83]. Kasha's rule describes that the molecules in $|2\rangle$ that get pumped to specific rotational states will relax to the rotational ground state in a much shorter timescale than the natural lifetime of the excited state, τ_i [84]. This means that there will be no difference in fluorescence wavelengths observed when the pumping laser wavelength is changed, since the fluorescence always comes from the rovibrational ground state [85]. Kasha's rule is applicable for larger molecules, due to their large density of rotational states. This allows for easier and faster internal conversion. In diatomic molecules the rotational constants are often larger, and therefore the spacing between different rotational peaks is larger. This means that internal conversion to lower lying rotational states will take longer, and Kasha's rule is generally assumed to be not applicable.

2.8 Excitation and fluorescence spectra

Two types of spectra are relevant when considering LIF, the excitation spectrum and the absorption spectrum. An excitation spectrum gives information about the wavelengths absorbed by a molecule. The excitation spectrum is different from an absorption spectrum, since the excitation spectrum only

concerns the wavelength where the light is absorbed and subsequently emitted as fluorescence. A fluorescence spectrum on the other hand gives information on the fluorescence emitted by the species for a fixed excitation wavelength. This is illustrated in Figure 13.

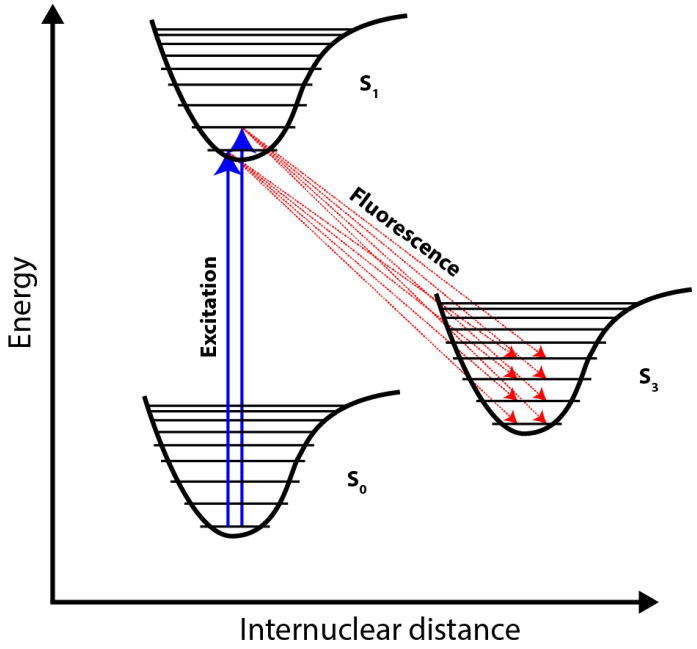

Figure 13 Schematic indicating the difference between excitation and fluorescence spectra, showing energy as a function of internuclear distance for three electronic states, which are made up of sub-states. The blue arrows indicate excitations to different states in the excited level S_1, whereas the red arrows shows the fluorescence emitted when the molecule deexcites to different rotational and vibrational levels in the intermediate electronic state S_3.

The experimental methods to measure these two spectra differs. In order to measure an excitation spectrum the wavelength is varied to excite the molecule to different excited states, whereas the emitted fluorescence is summed. To measure a fluorescence spectrum the pumping source has a fixed wavelength and the emitted fluorescence is spectrally resolved.

3. The spectrum of carbon monoxide

In chapter 2 the general theory of (two-photon) LIF and of transitions in diatomic molecules are discussed, whereas in this chapter this theory is applied to CO. Multiple excitation schemes for TALIF on CO are compared, next to that a simulation is developed which calculates both the fluorescence and the excitation spectrum of CO for one of these excitation schemes.

3.1 Excitation schemes

In Figure 14 the energy scheme of CO is shown schematically, with the most relevant electronic states indicated. Multiple excitation schemes for TALIF on CO have been applied [86]. Excited states that can be populated by TALIF are the $\mathrm{B}\,^1\Sigma^+$, $\mathrm{C}\,^1\Sigma^+$, $\mathrm{E}\,^1\Sigma^+$, $\mathrm{A}\,^1\Pi$ singlet states, as well as the triplet $\mathrm{a}^3\Pi$ state. Next to this figure the excitation and fluorescence wavelengths are displayed, together with some guiding remarks.

Three of these states are discarded based on these remarks, the $\mathrm{E}\,^1\Sigma^+$, $\mathrm{A}\,^1\Pi$ and $a\,^3\Pi$ states. This leaves the $\mathrm{B}\,^1\Sigma^+$ and $\mathrm{C}\,^1\Sigma^+$ states. Excitation in these schemes happen in the Hopfield-Birge system. Transitions in this system are singlet-singlet transitions, as well as $\Sigma \rightarrow \Sigma$ transitions, therefore $\Delta\Lambda = 0$. Electrons from both the $\mathrm{B}\,^1\Sigma^+$ and $\mathrm{C}\,^1\Sigma^+$ states fall back to the $\mathrm{A}\,^1\Pi$ state, thereby emitting fluorescence in respectively the Ångstrom or Herzberg systems. This is then a $\Sigma \rightarrow \Pi$ transition, having $\Delta\Lambda = -1$. Both these excitation schemes are elaborated on in sections 3.1.1 and 3.1.2.

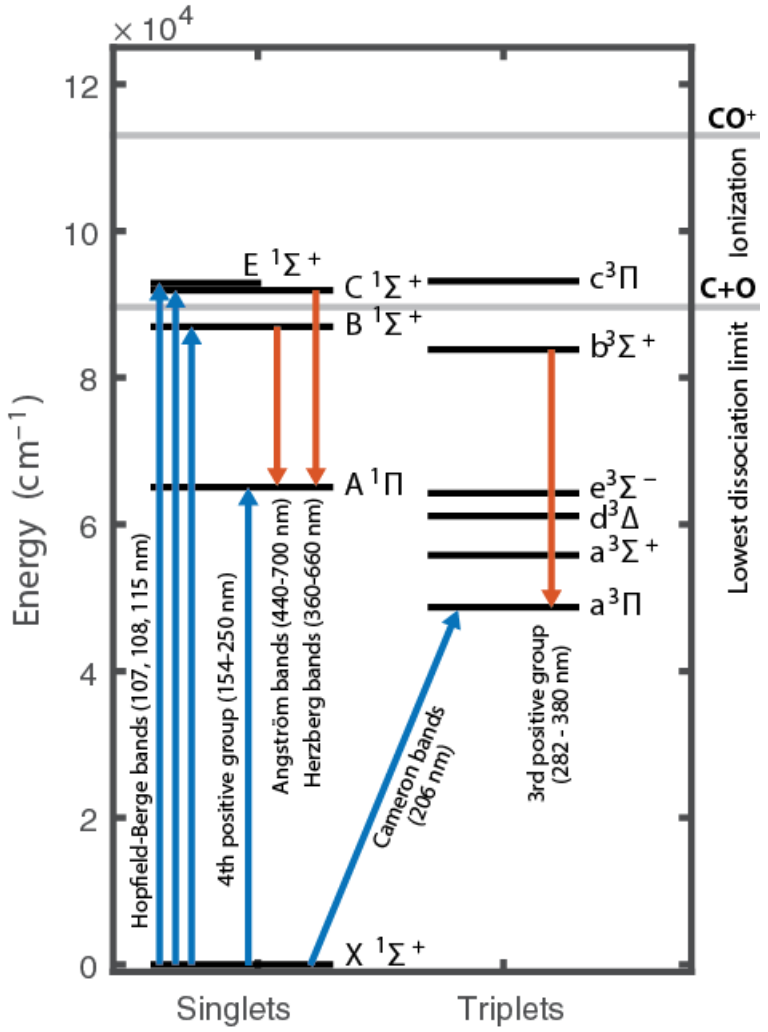

Figure 14 Schematic overview of the excited states of CO, with possible excitation routes and their fluorescence. Energies (and wavelengths) are given for one-photon transitions. Also indicated is the lowest dissociation limit and the ionization limit. Figure based on [87]*, data from* [54][88][89]

- **$A\,^1\Pi$ state** [90][91][92]
  - Excitation: 154-250nm
  - Fluorescence to $X\,^1\Sigma^+$ at 154-250nm

This electronic level can be reached through one-photon excitation. The single photon-absorption rate is much higher than that of two-photon processes. The downside of this state is that the fluorescence has the same wavelengths as the excitation laser. Furthermore the fluorescence is in the UV range, making detection challenging.

- **$a\,^3\Pi$ state** [93][94][89]
  - Excitation: 206nm
  - Fluorescence to $X\,^1\Sigma^+$ at 206nm

Exciting to this triplet can state can be done with single-photon LIF. However excitation to this state has a high quantum efficiency for enabling photochemistry. Excitation to and fluorescence from this state is spin-forbidden, making this state a metastable, thus giving it a very long lifetime, in the order of miliseconds.

- **$B\,^1\Sigma^+$ state** [86][95][96]
  - Excitation: 230nm
  - Fluorescence to $A\,^1\Pi$ at 440-700nm

This excitation scheme is well characterized and applied in combustion research, which is further detailed in the next sections.

- **$C\,^1\Sigma^+$ state** [86][95]
  - Excitation: 217nm
  - Fluorescence to $A\,^1\Pi$ at 330-600nm

Excitation to this state is a valid option, which is investigated as an attractive alternative to the often applied $B\,^1\Sigma^+$ scheme, further detailed in the next sections.

- **$E\,^1\Sigma^+$ state** [97]
  - Excitation: 215nm
  - Fluorescence to $A\,^1\Pi$ at 340-550nm

The $E\,^1\Sigma^+$ state lies completely above the dissociation limit and has a very low quantum yield, making it an unattractive option.

3.1.1 TALIF on CO to the $\mathrm{B}\,^1\Sigma^+$ state

TALIF on the $\mathrm{B}\,^1\Sigma^+$ state of CO is well characterized [91][96] [98]. The advantage of doing TALIF on this state is that it is not above the dissociation limit, and the fluorescence to the $\mathrm{A}\,^1\Pi$ state is emitted in the Ångstrom band [54], which lies in the visible light range, making detection easier.

The excitation scheme to the $\mathrm{B}\,^1\Sigma^+(v=0)$ from the ground state $\mathrm{X}\,^1\Sigma^+(v=0)$ requires two photons of 230.1nm. Since this excitation scheme has been studied quite extensively, absorption cross sections of the $\mathrm{B}\,^1\Sigma^+$ are known [91], as are photoionization rates [99] and the collisional quenching coefficients, including self-quenching and quenching with species of interest such as CO_2 and nitrogen [98]. The natural lifetime of this excited state is approximately 22.8ns [96]. For low pressures, $p \approx 1\mathrm{mTorr}$, the natural lifetime is the lifetime of the fluorescence. For higher pressures in the range of 200mTorr, an increase in lifetime is observed to about 65ns. This is attributed to the increasing opacity of the medium, so radiation trapping starts to occur [96]. For a further increase in pressure the lifetime of the excited state starts to decrease due to collisional quenching effects. For pressures above 10 Torr the lifetime of the CO has decreased by an order of magnitude compared to the natural lifetime. This pressure dependence is illustrated in Figure 15. In this work TALIF on CO is performed at pressures not lower than 10 Torr, which means the effective lifetime will be in the range of $1-2\mathrm{ns}$, and the rise in lifetime for very low pressures cannot experimentally be observed.

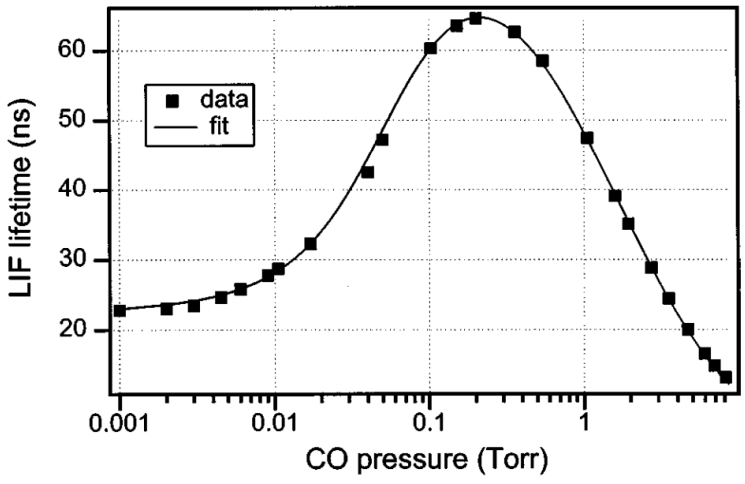

Figure 15 Lifetime of the fluorescence of the $B\,^1\Sigma^+$ state of CO in nanoseconds as a function of pressure, given in Torr. Figure from Teodoro et al, 2000, J. Chem. Phys. [96]

Collisional quenching of the $\mathrm{B}\,^1\Sigma^+$ can introduce a new fluorescence path, which is shown in Figure 14 as fluorescence coming from the $\mathrm{b}\,^3\Sigma^+$ state [95]. Collisions induce a transition from the singlet $\mathrm{B}\,^1\Sigma^+$ to the $\mathrm{b}\,^3\Sigma^+$ triplet state. The emitted fluorescence from this state is the third positive system having wavelengths of 280-380nm. TALIF measurements on the $\mathrm{B}\,^1\Sigma^+$ state of CO also report disturbances of the measurements with radiation not coming from CO. This is attributed to crosstalk of C_2 [100]. Fluorescence emitted in the Swan system of the C_2 molecule has a similar structure compared to the radiation coming from $\mathrm{B}\,^1\Sigma^+ \rightarrow \mathrm{A}\,^1\Pi$ transitions. The excited state in the Swan bands can be populated by photons of 230nm [86][101]. Since this is a one-photon process the cross-section for this excitation is expected to be much larger than the two-photon excitation cross section of CO. Very small amounts of

C_2 can therefore already provide a large distortion of the TALIF signal of CO. The presence of C_2 is common in combustion research, however Kwak *et al*, have also reported the presence of C_2 in a plasma discharge [102]. Furthermore, photo dissociation of CO by the 230nm radiation can produce C_2 [103]. A separate crosstalk channel comes from the Raman signal of N_2 [86], which is not expected to be a problem, since nitrogen is not included in these measurements.

Figure 16 shows the spectra of the Angstrom bands of CO and the Swan bands of C_2. This figure shows a large overlap in almost all the vibrational bands, therefore indicating that C_2 crosstalk might be a complicating factor in obtaining reliable results. This figure also shows the fluorescence emitted in the third-positive group as the fluorescence bands in the range of 280-380nm.

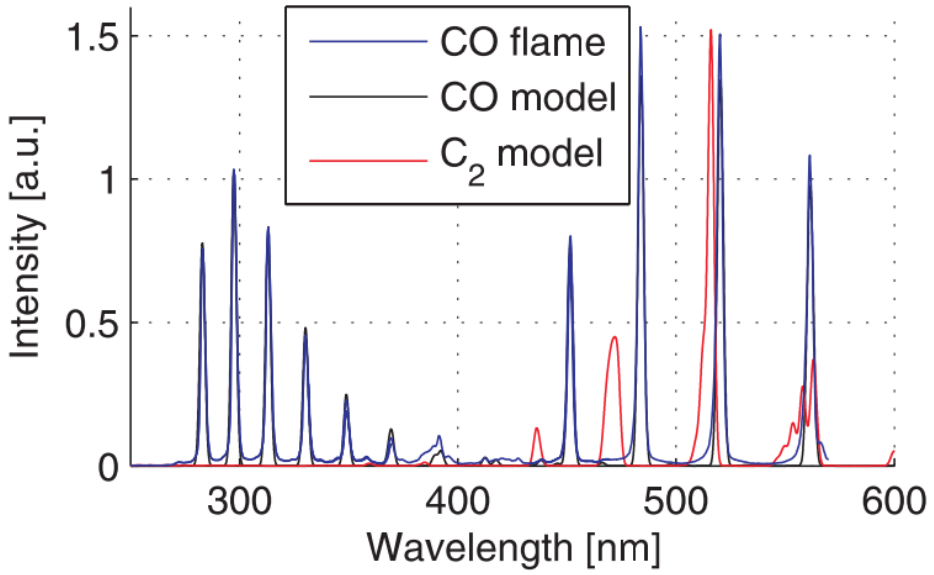

Figure 16 Comparison of the emission spectra of the Angstrom bands of CO and the Swan bands of C_2 in a flame and in models. The emission in the UV range is caused by emission of third positive group, which gets populated by quenching of the $B\,^1\Sigma^+$ state. Figure taken from [95].

3.1.2 TALIF on CO to the $C\,^1\Sigma^+$ state

Two photon absorption laser induced fluorescence to the $C\,^1\Sigma^+$ state of CO is very similar to that of the $B\,^1\Sigma^+$ state. Fluorescence from the $C\,^1\Sigma^+$ to the $A\,^1\Pi$ is the Herzberg band, instead of the Ångstrom band. The Herzberg band has the highest energies on the edge of the UV region, at a wavelength of 360nm. This is associated with the $v' = 0 \rightarrow v'' = 0$ transition. Transitions to different vibrational bands of the $A\,^1\Pi$ state have wavelengths in the visible regime, comparable to fluorescence from the $B\,^1\Sigma^+$ state.

There are two main differences between the two states. At first, the $C\,^1\Sigma^+$ state has a natural lifetime of approximately 2ns [86] which is an order of magnitude shorter than that of the $B\,^1\Sigma^+$ state. Secondly this electronic state lies completely above the dissociation limit [54]. The much shorter lifetime has a big

effect on collisional quenching. Due to the shorter lifetime the CO molecules have a shorter timespan where they can lose their energy to collisions, thereby theoretically increasing the fluorescence yield. The second difference, this state lying above the dissociation limit, can cause extra losses. A collision of an excited molecule can easily lead to the dissociation of this molecule.

The shorter lifetime is one of the reasons why this excitation scheme is potentially useful, a second reason being that the oscillator strength for this transition is much stronger compared to the $B\,^1\Sigma^+$ [104], thereby hinting at a bigger absorption cross-section. A third reason this excitation scheme might be favorable is that the fluorescence is emitted at lower wavelength, more blue-shifted. This reduces the crosstalk with the Swan system of C_2 [86]. These three advantages make this a possible alternative to the often used $B\,^1\Sigma^+$ excitation scheme.

3.1.3 Direct comparison of the two schemes

Both of these excitation schemes were experimentally tested, especially to see if the $C\,^1\Sigma^+$ holds any compelling advantage over the $B\,^1\Sigma^+$ state. Much more information is available for the $B\,^1\Sigma^+$ state, such as the quenching cross-sections and the photoionization rates. Therefore if there is no significant advantage of the $C\,^1\Sigma^+$ state, or a disadvantage of the $B\,^1\Sigma^+$ state, the $B\,^1\Sigma^+$ state is chosen.

Figure 17 shows a time resolved TALIF signal of both excitation schemes at a pressure of 5mbar, indicating that it is possible to measure using both of these schemes. Due to the low natural lifetime of the $C\,^1\Sigma^+$ state no information about quenching can be obtained at all. In the measurement of the $B\,^1\Sigma^+$ state an effective lifetime can be calculated, which can give information on quenching through the Stern-Volmer methods. The decreased signal-to-noise for the measurement of the $B\,^1\Sigma^+$ state stems from a different setup of the photomultiplier tube used to measure this.

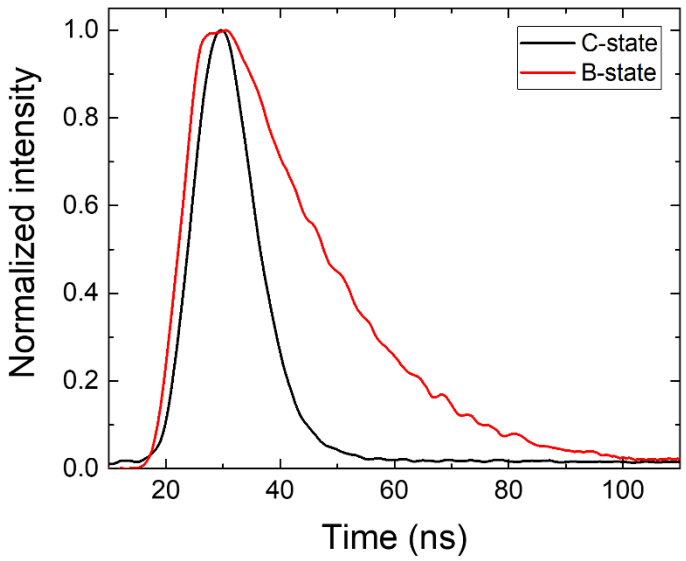

Figure 17 Time-resolved TALIF signal for the two excitation schemes, measured in 5mbar pure CO at room temperature, with a pulse energy of $50\mu J$ per pulse.

An excitation spectrum for both of these states is shown in Figure 18, also for a pressure of 5mbar. This shows that measuring an excitation spectrum is possible for both states, however this also does not provide any reason for the usage of the $C\ ^1\Sigma^+$ state. There is even a reason not to use this state, the separation of the peaks is slightly different compared to the $B\ ^1\Sigma^+$ state, which means the peaks of the $C\ ^1\Sigma^+$ state are spaced closer together, confirmed in Figure 18. This means these peaks are less resolvable, making data analysis more difficult. In the rest of this work therefore the $B\ ^1\Sigma^+$state is used.

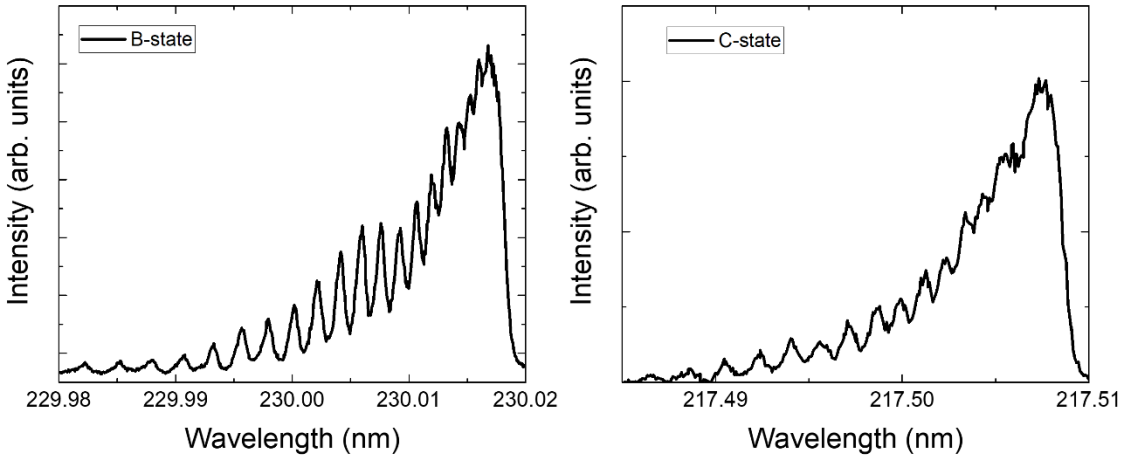

Figure 18 An excitation spectrum for the two considered excitation schemes, showing the ability to measure the rotational fringes. Both measurements are taken at a pressure of 5 mbar with a laser energy of $50\mu J$ per pulse.

3.2 Simulation of excitation spectrum

A simulation of the excitation spectrum of the $B\ ^1\Sigma^+$ state was done in order to better understand the mechanisms involved. In Appendix B the Matlab code which calculates this excitation spectrum is shown. Following is a short description of the simulation which calculates the excitation spectrum of the $B\ ^1\Sigma^+$ of CO state. This starts by calculating a stick spectrum, followed by the addition of line-broadening mechanisms to compute the absorption cross-section. As a final step this cross section is then convoluted with the laser line to give a total excitation spectrum.

3.2.1 Stick spectrum calculation

The first necessity in the calculation of a stick spectrum are the different physical constants of CO. These are required to compute the locations of the sticks. Next the line strength has to be computed, which depends on the Hönl-London factors, as well as the fractional population.

The locations of the sticks are computed by using equation (36), required for this are the rotational constant *B* and the centrifugal constant *D* for both states, as well as the difference in energy between the rotational and vibrational ground states of the $X\ ^1\Sigma^+$and $B\ ^1\Sigma^+$states. Table 2 shows these values which are required for the calculation of the stick spectrum.

Table 2 Constants of the ground and excited state of CO required for calculating the locations of the sticks in the stick spectrum. Data from[105]*, assuming only* $C^{12}O^{16}$

	$X\,^1\Sigma^+$	$B\,^1\Sigma^+$
w_0	–	86916.16cm^{-1}
B	1.922521cm^{-1}	1.9475cm^{-1}
D	$6.1138 * 10^{-6}\text{cm}^{-1}$	$6.1 * 10^{-6}\text{cm}^{-1}$

The next step in calculating the stick spectrum is computing the intensity of each line. The strength of each line is given by

$$S_{J'} = S_{vib,el} F_{J''} S_{J'J''}. \quad (71)$$

Here $S_{vib,el}$ is the electronic and vibrational part of the two-photon absorption cross section, which is independent on J. $F_{J''}$ is the fractional population in the ground state J'' and $S_{J'J''}$ is the two-photon Hönl-London factor [86].

The population of the ground state, $F_{J''}$, is assumed to be Boltzmann distributed, therefore

$$F_{J''} = \exp\left(-\frac{E_{J''}}{k_b T}\right) \quad (72)$$

where $E_{J''}$ is the rotational energy, calculated by equation (6), with the values for the $X\,^1\Sigma^+$state given in Table 2.

No P-and R-branches occur, which a is specific feature of $\Sigma^+ \rightarrow \Sigma^+$ two-photon transitions. In the simulation only the Q-branch is taken into account, since the intensities of the O-and S-branch are much lower compared to those of the Q-branch [87], which is experimentally confirmed by Tjossem *et al* [106]. These two branches are therefore neglected in the remainder of this work. The two-photon Hönl-London factors for the Q-branch of CO, $S^Q_{J'J''}$, are given by Bray and Hochstrasser [75] as

$$S^Q_{\Sigma\leftarrow\leftarrow\Sigma}(J) = \frac{(2J+1)}{9}\mu_I^2 + \frac{(2J+1)}{45(2J-1)(2J+3)}\mu_S^2 \quad (73)$$

with μ_I^2 and μ_S^2 invariants of the two-photon polarizability tensor, for which no absolute values are available. A comparison can however be made with linear to circular polarization ratios, described by Linow *et al* [86]. This gives

$$\frac{\sigma_{ll}}{\sigma_{cc}} = \lim_{J\rightarrow\infty}\frac{2}{3}\left(1 + \frac{10\mu_I^2}{\mu_S^2}\right) \quad (74)$$

where σ_{ll}/σ_{cc} is the polarization ratio, so the cross section of $B\,^1\Sigma^+ \leftarrow\leftarrow X\,^1\Sigma^+$ transitions for either linearly polarized light or circularly polarized light. Loge *et al* [87] have reported a value of 0.7:1 for this ratio, but this could not be unified with the theory of two-photon processes, as shown by Tjossem *et al* [106], who report $\frac{\sigma_{ll}}{\sigma_{cc}} \geq 300$ in the limit for large *J.* This value for the polarization ratio gives $\mu_I^2/\mu_S^2 \geq 30$, therefore the second term in equation (73) can be neglected. The factor $2J+1$ in this equation comes from the degeneracy of the ground state, which is only M degenerate, with M, ranging from $0, \pm1, \pm2, \ldots, \pm J$, therefore however apart from the degeneracy there is no change in line strength for increasing J, which is confirmed in the work of Di Rosa and Farrow [91].

Combining the locations of the sticks and their intensity gives a stick spectrum as shown in Figure 19, where it can be seen that for low values of $J = J' = J''$ the sticks are closely packed together and the intensity of each line is relatively large. As J increases, the spacing between the lines becomes bigger and the intensity decreases. The decrease in intensity is due to the decrease in population of the involved rotational levels in the electronic ground state.

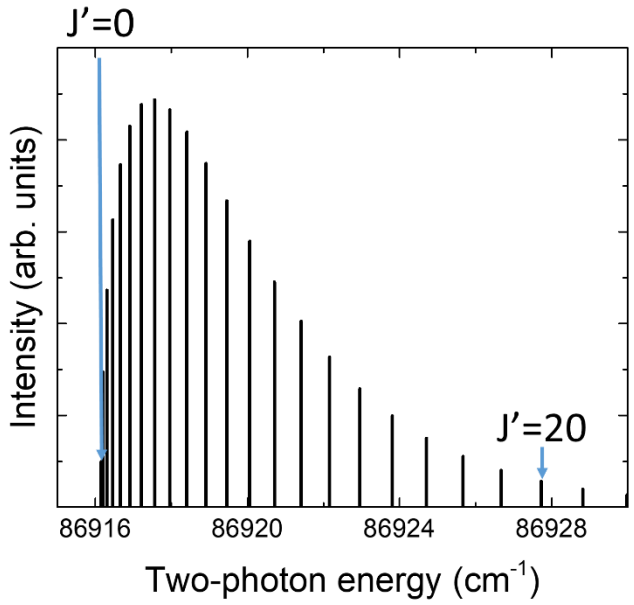

Figure 19 Calculated stick spectrum of the Q-branch of two-photon absorption on the $B\,^1\Sigma^+$ state of CO at a temperature of 300K. For low values of J'=J'' the sticks are closely packed, whereas for higher values of J the spacing between the sticks becomes larger, whereas the intensity becomes lower.

3.2.2 Full excitation spectrum

In order to expand the calculated stick spectrum of Figure 19 to a real spectrum, broadening mechanisms should be included. There are two types of broadening included in this model, Doppler broadening and pressure broadening. The collisional-and Stark-shifts are not taken into account, since the shift in energy associated with these processes is in the range of $10^{-2} - 10^{-1}\mathrm{cm}^{-1}$, and thus negligible [99][107].

Doppler broadening is caused by the distribution of velocities of the molecules present. The different velocities of the particles emitting light cause different Doppler shifts. The cumulative effect of all these shifts results in a broadened line with a Gaussian shape. The velocities of the molecules are purely thermal. Due to this thermal motion the standard deviation and full-width-half-maximum (FWHM) (in cm^{-1}) take the form

$$\sigma_f = \sqrt{\frac{kT}{mc^2}}\omega_0$$
$$2\gamma_D = \sqrt{\frac{8kT\log 2}{mc^2}}\omega_0 \qquad (75)$$

with *k* the Boltzmann constant, *T* the temperature in K, *m* the mass of the molecule in g, *c* the speed of light in ms^{-1} and ω_0 the central frequency of the Gaussian in expressed in cm^{-1} [108].

The second type of broadening that is significant, at least with the plasma operating at high pressures, 50-200mbar, is collisional broadening. Collisional broadening has a Lorentzian line profile of the form

$$I(\omega) = \frac{\gamma_{coll}/2\pi}{(\omega - \omega_0)^2 + \gamma_{coll}^2} \quad (76)$$

where γ_{coll} is the half-width of the Lorentzian and ω_0 is the central frequency [56]. The width for collisional broadening is generally expressed in the following form:

$$2\gamma_{coll} = P \sum_i X_i \gamma_i^{T_0} \left(\frac{295}{T}\right)^{m_i}. \quad (77)$$

Here γ_{coll} is again the half-width of the Lorentzian in cm^{-1}, and the summation is over all present species. P is the pressure in bar, X_i is the mole fraction of the ith species, $\gamma_i^{T_0}$ is the species-specific broadening at room temperature in cm^{-1}, T is the temperature in K, and m_i is a temperature scaling factor for each present species.

For TALIF on the on the Q-branch of the $\mathrm{B}\,^1\Sigma^+$ state of CO these collisional broadening parameters have been measured by Di Rosa and Farrow for different species [107], for the simulation a pure CO gas is assumed, reducing equation (77) to

$$2\gamma_{coll} = P * 0.74 \left(\frac{295}{T}\right)^{0.65}. \quad (78)$$

The total broadening is a convolution of the two profiles, giving a Voigt-profile, which cannot be explicitly expressed [61]. However, to speed up computational times an approximation is taken for a Voigt profile [109],

$$\sigma(\nu) = \sigma_0 \left\{(1-x)\exp(-0.693y^2) + \frac{x}{1+y^2} + 0.016x(1-x)\left[\exp(-0.0841y^{2.25}) - \frac{1}{1+0.0210y^{2.25}}\right]\right\}, \quad (79)$$

where σ_0 is the line strength of the transition, given by equation (71), $y = |\nu - \nu_0|, x = \frac{\gamma_{coll}}{\gamma_v}$. γ_{coll} is the half-width half maximum of the pressure broadening, and γ_v is the half-width of the Voigt profile, given by

$$\gamma_v = 0.5346\gamma_{coll} + \left(0.2166\gamma_{coll}^2 + \gamma_D^2\right)^{0.5} \quad (80)$$

where γ_D is the half-width of the Doppler broadening, given in equation (75).

Adding this broadening for every different stick for a temperature of 300K and a pressure of 50mbar gives a spectrum as shown in the red line of Figure 20.

It can be seen that barring the lowest J-values a rotational structure is visible. In the region from 86 916-86 917cm^{-1} the spectrum is highly convoluted, since the lines are spaced closely together. This simulation assumes an infinitely small laser linewidth. This is not realistic, therefore the effect the finite broadness of the laser has to be included. The laser for this simulation is assumed to have a Gaussian spectral profile with FWHM of $0.3\mathrm{cm}^{-1}$. The convolution of this Gaussian and the absorption cross-section simulates the effect the of the finite linewidth. This is shown as the dashed line of Figure 20.

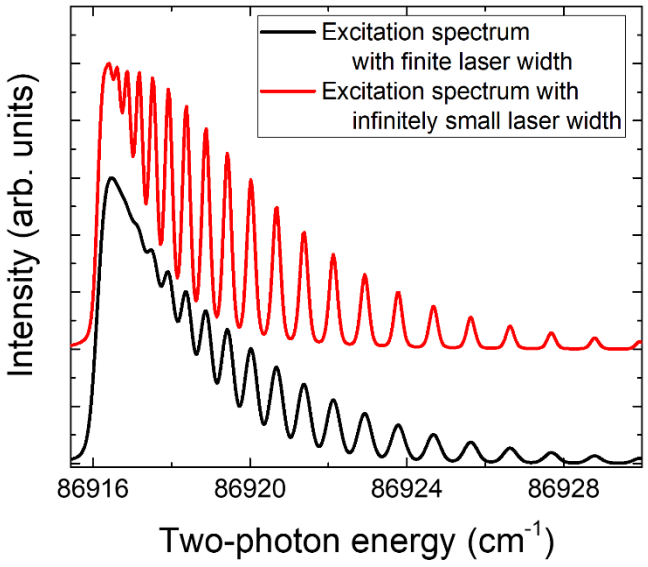

Figure 20 The dashed line shows the excitation spectrum when the finite width of the laser is included, the non-dashed line is the absorption cross-section if the laser would have an infinitely small linewidth, both spectra are calculated for a pressure of 100mbar a temperature of 300K and a laser linewidth FWHM of 0.3cm^{-1}.

Comparing the two spectra shows a lot of similarities, the shape is roughly the same, and the rotational peaks that can be observed are at the same wavenumbers. The main difference is that the individual peaks become resolvable at a higher rotational quantum number, the spectrum remains more convoluted for higher J values.

3.3 Simulation of fluorescence spectrum

In an actual experiment the fluorescence is measured, not the absorption, therefore it can be insightful to simulate this as well. Required for this simulation is knowledge of the $A\,^1\Pi$ state and of the Franck-Condon and Höln-London factors for fluorescence in a $\Sigma^+ - \Pi$ transition. The assumption is made that Kasha's rule does not apply to CO under the considered pressures, and therefore the fluorescence to the $A\,^1\Pi$ state only comes from the directly excited rotational states in the $B\,^1\Sigma^+$ state. This assumption seems valid when looking at experimental results obtained by Linow *et al* [86]. Changing the wavelength of the laser changes the wavelength of the emitted fluorescence. If Kasha's rule would be applicable this would not be the case, since all fluorescence would come from the rotational ground state. This assumption however means that it is required to calculate which rotational states in the $B\,^1\Sigma^+$ state get excited when the laser emits at a specific wavelength.

3.3.1 Energies of the $A\,^1\Pi$ state

To simulate the fluorescence to the $A\,^1\Pi$ state it is required to know the energies of rotational and vibrational states in this electronic level. Computing the energies can be done by using the Dunham expansion, which is detailed in section 2.1.3. The Dunham coefficients for this state are taken from Tilford and Simmons [105], and are displayed in Table 3.

Table 3 Dunham coefficients of the $A\,^1\Pi$ of CO given in cm^{-1}, taken from [105]

$Y_{01} = 1.612$	$Y_{11} = -2.33 \cdot 10^{-2}$	$Y_{21} = 1.59 \cdot 10^{-3}$	$Y_{31} = -5.71 \cdot 10^{-4}$	$Y_{41} = 8.24 \cdot 10^{-5}$	$Y_{51} = -5.94 \cdot 10^{-6}$	$Y_{61} = 2.11 \cdot 10^{-7}$
$Y_{10} = 1518.2$	$Y_{20} = -19.4$	$Y_{30} = 7.66 \cdot 10^{-1}$	$Y_{40} = -1.41 \cdot 10^{-1}$	$Y_{50} = 1.43 \cdot 10^{-2}$	$Y_{60} = -8.05 \cdot 10^{-4}$	$Y_{70} = 2.36 \cdot 10^{-5}$
$Y_{02} = 7.29 \cdot 10^{-6}$	$Y_{12} = -1.05 \cdot 10^{-7}$	$T_{e0} = 63994$				

Using these coefficients the energies of all rotational and vibrational levels of the $A\,^1\Pi$ state with respect to the ground state can be calculated. T_{e0} gives the difference in energy between the ground states of the $X\,^1\Sigma^+$ and $A\,^1\Pi$ states, to make it comparable to the energies of the $B\,^1\Sigma^+$ state. Figure 21 shows the energies of the different vibrational excitations. These in turn are made up of a rotational structure, which is shown for the vibrational ground state in the inset. For clarity only the first 10 rotational states are shown in the figure, the model however can compute up to an arbitrarily large J.

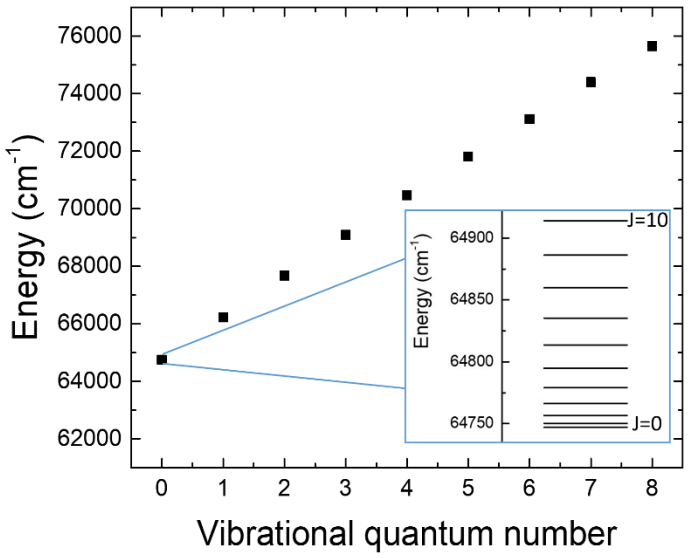

Figure 21 Energies of the different vibrational states of CO, with in the inset the rotational structure of one vibrational state.

3.3.2 $B\,^1\Sigma^+ \rightarrow A\,^1\Pi$ transitions

Excited molecules in the vibrational ground state of the $B\,^1\Sigma^+$state can fall back to different vibrational levels in the $A\,^1\Pi$ state, there are no selection rules for such transitions, instead the vibrational transitions are governed by the Franck-Condon principle [68]. Rotationally, the excited molecules fall back from the rotational state they are excited to by the laser. For $\Sigma \rightarrow \Pi$ transitions there are three different branches, the P, Q and R branch, for respectively a ΔJ of -1,0 and +1 [69].

As detailed in section 2.2.1 the Franck-Condon factors govern which vibrational states in the $A\,^1\Pi$ state get excited. The Franck-Condon factors are experimentally determined for these transitions in the Ångstrom system. They are shown in Table 4. This poses a limit for extending this simulation to the $C\,^1\Sigma^+$ state of CO. This system, the Herzberg band, has much less detailed Franck-Condon factors in literature, only extending up to the third vibrational state [54].

Table 4 Franck-Condon factors for the Angstrom band of CO, given for the first 9 vibrational states of the $A\,^1\Pi$ state. Data from [65][110][111][112][113][114].

$v' \rightarrow v''$	Franck Condon Factor
$\mathbf{0 \rightarrow 0}$	0.08898
$\mathbf{0 \rightarrow 1}$	0.18159
$\mathbf{0 \rightarrow 2}$	0.21056
$\mathbf{0 \rightarrow 3}$	0.18339
$\mathbf{0 \rightarrow 4}$	0.13399
$\mathbf{0 \rightarrow 5}$	0.08706
$\mathbf{0 \rightarrow 6}$	0.06211
$\mathbf{0 \rightarrow 7}$	0.02094
$\mathbf{0 \rightarrow 8}$	0.01591

The three different rotational branches each have a specific line strength, governed by the Hönl-London factor. This means that each rotational line in the $\mathrm{B}\,^1\Sigma^+$ state can fall back to three different rotational states in each vibrational band. The Höln-London factors for $\Sigma \rightarrow \Pi$ transitions, with $\Delta\Lambda = -1$ are detailed by Kovacs [69], where $\Lambda_B = 0$ is already taken into account. This gives:

$$S^Q_{\Sigma\rightarrow\Pi} = \frac{(2J'+1)}{2}$$
$$S^P_{\Sigma\rightarrow\Pi} = \frac{(J'+1)(J'+2)}{2J+1} \qquad (81)$$
$$S^R_{\Sigma\rightarrow\Pi} = \frac{(J'-1)}{2}$$

with *S* is the line strength. As can be seen this is independent on vibrational quantum number. Using these relations and the Franck-Condon factors every line strength for every possible transition can be computed. For every rotational line in the $\mathrm{B}\,^1\Sigma^+$ state there are nine different possible vibrational states that can be populated when a CO molecule de-excites. Three rotational states can be excited in each vibrational band, due to the three branches.

Figure 22 shows the fluorescence spectrum if only one rotational state in the $\mathrm{B}\,^1\Sigma^+$ state were excited, where each vibrational band consists of three rotational lines, one for each of the branches. Collisional broadening and Doppler broadening are added to this figure, however they are barely distinguishable, the linewidth of both broadening mechanisms is in the range of $10^{-1}\ \mathrm{cm}^{-1}$, whereas the whole spectrum covers a range of approximately 10^4 wavenumbers. The dominating broadening mechanism in a spectrally resolved experiment covering this wavelength range will therefore be instrumental broadening.

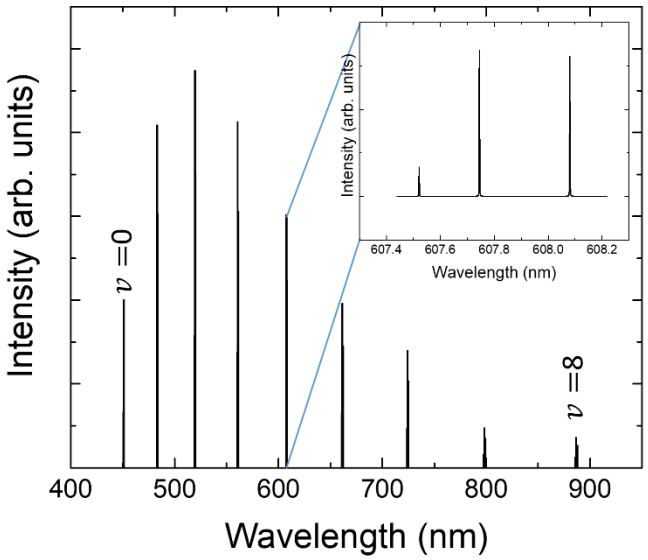

Figure 22 The fluorescence spectrum that one excited rotational state in the B-state emits. The inset shows a zoom-in on the fourth vibrational band, thereby showing the three different rotational branches.

3.3.3 Overlap with the laser

The relative strength of transitions to the excited state not only depends on the line strength, governed by the Franck-Condon and Hönl-London factors, but also on the overlap integral with the laser, discussed in chapter 2. It is assumed the spectral profile of the laser is Gaussian. The upper level of a transition gets excited proportional to the overlap of the spectral profiles of the laser and this transition. This mechanism will therefore populate certain J values in the $\mathrm{B}\,^1\Sigma^+$ state. It is assumed there is no change in rotational value before these excited molecules emit fluorescence.

For a fixed laser-wavelength the fluorescence spectrum is shown in Figure 23 with in the inset a zoom in on one of the vibrational bands. There are more transitions compared to Figure 22, which can be explained by the laser overlapping with multiple transitions. Each excited transition again consists of three fluorescence branches.

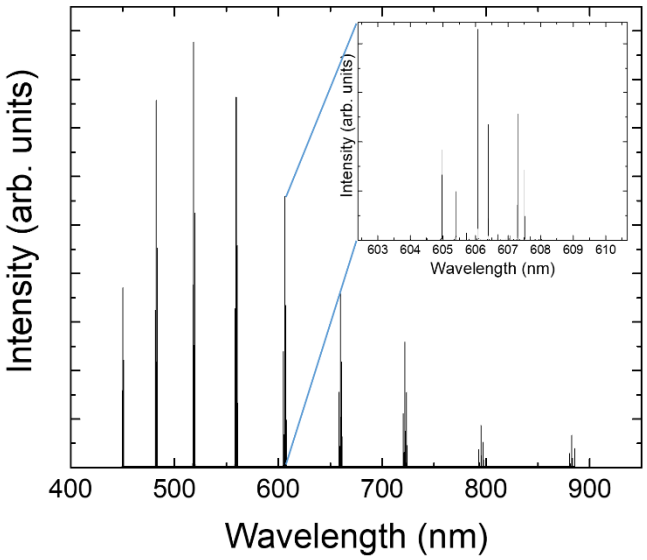

Figure 23 Simulated fluorescence spectrum where the states being excited are calculated by the overlap integral of this transition with the laser. The laser has a wavelength of 230.1nm, and a width of 0.09cm^{-1}. A zoom in on the fourth vibrational band is shown in the inset.

It is also possible to simulate a laser scan over all the different excitation wavelengths. Then the procedure used to generate Figure 23 iterates over a set of laser wavelengths, integrating the total fluorescence at each wavelength. The integral of the output can be plotted as a function of laser wavelength, giving the same result as Figure 20 if the steps between laser wavelengths are small enough. This is shown in Figure 24. For comparison the calculated convolution of the absorption cross-section with the laser is included as well, both are computed for a temperature of 300K, a pressure of 100mbar and a laser line-width of $0.09\mathrm{cm}^{-1}$, which is based upon the laser specifications.

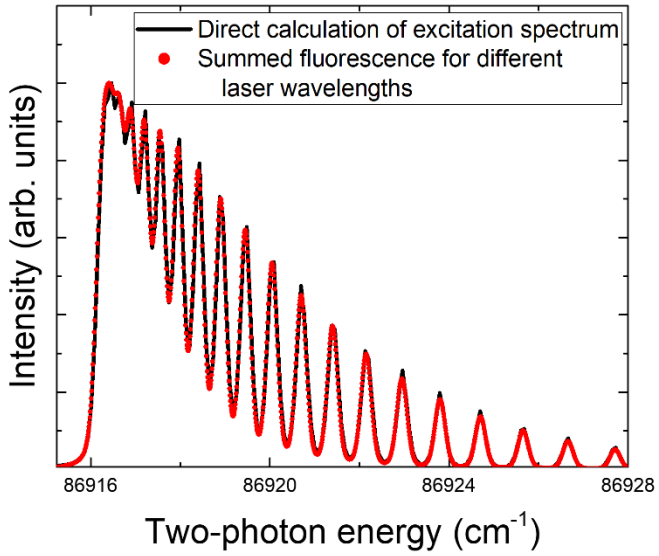

Figure 24 Simulated laser scan, computed by calculating the fluorescence emitted by the system at different wavelengths, calculated at a temperature of 300K and a pressure of 100mbar, shown as the red points, together with the black line, which is the spectrum from Figure 20.

The two absorption spectra are exactly the same. The way both simulations are created makes sure that this is the case, since no quenching processes are taken into account, therefore every excitation of a CO molecule eventually leads to a photon that goes into one of the fluorescence bands. Therefore the excitation spectrum is perfectly recreated by integrating the fluorescence for different wavelengths.

The simulation of the excitation spectrum can be validated with a comparison to similar TALIF on CO studies. Di Rosa and Farrow have a more complete simulation taking into account absorption before the focal point as well as photo-ionization and collisional quenching, this to measure the absolute cross-section [91]. Since that is outside of the scope of this work this is not taken into account in this simulation. The simulation of Di Rosa and Farrow is shown in Figure 25a, whereas in Figure 25b the simplified simulation is shown. The excitation spectrum of Figure 25b is calculated under the same conditions as that of Figure 25a. These figures are very similar, thereby qualitatively confirming the validity of the simulation.

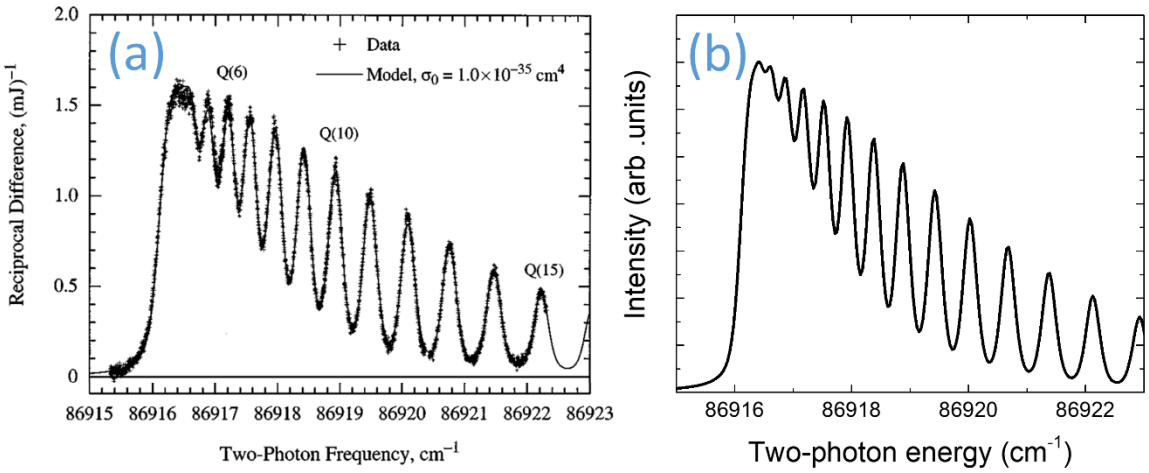

Figure 25 Comparison between a simulation performed by Di Rosa and Farrow, overlaid with experimental data, taken from [91]*, shown in (a), and the developed simulation calculated for the same conditions, shown in (b). Conditions are a pressure of 173mbar, room temperature, and a laser linewidth of 0.004cm^{-1}.*

4. Experimental setup

The experimental setup is split in two parts, at first the generation of the excitation wavelength is discussed and secondly the vacuum and detection systems are detailed. Finally the procedure on how to measure an excitation spectrum is detailed.

4.1 Generation of excitation laser

In this section the method to generate a 230nm laser pulse is discussed. Schematically this part of the experimental setup is shown in Figure 26.

Laser light of 1064nm is emitted by a Nd:YAG-laser (Spectra Physics Quanta Ray Pro 290-30), having a pulse length of 10ns and a frequency of 33Hz. This light is frequency tripled to 355nm by at first frequency doubling to 532nm, and subsequent sum-frequency generation. The 355nm light is coupled into a dye laser (Sirah Lasertechnik PrecisionScan). The pump beam emits on the laser dye (Exciton Coumarin 460, diluted in ethanol) to create a laser beam with a tunable wavelength around 460nm. This tuning can be done by changing the angle of the grating in the dye laser. This grating has a length of 90mm and 3000 lines/mm.

For TALIF on CO light of 230nm is required. Therefore a second harmonic generation (SHG) BBO crystal is put into the beam, creating a laser pulse of 230nm. The efficiency of the SHG-crystal for different wavelengths is very sensitive to the angle under which the laser pulse hits the crystal. Due to this angle the beam is displaced slightly, therefore a compensator is in place to compensate for this displacement. The SHG crystal changes the spectral width of the laser pulse, according to the manufacturer by no more than a factor 1.5 [115].

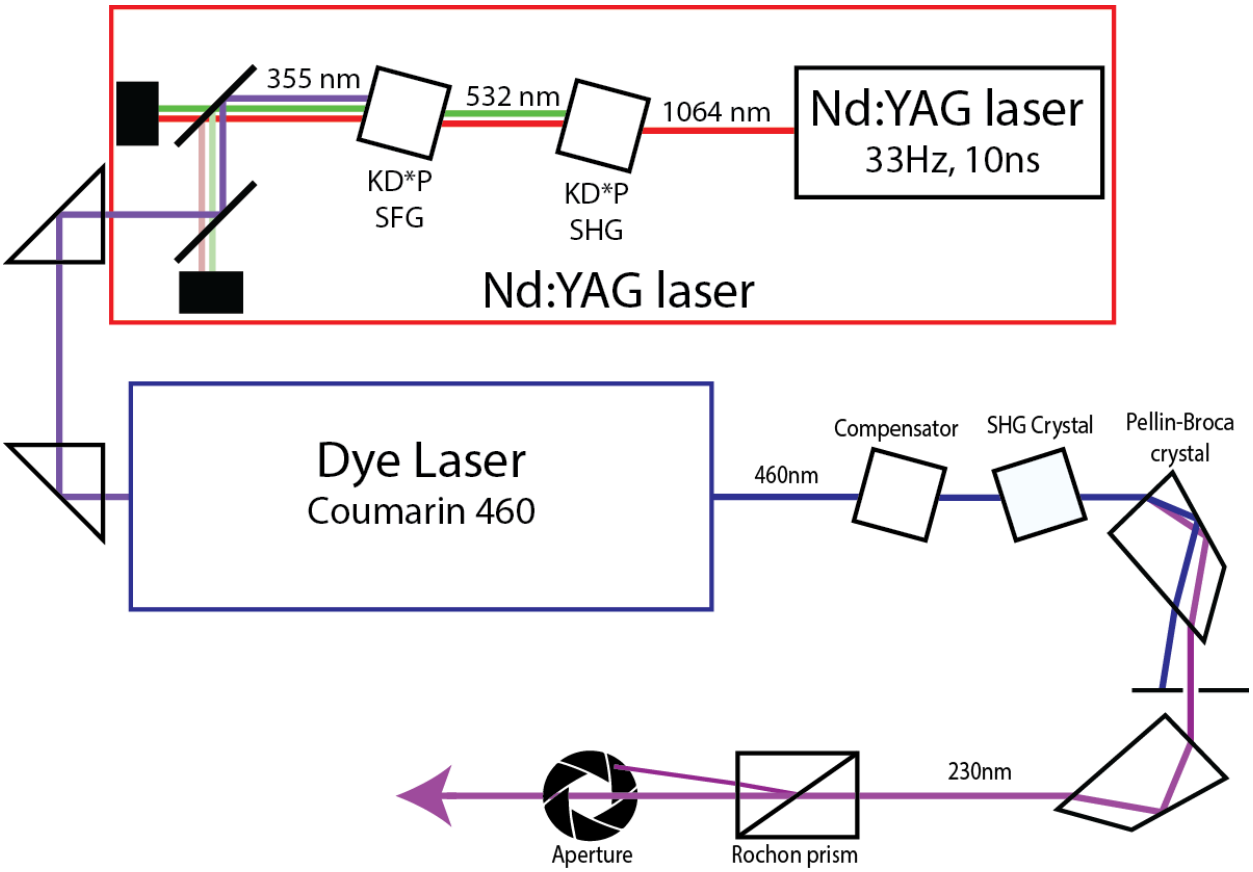

Figure 26 Schematic display of a part of the experimental setup which creates the 230mn pulse. The setup consists of the Nd:YAG laser and the dye laser, with the most important elements of the lasers displayed. Fundamental light of 460nm coming from the dye laser is frequency doubled, after which the remaining 460nm light is filtered out using two Pellin-Broca prisms. Finally there is a Rochon prism to attenuate the laser power.

The laser pulse still contains a significant amount of fundamental 460nm light, therefore two Pellin-Broca crystals are placed after the frequency doubling crystal and the compensator. These crystals filter out most of the 460nm pulse.

Control over the laser output power is crucial in a TALIF experiment. The laser power determines in which LIF regime the setup operates. If the setup operates in the linear regime the detected signal depends on the square of the input power, and is therefore very sensitive to changes in the laser power. A method to control the laser power is included in the system, in the form of a Rochon prism. A Rochon prism consist of two prisms that are cemented together [116]. At the interface of the two prisms a deviating beam is generated. The amount of laser-power that goes into the deflected beam depends on the angle between the prism and the polarization of the beam. Therefore by changing the angle of the Rochon prism the laser power can be tuned, since the dye laser emits vertically polarized light.

4.2 Detection system

The second part of the experimental setup is shown in Figure 27. The attenuated beam of 230nm light is focused by two lenses, $\left(F_1 = -200, F_2 = 100, (UV\ Fused\ Silica\ (UVFS)\right)$ into a gas chamber where various gases can flow through. In this quartz tube the fluorescence is detected at the focal point of

these lenses, where the laser power density is highest. The fluorescence is imaged into a fiber $(d = 500\mu\text{m})$ by two lenses $(F_3 = 70, F_4 = 30, UVFS)$. This fiber then leads to a photomultiplier tube (PMT) (Hamamatsu R12829) which is connected to an oscilloscope connected to a computer. It is possible to place a bandpass filter in front of the PMT to filter out almost all of the ambient light.

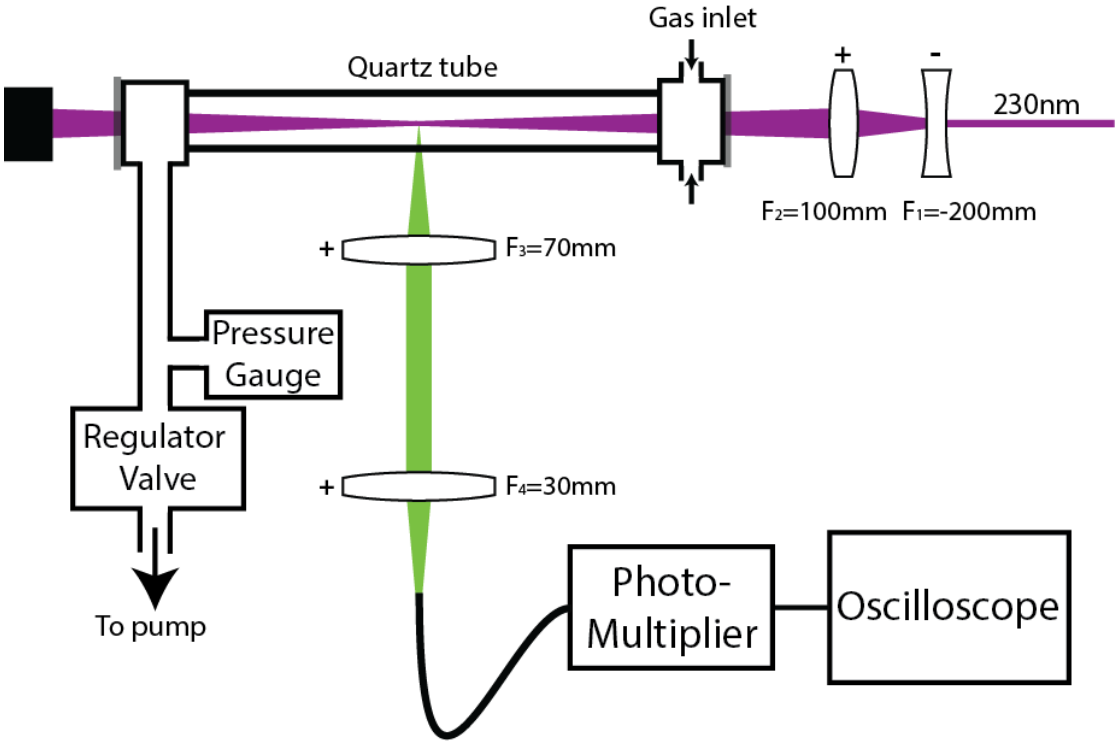

Figure 27 Second part of the experimental setup, showing the vacuum and detection systems. The excitation beam of 230nm is focused into the reactor, where fluorescence is detected at a 90° angle. This fluorescence is imaged into a fiber which leads to a photomultiplier tube, which is connected to an oscilloscope. The vacuum system consists of a vortex flow injector, a vacuum reactor. The pressure is measured using a pressure gauge and controlled using a valve. The base pressure of the system is in the order of $10^{-2}mbar$.

The TALIF signal can also be spectrally resolved by a spectrometer (Andor Shamrock i303), this cannot be used at the same time as the photomultiplier. The downside of using a spectrograph is the speed of taking measurements. The spectrometer requires a fairly long exposure time, and measuring as well as saving data is fairly slow. A photomultiplier tube on the other hand does not require a long exposure, and the speed of taking measurements is purely limited by the speed of the oscilloscope.

The vacuum system is also shown in Figure 27. A vortex flow injector creates a vortex flow in the middle of the tube, this to try to prevent a future microwave plasma from hitting the quartz and heating it too much. The gas goes through the reactor, to a pressure gauge (Pfeiffer Vacuum CMR-361). The pressure is regulated using a valve.

4.3 Measuring an excitation spectrum

Experimentally, a scan over the complete ground-state is required to measure the excitation spectrum and to subsequently fit it. A custom software was created for this purpose. This software changes the position of the grating and the BBO crystal in the dye laser, while saving the fluorescence collected with

the PMT. A backlashing mechanism is included for the motors inside the dye laser to prevent any hysteresis effect. The photomultiplier tube measures a signal that is a function of time. Such a measurement is displayed in Figure 28.

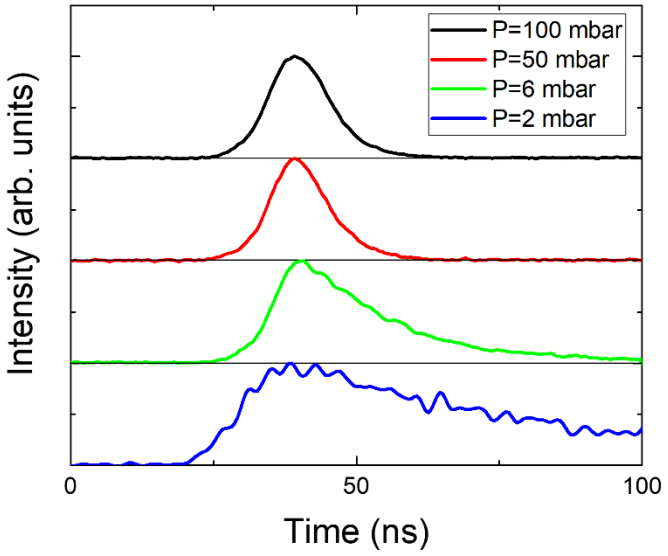

Figure 28 Measured TALIF signal as a function of time for different pressures, illustrating the effect of pressure on the quenching rate, therefore on the effective lifetime.

Here for several pressures the TALIF signal as a function of time is shown, highlighting the decrease in effective lifetime with increasing pressure, which can be rephrased as an increase in collisional quenching with increasing pressure. This effect was previously illustrated in Figure 15. This figure is illustrative as to why in this work the focus lies on measuring temperatures and not density. For pressures above a certain threshold, in pure CO $\sim 50\text{mbar}$, the laser pulse becomes nearly indistinguishable from the time evolution of the TALIF signal. This makes it nigh impossible to characterize the quenching through the theory of chapter 2. If quenching is not properly characterized nothing can be said about densities. In a mixture of CO_2 and CO the pressure where the effective lifetime cannot be measured is even lower, since CO_2 is a more effective quencher than CO [96][98].

The fluorescence signal as a function of time is integrated. This gives one data point for the excitation spectrum, where the wavelength corresponding to this data point is determined by the angle of the grating. Then as the grating changes its angle, a different wavelength is selected, and thus a different time resolved signal is measured and integrated. This scan is done over all the wavelengths where fluorescence can be detected, to finally give an excitation spectrum. Figure 18 already showed a measured excitation spectrum at room temperature and at a pressure of 5 mbar.

5. Data Processing

In the previous chapter the procedure of measuring an excitation spectrum is explained. Discussed in this chapter are the steps to come from a measured excitation spectrum to a temperature. This details the data-fitting procedure, which builds upon the simulation discussed in section 3.2. Furthermore the wavelength axis is calibrated, the linewidth of the laser is checked, operation in the linear regime is validated, the option of measuring using a bandpass filter is investigated, and finally a measured excitation spectrum is fitted to the simulation.

To obtain the temperature from a measured excitation spectrum an iterative process is applied. The theoretical excitation spectrum at a specific temperature can be calculated and then iteratively fitted to the measurement. The computation of this excitation spectrum starts by calculating the positions of sticks of individual transitions, based on spectroscopic constants. The intensity of each stick is then computed based on the temperature. These sticks are broadened by Doppler and collisional broadening. Subsequently the whole spectrum is convoluted with the spectral profile of the laser to account for its finite linewidth. This yields an excitation spectrum for a specific temperature, which can then be fitted to the data in an iterative process.

The computation of an excitation spectrum is treated in more detail in section 3.2. Appendices A & B show the applied Matlab code, where Appendix A shows the code to treat the data and Appendix B shows the code to generate an excitation spectrum, which is applied in the code of Appendix A. Temperature is the main fitting parameter in this code. In Figure 29 the effect of temperature on a calculated excitation spectrum is shown.

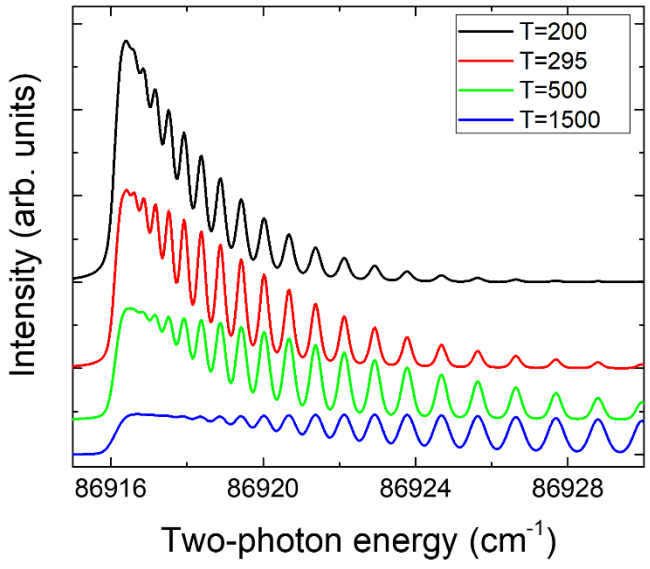

Figure 29 Effect of temperature on the excitation spectrum, calculated with using the described simulation, with a laser width of 0.09cm^{-1} at a pressure of 100mbar. The area under the spectra are normalized.

The main effect of temperature is the change in population of rotational levels in the ground state. For increasing temperature increasingly large J values will be populated, since they will be closer to the thermal energy, kT. Temperature also has an effect on the two intrinsic broadening mechanisms, collisional and thermal broadening. The width of collisional broadening of CO scales with $T^{-0.65}$, whereas Doppler width scales as $T^{0.5}$. The similar scaling factors ensure that a higher temperature increases the Doppler width, but simultaneously decreases the collisional width with a very similar factor. This makes it hard to numerically separate the two broadening mechanisms, even though there is a large difference between the tail of a Gaussian and a Lorentzian.

5.1 Calibration of the wavelength

Fitting a computed excitation spectrum to experimental data is very sensitive to the wavelength. A wrongly aligned wavelength axis where the laser does not scan linearly or reproducibly puts the rotational peaks at slightly wrong positions. This introduces fitting inaccuracies, since the code does not automatically corrects for this.

The wavelength axis of a measurement is directly given by the dye laser, and more specifically by the angle of the grating in the dye laser. For several laser scans this wavelength is checked using a wavemeter. A wavemeter uses a Fizeau interferometer to measure the absolute laser wavelength with extremely high accuracy [117]. Undoubled laser light of 460nm was coupled into the wavemeter, while simultaneously doing a wavelength scan. Figure 30 shows the wavelength of the laser as a function of the measured wavelength. If the laser is well calibrated a linear fit through this data should have a slope of 1. The linear fit however gives a slope of 0.96.

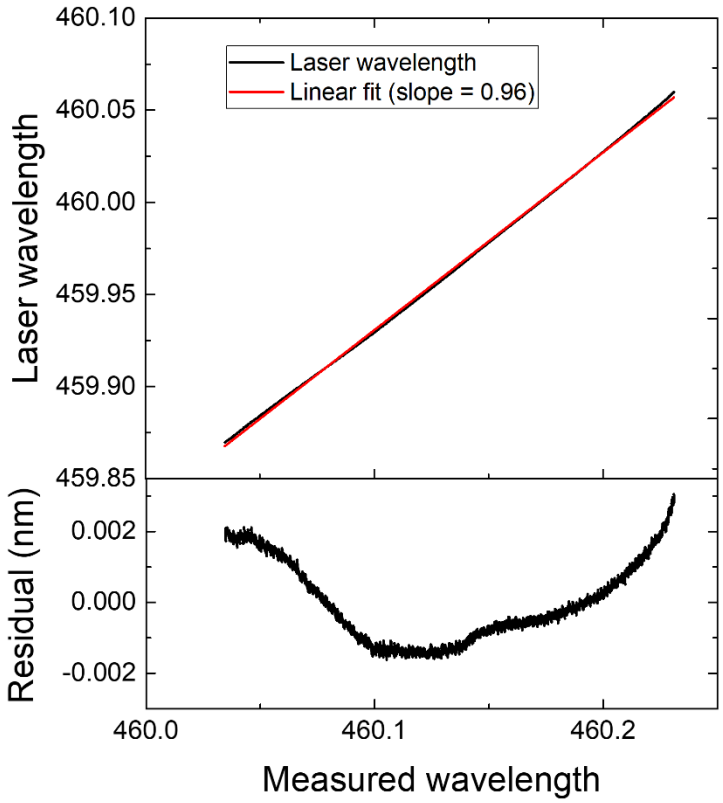

Figure 30 The wavelength of the laser as a function of the measured wavelength, together with a linear fit, which got a fitted slope of 0.96. In the bottom graph the residual of the fit is shown.

The bottom plot of this figure shows the residual of the fit and the measurement, showing very small deviations from linearity. Since the slope of the fit is not equal to 1 it can be concluded that the calibration of the software is not accurate. A second measurement was taken under exactly the same conditions right after the first measurement. This is done to check the reproducibility of a wavelength scan. The result of this measurement together with the one of Figure 30 is shown in Figure 31.

This figure again shows the measured wavelength and the wavelength determined by the grating position, from now on called the laser-wavelength. The bottom plot shows the difference between the laser and measured wavelengths for the two measurements. A laser scan goes from high to low wavelengths. Near the end of the scan, near the lowest wavelengths, the two lines overlap. This could hint at a hysteresis issue, however a mechanism to account for this is already included in the software. Also interesting is a sudden shift in lasing wavelength observed in the second measurement. It can be concluded that the laser does not scan perfectly reproducibly, and therefore it is not possible to make a wavelength calibration for all measurement, rather for each single measurement a calibration needs to be made separately.

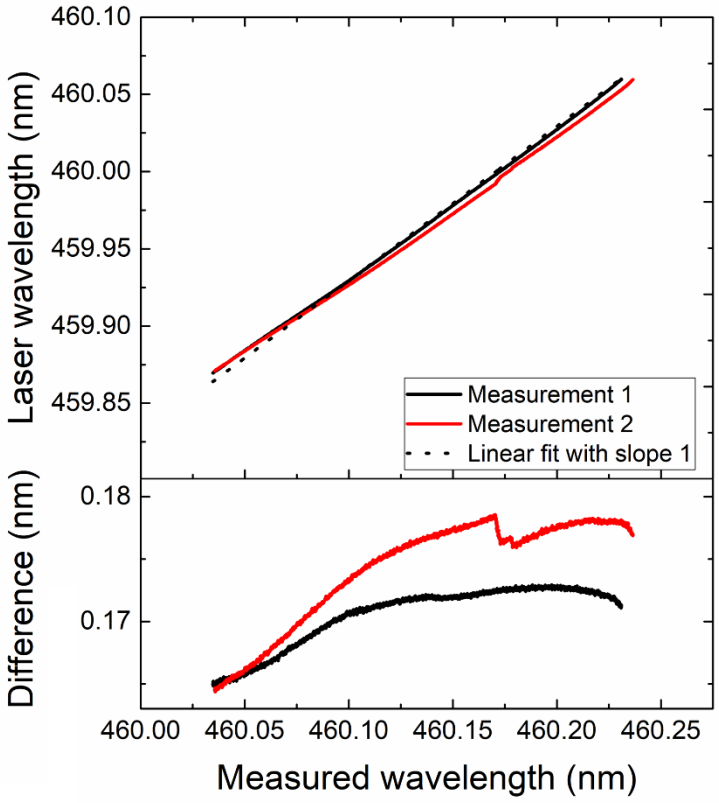

Figure 31 For two different measurements the laser-wavelength as determined by the grating is plotted as a function of the measured wavelength. In the bottom plot the difference with a linear fit of slope 1 is shown. The scan was performed from high to low wavelengths.

There are two ways to do this calibration, either by adding a Fabry-Perot interferometer to the setup, or by a numerical solution. A numerical solution introduces more possible errors, therefore the addition of a Fabry-Perot interferometer is preferred.

A Fabry-Perot interferometer, or etalon, consists of two reflecting surfaces parallel to each other. In such an interferometer multiple cycles of constructive and destructive interference occur over a wavelength scan, which give information over the scanning behavior. For the etalon to be applicable it needs to have enough fringes in a wavelength scan, especially since the deviations from linearity are small. An etalon was constructed for this purpose, however the housing only has space for a 4mm separation between the parallel reflectors. This gives a maximum free spectral range (FSR) of

$$f_{fsr} = \frac{c}{2nd} = 37.5\text{Ghz} = 1.25\text{cm}^{-1}. \quad (82)$$

The reflectors of this etalon were only suitable for the fundamental wavelength of the dye laser, the 460nm light. The results of measuring the intensity of light coming out of the etalon, together with a fit of this data are shown in Figure 32. Fitting data of an etalon was done by identifying the peaks and fitting each individual peak with a Gaussian.

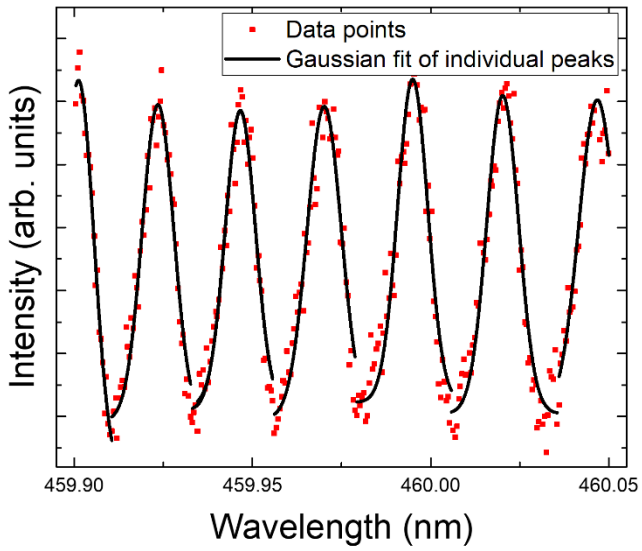

Figure 32 Intensity of the etalon as a function of laser wavelength, together with Gaussian fits of each local maximum.

This shows that this etalon is not perfectly suited for this purpose, the FSR of this etalon is too large to pick up the small wavelength changes, especially the abrupt changes as seen in Figure 30.

A more suitable interferometer would be required to have a larger separation between the mirrors, while preferentially being applicable for 230nm light. In a wavelength scan the frequency doubled beam covers a spectral range twice as big, whereas the linewidth scales with a smaller factor. The laser linewidth determines how small the FSR can become. No such etalon was available however, and a numerical solution is chosen.

This numerical option consists of calibrating the x-axis of the measurement using the measured data itself. This option is available due to the fairly large number of local maxima that can be identified in the excitation spectrum. These local maxima correspond to transitions of different J values, of which the energy is known. It is impossible to identify all the rotational lines in the low-J regime, which makes it challenging to assign a definite J value to each of these local maxima. However, due to the increasing separation between the peaks there is a solution where the energy of each measured local maximum is closest to the computed energy of a value of J. This is more clearly illustrated in Figure 33, where the peaks for a measured spectrum are all assigned a J value. The first observable peak corresponds in energy to the $J' = J'' = 4$ transition.

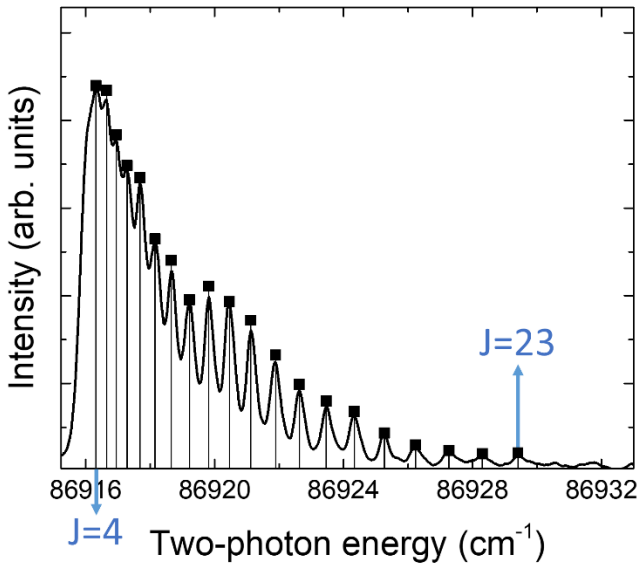

Figure 33 Identified peaks in a measurement, where the actual J-values belonging to these peaks are given for the first and last peaks.

For every observable local maximum the energy is given by the spectroscopic constants of CO. A calibration can now be made between the calculated energy and the one given by the data. This calibration is made by fitting a third order polynomial through this data. This both shifts the wavelength axis, as well as that it compresses and extends it at some points in order to generate the best fit of the computed spectrum to the measured one. In more noisy data it becomes harder to do this, especially in the region around $86917\mathrm{cm}^{-1}$. This method strongly depends on the correct identification of the peaks, and will fail if this identification is not done correctly. A combination of the two methods would probably yield the most accurate results. The etalon gives information on the linearity over a larger range, whereas the numerical method might pick up more sudden changes in wavelength.

5.2 Laser linewidth

The laser linewidth is an important parameter in the fitting process, since it determines, together with the other broadening mechanisms, how convoluted the excitation spectrum is. Therefore the laser linewidth provided by the specifications of the laser is checked. It is important to note here that this is a two-photon process, therefore two photons of 230nm are used, each photon having a Gaussian spectral

profile with a FWHM of $0.09\mathrm{cm}^{-1}$ according to the specifications. This is translated to a two-photon process by taking the convolution of two of these gaussians,

$$FWHM_{2photons} = \sqrt{2} \cdot FWHM_{1photon}. \quad (83)$$

The specifications of the laser can be validated by trying to overlay the computed spectrum at known temperature and pressure with known laser-linewidth. The result of this is shown in Figure 34.

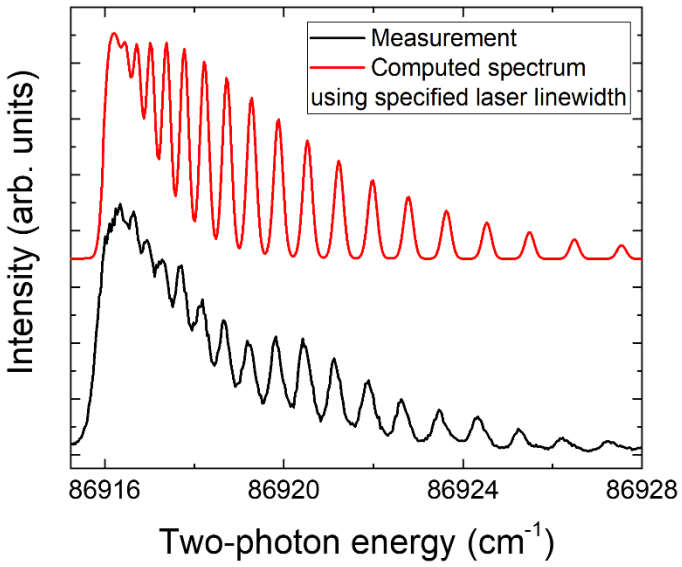

Figure 34 Computed spectrum using the laser-linewidth given by the specifications, together with a measurement. Temperature and pressure are known, and are therefore used in the computation of the excitation spectrum.

Clearly this is not a good fit, and the actual linewidth is much larger. The computed fringes of the peaks are much deeper than what is actually measured. The laser-linewidth is therefore chosen as a separate fitting parameter to be included in further measurements. The downside of making the linewidth a fitting parameter is that it becomes partly interchangeable with the main fitting parameter, temperature. Temperature also has an effect on the line broadening, however it has a much stronger effect on the fractional population in the ground state. This makes the interchangeability of these two parameters minimal, allowing for simultaneous fitting of the two parameters.

5.3 Linearity

Operation in the linear regime of TALIF is required for these measurements. In the linear regime it is assumed that the ground state is not depleted, and that the power is low enough to make the diagnostic technique non-intrusive. To check in which regime the system operates, the laser power should be varied. If the signal intensity scales linearly with the energy per pulse squared the system operates in the linear regime. Experimentally the input power is varied with the Rochon-prism, and the signal intensity is measured at a fixed laser-wavelength. The result of this experiment is shown in Figure 35.

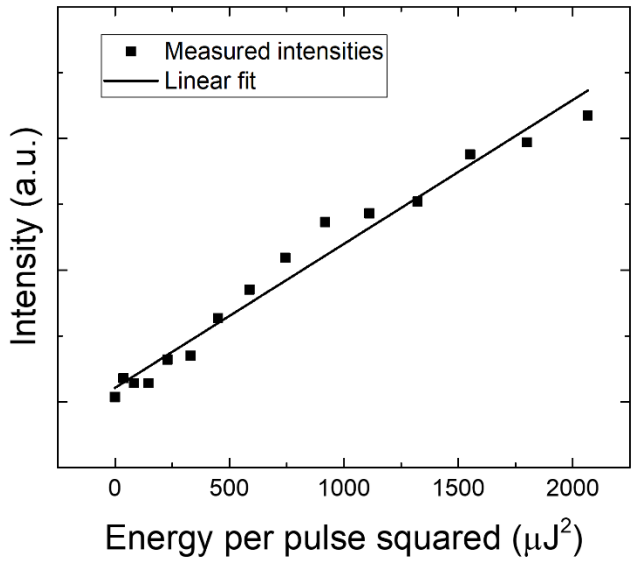

Figure 35 Validation of operation in the linear regime, by measuring the intensity as a function of the energy per pulse. In the linear regime the intensity scales linear with the square of energy per pulse, confirmed through this measurement.

This shows that the TALIF signal scales linearly with the square of input power, concluding that operation in the linear regime is achieved when the energy is in the range between 0 and 50μJ per pulse. This validates the inherent assumption of the simulations, which is that the ground state is far from depletion. The non-intrusiveness of the diagnostic is also reinforced, since operation in the linear regime minimizes the chances of inducing photochemistry.

5.4 Bandpass filter

It would be beneficial for the signal to noise ratio of the experiments if most of the ambient light could be filtered out before this light emits on the detector. It would even be more beneficial to filter out pulsed light sources, such as scattered light from the windows, or fundamental light of the dye-or YAG-lasers. These light sources can have a big impact on the measurements. Ambient light increases the baseline in the temporal measurements, and is easily filtered out numerically. Pulsed light cannot easily be distinguished from the fluorescence signal in temporal measurements, and will therefore increase the baseline of the excitation spectrum. This is more challenging to filter out, especially if this light is not constant over time. To investigate what type of filter has to be used the fluorescence is measured using a spectrometer using a grating of 2400 lines/mm, while only looking at one fluorescence band. The band around 520nm is chosen for this, since it has one of the highest Franck-Condon factors, and it does not have any light contamination from the dye-laser fundamental. An added advantage of using a spectrometer to do several measurements is that the applicability of Kasha's rule can be validated.

The fluorescence spectrum of the vibrational band near 520nm is shown in Figure 36a for multiple laser wavelengths. Figure 36b shows a computed excitation spectrum with arrows indicating the laser wavelengths for which the fluorescence in Figure 36a is shown. These four laser wavelengths cover a wide range of the excitation spectrum.

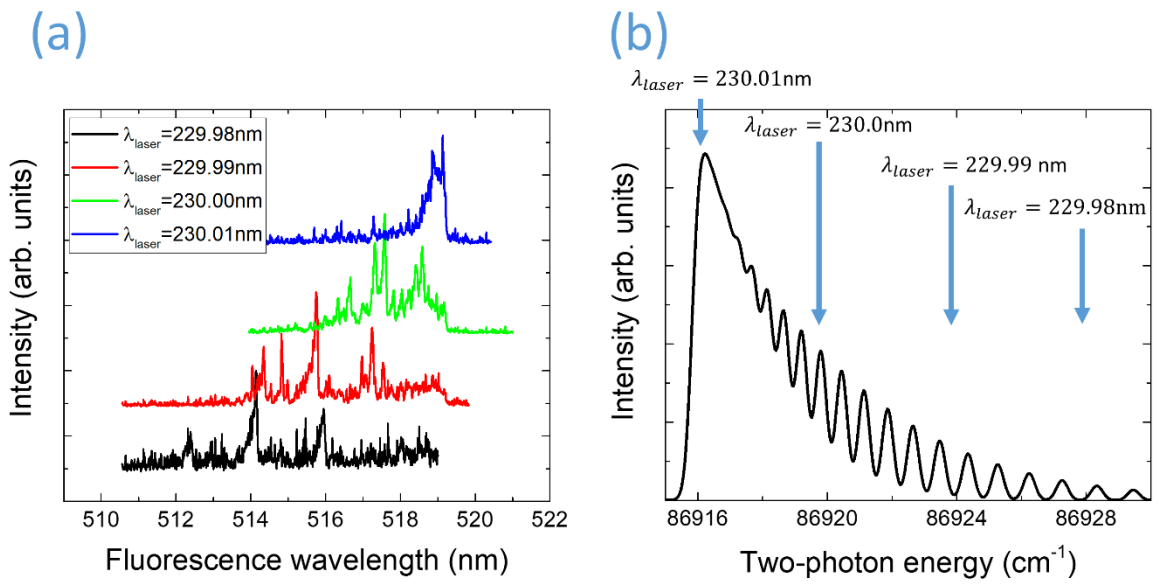

Figure 36 (a) shows the spectral measurements of TALIF of CO for four different laser wavelengths. Measurements taken at 20mbar and room temperature. The height of the peaks of the different measurements is normalized to one. (b) shows the laser wavelengths in an excitation spectrum at which the fluorescence spectra of (a) are taken.

These measurements show a large variation in output wavelength, and shape of the fluorescence, thereby already confirming that Kasha's rule is not valid for CO under these pressures. The different shapes and the large shift in fluorescence wavelength of these measurements can be validated by comparing these measurements to the simulation of the fluorescence spectrum created in section 3.3. The absolute values of the laser wavelength and the laser-linewidth are not known. A third unknown in this simulation is the broadening of the spectrometer, which should be taken into account when comparing these spectra to a simulation. However an attempt can be made to simulate something resembling these measurements.

The highest wavelength of Figure 36 is in the heavily convoluted region of the excitation spectrum, hence the broad feature instead of individually distinguishable peaks. A wavelength in this region can be chosen in order to compute the fluorescence spectrum. The other wavelengths are computed by taking this wavelength and subtracting 0.01nm from the laser wavelength for each consecutive spectrum. For the instrumental broadening $5\mathrm{cm}^{-1}$ is chosen, and a laser linewidth of $0.3\mathrm{cm}^{-1}$ is used. The results of these simulations are displayed in Figure 37.

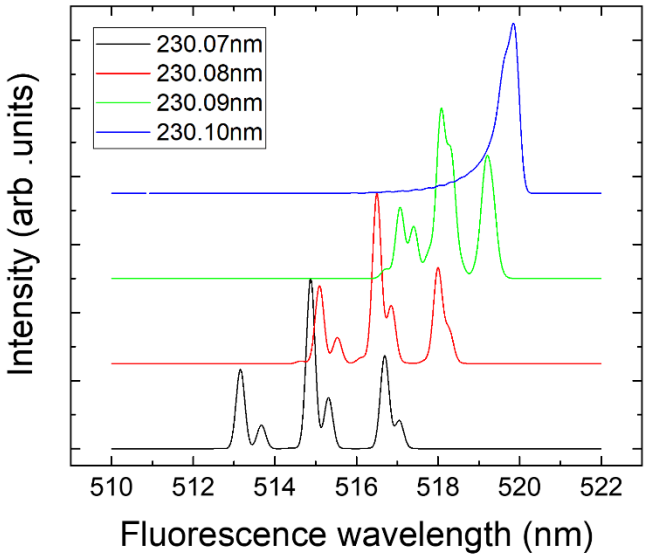

Figure 37 Calculated fluorescence for different input wavelength for a pressure of 20mbar and room temperature. Assuming an instrumental broadening of 5cm^{-1}. The height of the peaks of the different spectra are all normalized to one.

This figure confirms the large variation in shape and fluorescence wavelength which was measured. There is no complete overlap between measurement and computation, which is explained by the unknowns of the laser wavelength and linewidth. The shapes of the different spectra can qualitatively be explained. At the highest wavelength the laser matches with many different transitions in the Q-branch, since many transition lines are placed closely together in this region. This gives a broad fluorescence spectrum consisting of a lot of transitions. The individual transitions can no longer be distinguished. When the wavelength is lowered less lines get excited, since the separation of lines for higher J increases. More structures can be observed. Different lines get excited proportional to the laser overlap. For each of these lines there are three different fluorescence branches, which can be identified in both the measured and the calculated spectra.

It is possible to place a bandpass filter before the PMT, however as these measurements confirm this bandpass filter needs to have a flat transmittance for a fairly large spectral range. Measurements with and without a bandpass filter around 520nm (FWHM 10nm) were taken. In Figure 38 the spectrum measured with a bandpass filter is shown, together with a fit of only the laser linewidth, since both temperature and pressure are known. This illustrates that using a bandpass filter which does not have a flat transmittance has a significant impact on the excitation spectrum, and no reliable fit can be obtained. The signal gets cut off on the left side of the spectrum, which makes the fit underestimate the signal intensity in this region. This then leads to a bad fit everywhere, including the right side of the spectrum.

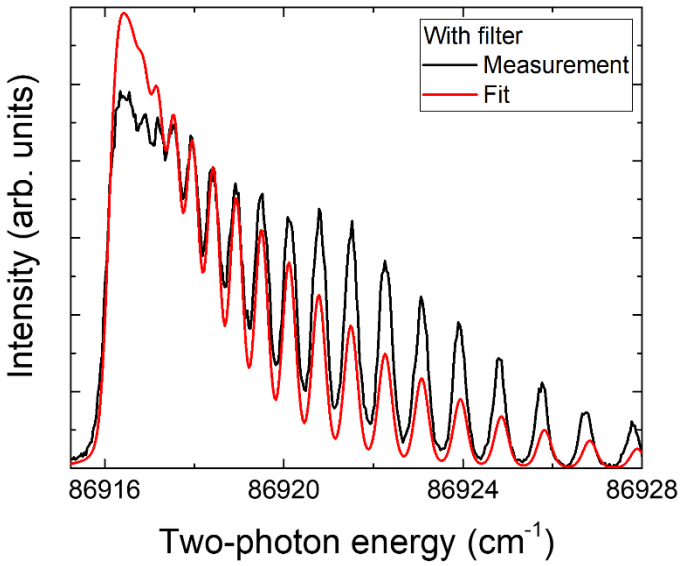

Figure 38 Measurement of the excitation spectrum taken with a bandpass filter, having a central wavelength of 520nm and FWHM of 10nm, together with a fit to compute the laser line-width, since temperature and pressure are fixed.

This measurement shows that this particular bandpass filter is not suited for measuring. The shape of the excitation spectrum changes significantly, therefore all further measurements are taken without any bandpass filter.

5.5 Fitting of an excitation spectrum

Now that the above mentioned prerequisites are handled a final excitation spectrum can be fitted, to obtain a temperature.

Figure 39 shows a measured excitation spectrum with a fit. The pressure is a fixed parameter, whereas the laser-linewidth and the temperature are free parameters. The fit converges, and gives a reasonable temperature, however it can be seen that the fitting process is still not perfect. That there are still regions in the convoluted part and the almost resolved part of the spectrum that do not overlap. There can be a whole range of causes for parts of the spectrum to not overlap completely, these can be sought in the computations, or in the experiments.

To check whether the computations are valid, the fitting program is used on data from literature. The data chosen is the data displayed already in Figure 25, where qualitatively the excitation spectrum computed in this work is compared to the measurements and model of Di Rosa and Farrow [91]. This data is digitized, and subsequently fitted using the developed function in this work. Temperature, pressure and laser-wavelength are free fitting parameters, which should all give similar values to the actual values reported for this measurement.

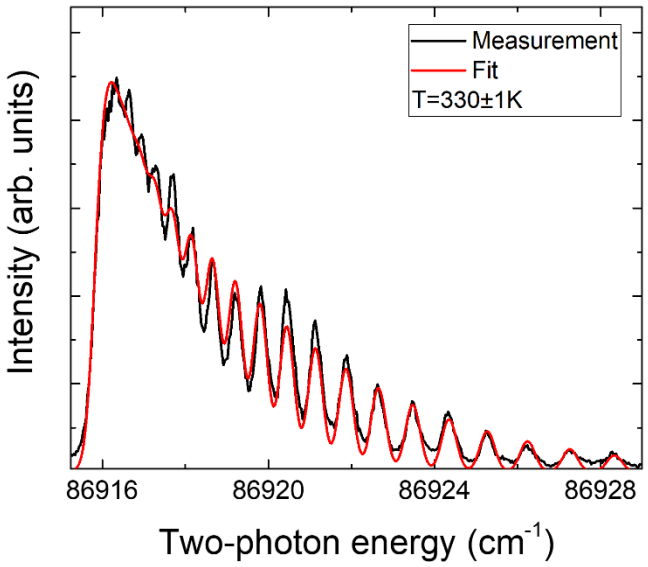

Figure 39 TALIF measurement taken at room temperature with a pressure of 10mbar, together with a fit to obtain the temperature, giving 330K.

In Figure 40 this fit is shown. The fit converges almost perfectly with the digitized data. The given pressure is almost the same as the one reported, whereas the fitted temperature is slightly too low. Overall this shows that the simulation is correct, since no significant deviations are observed. Clearly the wavelength axis is calibrated slightly differently, since the numerical band-aid discussed in section 5.1 is not applied for this fit in order to keep this data fitting procedure as clean as possible. In the convoluted part of the spectrum, near the first rotational lines, a deviation occurs, but this is most probably caused by the process used to digitize this data. The parameter that did not fit decently is the laser width. The laser used in the work of Di Rosa has such a small linewidth that it is almost negligible compared to the Doppler and collisional broadening effects, which therefore gives a large fitting error. The successful fitting of data from literature excludes the simulation as a cause for the discrepancy between simulation and the measurement in this work. There are a plethora of experimental reasons why this deviation might occur.

One possible cause for this deviations is absorption of laser light before the focus. This is checked by placing a power meter placed behind the reactor. If absorption before the focal point would be a significant problem the power meter would show a change in transmitted power over the wavelength scan. It does however not show any significant change in intensity over the whole scan. It has to be said though, the accuracy of the power-meter is not sufficient to rule this out completely. Since TALIF depends very strongly on the laser intensity, a small change in laser output power would already have such an effect, whereas this small change in power is hardly measurable with this tool. This could be more accurately monitored using a UV-sensitive photodiode. This photodiode would also check the stability of the laser with a shot-to-shot accuracy. It is possible to account for this absorption numerically if the laser beam has a Gaussian profile. In the current setup it does not have such a profile, however the laser can be forced into a Gaussian by focusing it through a pinhole.

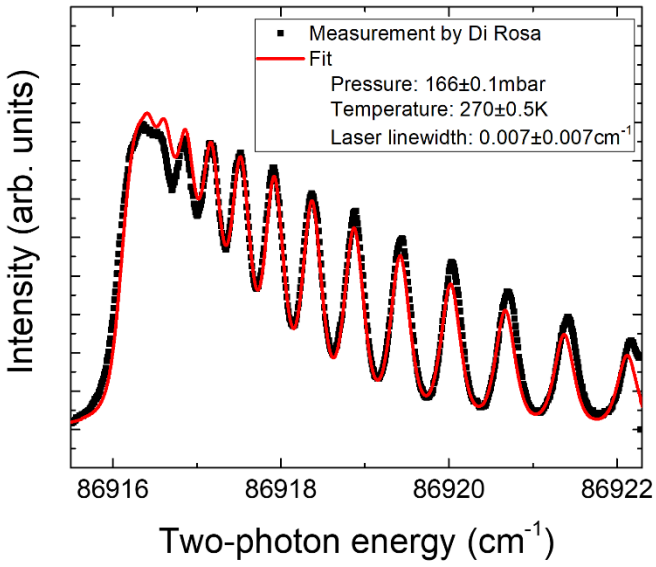

Figure 40 A fit done to the data published by Di Rosa and Farrow [91]*. The conditions in which this measurement was taken are 170mbar pressure, room temperature. A laser with a width of* $0.004cm^{-1}$ *is used.*

Currently it is assumed that quenching is independent on the rotational quantum number. If J-dependent quenching would be significant the shape of the spectrum would change according to this dependence. However this has not been reported in literature [96], making this an unlikely factor to cause deviations in the excitation spectrum. A change in the laser linewidth over the scanning range also is an unlikely cause for these deviations, since this linewidth is determined completely by the grating of the dye-laser. This angle of the grating only changes by a very small amount over the scanning range, which makes it improbable that the linewidth would change.

A last possible reason for the deviations from the computed spectrum might be C_2 crosstalk. The excitation spectrum of C_2 is not accounted for in this work, whereas it might very well have a significant impact on the measurements. This crosstalk can be checked in future work by measuring all the vibrational bands for different excitation wavelengths. The height of the vibrational features can then be compared to the Franck-Condon factors, which determine the ratios between the vibrational bands in the Angstrom system. If there is a change in these ratios for different excitation wavelengths, and if the ratios between the areas of these peaks do not match the Franck-Condon factors, C_2 crosstalk is possibly a problem.

In the end however, the developed code to calculate and fit measured absorption spectra can be applied to measurements taken to give temperatures with reasonable accuracy.

6. Conclusion & Outlook

This work serves as a proof-of-concept of measuring temperatures using TALIF on CO. The conclusions and outlook concern the diagnostic itself, together with possible improvements that can be applied to either the TALIF setup or the data analysis as well as possible future measurements.

6.1 Conclusion

This work focuses on the data acquisition and analysis of TALIF on CO. A working setup was constructed, which can measure the excitation spectrum of the Q-branch of excitations to the $B\,^1\Sigma^+$ state of CO. The setup consists of a frequency tripled Nd:YAG laser coupled into a frequency doubled dye laser. This generates the required tunable laser beam of 230nm, which can be tuned to specific wavelengths of the excitation spectrum. A new software was applied to change the grating position in the laser stepwise, while simultaneously saving fluorescence data measured with a photomultiplier tube. Such a wavelength scan then measures the excitation spectrum. The setup is furthermore constructed in such a way that *in-situ* spatially resolved measurements in a microwave discharge can be made.

A simulation of this particular TALIF excitation scheme was created, which can compute both the excitation spectrum and the fluorescence spectrum. The excitation spectrum depends strongly on the temperature, which makes this spectrum suited for iterative data fitting to obtain the temperature from a measured excitation spectrum. The fluorescence spectrum computes the fluorescence emitted by excited CO molecules for a certain excitation wavelength. This is qualitatively compared to spectrally resolved measurements to investigate the applicability of a bandpass filter.

The procedure of measuring an excitation spectrum and subsequent fitting of this spectrum is applied successfully in this work. An excitation spectrum is measured at room temperature and subsequently fitted to obtain this room temperature, 330K was found instead of 295K. To further reinforce the applicability of the data analysis procedure, experimental data from literature was fitted using the software. This data converged, and gave a pressure and temperature very close to the reported values. A temperature of 270K was found for room temperature and a pressure of 166mbar was found for 170mbar. This shows the applicability of this method for finding temperatures based on the excitation spectrum of CO.

6.2 Outlook

There are many options to continue this research, including future measurements as well as improvements to the experimental setup.

6.2.1 Future measurements

- Research into TALIF on CO in gas discharges will need to improve the fitting process of the excitation spectrum. Crosstalk of C_2 is one factor that needs to be investigated. C_2 crosstalk can be investigated by comparing the Franck-Condon factors of spectrally resolved measurements.
- In this work only temperatures are measured using TALIF, however, for TALIF to have any advantage over more conventional laser diagnostics, such as Raman scattering, densities should be measured. A proposed way to measure densities with this setup would be to extend the numerical analysis of the data. The shot-to-shot behavior of the laser pulse can be measured

using a photodiode. This data can then be compared with the data of the photomultiplier tube, and the theory of TALIF can used to try to obtain an effective lifetime for each measurement. The Stern-Volmer method can then be applied to account for the quenching. If quenching is known relative densities can be measured.

- The constructed setup can be used to measure spatially resolved temperatures in a microwave discharge, where the created software and fitting procedures can be applied.

6.2.2 Experimental setup

- TALIF very strongly depends on the laser stability, therefore one of the greatest improvements possible to this setup would be a method to automatically measure and adjust the laser power in order to improve the stability of the setup.
- Absorption before the focal point can affect measurements, which can in principle be taken into account. However the only assumption that has to be made when accounting for this is a Gaussian laser profile. The laser can be forced into a Gaussian shape by focusing it through a pinhole.
- Another big improvement to the stability and noise-level of the measurements would be the addition of a suitable bandpass filter. Currently any light is amplified by the photomultiplier tube, not only light coming from the fluorescence. Changes in both ambient and pulsed light picked up by the photomultiplier tube changes the background, decreasing the accuracy of the data analysis.
- One last potentially very interesting topic would be to measure Doppler free. The setup in principle allows for this. Much more rotational lines become resolvable, potentially giving a much more accurate temperature fit.

References

[1] Intergovernmental Panel on Climate Change, *Climate Change 2014 - Impacts Adaptation and Vulnerability*. Cambridge University Press, 2014.

[2] C. Rosenzweig, A. Iglesias, X. B. Yang, P. R. Epstein, and E. Chivian, "Climate change and extreme weather events," *Glob. Chang. Hum. Heal.*, vol. 2, no. 2, pp. 90–104, 2001.

[3] T. R. Knutson, J. L. McBride, J. Chan, K. Emanuel, G. Holland, C. Landsea, I. Held, J. P. Kossin, A. K. Srivastava, and M. Sugi, "Tropical cyclones and climate change," *Nat. Geosci.*, vol. 3, pp. 157–163, 2010.

[4] J. X. Mitrovica, M. E. Tamisiea, J. L. Davis, and G. A. Milne, "Recent mass balance of polar ice sheets inferred from patterns of global sea-level change," *Nature*, vol. 409, no. February, pp. 1026–1029, 2001.

[5] IPCC, *Climate Change 2014 - Impacts, Adaptation and Vulnerability: Regional Aspects*. Cambridge University Press, 2014.

[6] C. F. Baes, "Carbon Dioxide and Climate : The Uncontrolled Experiment," 2016.

[7] R. C. Duncan, "World Energy Production , Population Growth , and the Road to the Olduvai Gorge," *Popul. Environ.*, vol. 22, no. 5, pp. 503–522, 2001.

[8] P. Friedlingstein, R. M. Andrew, J. Rogelj, G. P. Peters, J. G. Canadell, R. Knutti, G. Luderer, M. R. Raupach, M. Schaeffer, D. P. Van Vuuren, and C. Le Quéré, "Persistent growth of CO2 emissions and implications for reaching climate targets," *Nat. Publ. Gr.*, vol. 7, no. 10, pp. 709–715, 2014.

[9] G. Yamamoto, "Direct Absorption of Solar Radiation by Atmospheric Water Vapor, Carbon Dioxide and Molecular Oxygen," *J. Atmos. Sci.*, vol. 19, pp. 182–188, 1961.

[10] L. H. Ziska and F. A. Caulfield, "Rising CO2 and pollen production of common ragweed, a known allergy-inducing species: implications for public health.," *Funct. Plant Biol.*, vol. 27, no. 10, pp. 893–898, Oct. 2000.

[11] P. M. Vitousek, H. A. Mooney, J. Lubchenco, and J. M. Melillo, "Human Domination of Earth ' s Ecosystems," *Science (80-.).*, vol. 277, pp. 494–499, 1997.

[12] T. J. Crowley, "Causes of Climate Change Over the Past 1000 Years," *Science (80-.).*, vol. 289, pp. 270–278, 2000.

[13] A. M. Mccright, R. E. Dunlap, and S. T. Marquart-Pyatt, "Political ideology and views about climate change in the European Union," *Env. Polit.*, vol. 25, no. 2, pp. 338–358, 2017.

[14] United Nations Climate Change Secretariat, "Work programme resulting from the relevant requests contained in decision 1 / CP . 21." 2017.

[15] R. S. Dimitrov, "Forums The Paris Agreement on Climate Change : Behind Closed Doors," *Glob. Environ. Polit.*, vol. 16, pp. 1–11, 2016.

[16] Y. Shimomura and R. Aymar, "Overview of ITER-FEAT - The future international burning plasma

experiment," *Nucl. Fusion*, vol. 41, no. 10, pp. 1301–1310, 2001.

[17] M. Krychowiak, "Wendelstein 7-X : Overview of diagnostic performance and results for the first operation phase in Wendelstein 7-X," *Rev. Sci. Instrum.*, vol. 729, no. June, 2016.

[18] J. Ongena and Y. Ogawa, "Nuclear fusion : Status report and future prospects," *Energy Policy*, vol. 96, pp. 770–778, 2016.

[19] F. Romanelli, L. H. Federici, R. Neu, D. Stork, and H. Zohm, "A roadmap to the realization of fusion energy," *Proc. IEEE 25th Symp. Fusion Eng*, pp. 1–4, 2013.

[20] M. Dittmar, "Nuclear energy: Status and future limitations," *Energy*, vol. 37, no. 1, pp. 35–40, 2012.

[21] World Nuclear Association, "Nuclear Power in the World Today," 2017. [Online]. Available: http://www.world-nuclear.org/information-library/current-and-future-generation/nuclear-power-in-the-world-today.aspx. [Accessed: 29-Sep-2017].

[22] A. Yablokov, V. Nesterenko, and A. Nesterenko, "Chernobyl; Consequences of the Catastrophe for People and the Environment," *Ann. N. Y. Acad. Sci.*, vol. 1181, p. 5, 2009.

[23] K. Boomer, "Nuclear Waste," *Engineering*, no. 11212. pp. 1–15, 2011.

[24] OECD/IAEA, *Uranium 2014*. OECD Publishing, 2014.

[25] United Nations Development Programme, *World Energy Assessment. Energy and the challenge of Sustainability*. 2000.

[26] R. Perez and M. Perez, "A Fundamental Look At Supply Side Energy Reserves For The Planet," *Int. Energy Agency SHC Program. Sol. Updat.*, no. April 2009, pp. 4–6, 2015.

[27] D. R. Gergel, B. Nijssen, J. T. Abatzoglou, D. P. Lettenmaier, and M. R. Stumbaugh, "Effects of climate change on snowpack and fire potential in the western USA," *Clim. Chang.*, vol. 141, pp. 287–299, 2017.

[28] K. Thirumalai, P. N. Dinezio, Y. Okumura, C. Deser, and E. Nin, "Extreme temperatures in Southeast Asia caused ˜ o and worsened by global warming by El Nino and worsened by global warming," *Nat. Commun.*, vol. 8, pp. 1–8, 2017.

[29] Bundesministerium für Wirtschaft und Energie, "Zeitreihen zur Entwicklung der erneuerbaren Energien in Deutschland," 2016.

[30] F. Tao, Z. Feng, H. Tang, Y. Chen, and K. Kobayashi, "Effects of climate change , CO2 and O3 on wheat productivity in Eastern China , singly and in combination," *Atmos. Environ.*, vol. 153, pp. 182–193, 2017.

[31] J. A. Mathews and H. Tan, "China's Energy Firms: New Dragon Multinationals," in *China's Renewable Energy Revolution*, London: Palgrave Macmillan UK, 2015, pp. 107–126.

[32] International Energy Agency, "Key World Energy Statistics," 2017.

[33] B. K. Sovacool, "The intermittency of wind , solar , and renewable electricity generators : Technical barrier or rhetorical excuse ?," *Util. Policy*, vol. 17, pp. 288–296, 2009.

[34] D. Elliott, "A balancing act for renewables," *Nat. Energy*, vol. 1, no. January, pp. 1–3, 2016.

[35] A. J. Carvallo, “Energy Storage Technologies for Utility Scale Intermittent Renewable Energy Systems,” *J. Sol. Energy Eng.*, vol. 123, pp. 387–389, 2001.

[36] M. C. McManus, “Environmental consequences of the use of batteries in low carbon systems: The impact of battery production,” *Appl. Energy*, vol. 93, pp. 288–295, 2012.

[37] B. R. Cooper and W. A. Ellingson, *The Science and Technology of Coal and Coal Utilization*. New York: Plenum Press, 1984.

[38] G. Jeong, H. Kim, J. H. Park, J. Jeon, X. Jin, J. Song, B. Kim, M.-S. Park, J. M. Kim, and Y.-J. Kim, “Nanotechnology enabled rechargeable Li-SO2 battery: Another approach towards post lithium-ion battery system,” *Energy Environ. Sci.*, vol. 8, pp. 3173–3180, 2015.

[39] C. K. Dyer, “Fuel cells for portable applications,” *J. Power Sources*, vol. 106, pp. 31–34, 2002.

[40] H. Schulz, “Short history and present trends of Fischer – Tropsch synthesis,” *Appl. Catal.*, vol. 186, pp. 3–12, 1999.

[41] J. R. Bolton, “Solar Fuels,” *Science (80-.).*, vol. 202, no. 4369, pp. 705–711, 1978.

[42] V. Eletskii and B. M. Smirnov, “Dissociation of molecules in plasma and gas: the energy,” *Pure Appl. Chem.*, vol. 57, no. 9, pp. 1235–1244, 1985.

[43] L. B. Ibragimova, G. D. Smekhov, O. P. Shatalov, A. V Eremin, and V. V Shumova, “Dissociation of CO2 Molecules in a Wide Temperature Range,” *Thermophys. Prop. Mater.*, vol. 38, no. 1, pp. 37–40, 2000.

[44] M. A. Lieberman and A. J. Lichtenberg, *Principles of Plasma Discharges and Material Processing*, 2nd ed., vol. 1. Hoboken, New Jersey: Wiley, 2005.

[45] L. F. Spencer and A. D. Gallimore, “Efficiency of CO2 Dissociation in a Radio-Frequency Discharge,” *Plasma Chem. Plasma Process.*, vol. 31, no. 1, pp. 79–89, 2011.

[46] A. Fridman, *Plasma Chemistry*, 1st ed. Cambridge University Press, 2008.

[47] R. Snoeckx and A. Boogaerts, “Plasma technology – a novel solution for CO2 conversion?,” *Chem. Soc. Rev.*, vol. 46, pp. 5805–5863, 2017.

[48] G. J. van Rooij, D. C. M. van den Bekerom, N. den Harder, T. Minea, G. Berden, W. A. Bongers, R. Engeln, M. F. Graswinckel, E. Zoethout, and M. C. M. van de Sanden, “Taming microwave plasma to beat thermodynamics in CO2 dissociation,” *Faraday Discuss.*, vol. 183, no. 0, pp. 233–248, 2015.

[49] S.-L. Park, J.-D. Moon, S.-H. Lee, and S.-Y. Shin, “Effective ozone generation utilizing a meshed-plate electrode in a dielectric-barrier discharge type ozone generator,” *J. Electrostat.*, vol. 64, no. 5, pp. 275–282, 2006.

[50] T. Nunnally, “Dissociation of CO 2 in a low current gliding arc plasmatron,” 2011.

[51] V. D. Rusanov, A. A. Fridman, and G. V Sholin, “The physics of a chemically active plasma with nonequilibrium vibrational excitation of molecules,” *Sov. Phys. Uspekhi*, vol. 24, pp. 449–472, 1981.

[52] M. Damen, “A spectroscopic study on the detection of carbon monoxide for solar fuel production,” Eindhoven University of Technology, 2015.

[53] J. L. Kinsey, “Laser-Induced Fluorescence,” *Annu. Rev. Phys. Chem.*, vol. 28, no. 1, pp. 349–372, 1977.

[54] P. H. Krupenie, “The band spectrum of carbon monoxide,” 1966.

[55] J. M. Hollas, *Modern Spectrospy*, 4th ed. Wiley, 2004.

[56] W. Demtroder, *Atoms, Molecules and Photons*, 2nd ed. Springer, 2010.

[57] D. J. Griffiths, *Introduction to Quantum Mechanics*, Second. Pearson Eduction, 2005.

[58] P. M. Morse, “Diatomic Molecules According to the Wave Mechanics II Vibrational Levels,” *Phys. Rev.*, vol. 34, no. 1, 1929.

[59] R. J. Leroy and R. B. Bernstein, “Dissociation Energy and Long-Range Potential of Diatomic Molecules from Vibrational Spacings of Higher Levels,” *J. Chem. Phys.*, vol. 52, no. 8, pp. 3869–3879, 1970.

[60] J. L. Dunham, “The Energy Levels of a Rotating Vibration,” *Phys. Rev.*, vol. 41, no. 1932, pp. 722–731, 1932.

[61] J. Brown and A. Carrington, *Rotational Spectroscopy of Diatomic Molecules*, 1st ed. Cambridge University Press, 2003.

[62] J. Hodgkinson and R. P. Tatam, “Optical gas sensing : a review,” *Meas. Sci. Technol.*, vol. 24, 2013.

[63] E. Condon, “Theory of intensity distribution in band systems,” *Phys. Rev.*, vol. 28, pp. 1182–1201, 1926.

[64] M. Sauer, J. Hofkens, and J. Enderlein, “Basic Principles of Fluorescence Spectroscopy,” in *Handbook of Fluorescence Spectroscopye and Imaging*, 2010, pp. 12–15.

[65] D. R. Bates, “Relative Transition Probabilities in band systems of diatomic molecules,” *R. Astron. Soc.*, vol. 112, no. 6, pp. 614–637, 1952.

[66] H. Lefebvre-Brion and R. W. Field, *The Spectra and Dynamics of Diatomic Molecules*, 2nd ed. Elsevier Ltd.

[67] Y. H. Honl and F. London, “Uber die Intensitaten der Bandenlinien.,” *Zeitschrift fur Phsysik*, vol. 33, no. 54, pp. 803–809, 1925.

[68] Gerhard Herzberg, *Atomic Spectra and Atomic Structure*, 1st ed. New York: Dover Publications, 1944.

[69] I. Kovacs, *Rotational structure in the spectra of diatomic molecules*, 1st ed. Budapest: Akademiai Kiado Budapest and Adam HIgler LTD, London, 1969.

[70] R. C. Hilborn, “Einstein coefficients, cross sections,” pp. 1–12, 2002.

[71] P. H. Paul, J. A. Ray, J. L. Urant, and J. W. Homan, “Collisional quenching corrections for laser-induced fluorescence measurements of NO A2Sigma(+),” *AIAA J.*, vol. 32, no. 8, pp. 1670–1675, Aug. 1994.

[72] Y. Deguchi, “Industrial Applications of Laser Diagnostics,” CRC Press, 2012, pp. 72–74.

[73] P. Vankan, “Molecules and Atoms in a Hydrogen Plasma Expansion,” Technische Universiteit

Eindhoven, 2005.

[74] D. B. Santolo and D. Giorgio, “Laser-Induced Fluorescence Methods for Transient Species Detection in High- Pressure Discharges,” *Low Temp. Plasma Technol. Methods Appl.*, vol. 2, 2013.

[75] R. G. Bray and R. M. Hochstrasser, “Two-photon absorption by rotating diatomic molecules,” *Mol. Phys.*, vol. 31, no. 4, pp. 1199–1211, 1976.

[76] W. Demtroder, *Laser Spectroscopy Vol. 2: Experimental Techniques*, 4th ed. Springer, 1981.

[77] R. Loudon, *The Quantum Theory of Light*, 3rd ed. Oxford University Press, 2000.

[78] K. Niemi, V. S. der Gathen, and H. F. Dobele, “Absolute calibration of atomic density measurements by laser-induced fluorescence spectroscopy with two-photon excitation,” *J. Phys. D. Appl. Phys.*, vol. 34, pp. 2330–2335, 2001.

[79] M. Göppert-Mayer, “Über Elementarakte mit zwei Quantensprüngen,” *Ann. Phys.*, vol. 401, no. 3, pp. 273–294, 1931.

[80] M. Hippler, “Interference in two-photon rotational line strengths of diatomic molecules,” *Mol. Phys.*, vol. 97, no. 1–2, pp. 105–115, 1999.

[81] P. A. Freedman, “The two photon absorption spectrum of NO,” *Can. J. Phys.*, vol. 55, no. 16, pp. 1387–1392, 1977.

[82] K. Chen and E. S. Yeung, “Rovibronic two-photon transitions of symmetric top molecules,” *J. Chem. Phys.*, vol. 69, no. 1, pp. 43–51, 1978.

[83] J. W. Gibbs, *Elementary Principles in Statistical Mechanics*. New York: Dover Publications, 1902.

[84] M. Kasha, “Characterization of Electronic Transitions in Complex Molecules,” *Complex Mol.*, vol. 9, 1950.

[85] K. Yanagi and H. Kataura, “Breaking Kasha’s rule,” *Nat. Photonics*, vol. 4, pp. 200–201, 2010.

[86] S. Linow, A. Dreizler, J. Janicka, and E. P. Hassel, “Comparison of two-photon excitation schemes for CO detection in flames,” *Appl. Phys. B Lasers Opt.*, vol. 71, pp. 689–696, 2000.

[87] G. W. Loge, J. J. Tiee, and F. B. Wampler, “Multiphoton induced fluorescence and ionization of carbon,” *J. Chem. Phys.*, vol. 79, no. 1, pp. 196–202, 1983.

[88] P. Erman, A. Karawajczyk, E. Rachlew-k, and C. Stromholm, “Direct determination of the ionization potential of CO by resonantly enhanced multiphoton ionization mass spectroscopy,” *Chem. Phys. Lett.*, vol. 215, no. 1, pp. 173–178, 1993.

[89] R. T. Jongma, M. G. H. Boogaarts, and G. Meijer, “Double-Resonance Spectroscopy on Triplet States of CO,” *J. Mol. Spectrosc.*, vol. 165, pp. 303–314, 1994.

[90] W. F. Chan, G. Cooper, and C. E. Brion, “Absolute optical oscillator strengths for discrete and continuum photoabsorption of carbon monoxide (7-200 eV) and transition moments for the X->A system,” *Chem. Phys.*, vol. 170, pp. 123–138, 1993.

[91] M. D. Di Rosa and R. L. Farrow, “Two-photon excitation cross section of the B<-X(0,0) band of CO measured by direct absorption,” *J. Opt. Soc*, vol. 16, no. 11, pp. 1988–1994, 1999.

[92] W. R. Ferrell, C. H. Chen, M. G. Payne, and R. D. Willis, “Two-resonance step ionization spectroscopy of CO,” *Chem. Phys. Lett.*, vol. 97, no. 4.5, pp. 460–466, 1983.

[93] W. Groth, “Chemical Spectroscopy and Photochemistry in the Vacuum-Ultraviolet,” in *The Early Years of Photochemistry in the VUV*, 1973, pp. 415–426.

[94] M. Drabbels, S. Stolte, and G. Meijer, “Production of an intense pulsed beam of oriented metastable CO a 311,” *Chem. Phys. Lett.*, vol. 200, no. 1, pp. 108–112, 1992.

[95] M. Richter, M. Alde, J. Rosell, and J. Sjo, “Comparison of Three Schemes of Two-Photon Laser-Induced Fluorescence for CO Detection in Flames,” *Appl. Spectrosc.*, vol. 67, no. 3, pp. 314–320, 2013.

[96] F. Di Teodoro, J. E. Rehm, R. L. Farrow, P. H. Paul, F. Di Teodoro, J. E. Rehm, R. L. Farrow, and P. H. Paul, “Collisional quenching of CO B1Sigma+ (v’=0) probed by two-photon laser-induced fluorescence using a picosecond laser,” *J. Chem. Phys.*, vol. 113, no. 8, pp. 3046–3054, 2000.

[97] L. C. Lee and J. A. Guest, “Quantative absorption and fluorescence study of CO from 1060 to 1150 A.” NASA, Menlo Park, 1980.

[98] T. B. Settersten, A. Dreizler, and R. L. Farrow, “Temperature-and Species Dependent Quenching of CO B Probed by Two-Photon Laser Induced Fluorescence Using a Picosend Laser,” *J. Chem. Phys.*, vol. 117, no. 7, pp. 3173–3179, 2002.

[99] M. D. Di Rosa and R. L. Farrow, “Cross sections of photoionization and ac Stark shift measured from Doppler-free B — X (0 , 0) excitation spectra of CO,” *J. Opt. Soc. Am. B*, vol. 16, no. 5, pp. 861–870, 1999.

[100] F. Fuest, R. S. Barlow, J. Chen, and A. Dreizler, “Raman / Rayleigh scattering and CO-LIF measurements in laminar and turbulent jet flames of dimethyl ether,” *Combust. Flame*, vol. 159, no. 8, pp. 2533–2562, 2012.

[101] A. Tanabashi, T. Hirao, and T. Amano, “The Swan System of C2: A Global Analysis of Fourier Transform Emission Spectra,” *Astrophys. J. Suppl. Ser.*, vol. 169, no. 2, pp. 472–484, 2007.

[102] H. S. Kwak, H. S. Uhm, Y. C. Hong, and E. H. Choi, “Disintegration of Carbon Dioxide Molecules in a Microwave Plasma Torch,” *Nat. Sci. Reports*, vol. 5, pp. 1–13, 2015.

[103] J. M. Seitzman, J. Haumann, and R. K. Hanson, “Quantitative two-photon LIF imaging of carbon monoxide in combustion gases,” *Appl. Opt.*, vol. 26, no. 14, pp. 2892–2899, 1987.

[104] K. Kirby and D. L. Cooper, “Theoretical study of low-lying Σ and Π states of CO . II . Transition dipole moments , oscillator strengths , and radiative lifetimes,” *J. Chem. Phys.*, vol. 90, no. 9, pp. 4895–4902, 1989.

[105] S. G. Simmons and D. Tilford, “Atlas of the Observed Absorption Spectrum of Carbon Monoxide Between 1060 and 1900 A,” *Am. Inst. Phys.*, vol. 147, no. 1, 1972.

[106] P. J. H. Tjossem and K. C. Smyth, “Multiphoton excitation spectroscopy of the B Σ and C Σ Rydberg states of CO,” *J. Chem. Phys.*, vol. 91, no. 4, pp. 2041–2048, 1989.

[107] M. D. Di Rosa and R. L. Farrow, “Temperature-dependent collisional broadening and shift of Q -branch transitions in the B Q X (0 , 0) band of CO perturbed by N , CO and CO,” *J. Quant. Spectrosc. Radiat. Transf.*, vol. 68, pp. 363–375, 2001.

[108] M. D. Levenson and N. Bloembergen, “Doppler-Free Two-Photon Absorption Spectroscopy,” *High-Resolution Laser Spectrosc.*, pp. 315–319, 1976.

[109] M. Gharavi and S. G. Buckley, “Single Diode Laser Sensor for Wide-Range H 2 O,” *Appl. Spectrosc.*, vol. 58, no. 4, pp. 468–473, 2004.

[110] R. W. Nicholls, P. A. Fraser, W. R. Jarmain, and R. P. McEachran, “Vibrational Transition Probabilities of Diatomic Molecules: Collected Results. IV. BeO, BO, CH+, CO, NO, SH, O2+,” *Astrophys. J.*, vol. 131, p. 399, 1960.

[111] F. Ortenberg, “Calculation of Franck-Condon factors for the NO, C2 and CO band systems,” *Opt. Spectrosc.*, vol. 16, no. 1, 1964.

[112] L. V. Leskov, “On the method of quantative gas analysys using electron-vibrational spectra of diatomic molecules,” *Opt. Spectrosc.*, vol. 62, no. 4, pp. 168–179, 1958.

[113] D. Robinson and R. W. Nicholls, “Intensity Measurements on the O2+ Second Negative, CO Ångström and Third Positive and NO γ and β Molecular Band Systems,” *Proc. Phys. Soc.*, vol. 71, no. 6, p. 957, 1958.

[114] N. S. Murthy and U. D. Prahllad, “Integrated Intensity Measurements and Relative Band Strengths of CO (Ansgstrom) Bands,” *Physica*, vol. 97, no. C, pp. 385–387, 1979.

[115] Sirah Lasertechnik, “Second Harmonic Generation.” 2013.

[116] J. N. Damask, “Polarization Optics in Telecommunications,” pp. 199–204.

[117] J. L. Gardner, “Compact Fizeau wavemeter,” *Appl. Opt.*, vol. 24, no. 21, pp. 3570–3573, Nov. 1985.

Appendix

The appendix is split in two parts, which both concern the data treatment. Appendix A shows the developed Matlab script to treat the data, whereas Appendix B shows the Matlab function *absorption_3* used in Appendix A, this computes the excitation spectrum, which depends on several of the input parameters.

Appendix A

Data analysis

```
clear all

dirinfo=dir('.dat');

intensity=zeros(size(dirinfo,1),3);

wave=importdata('1.dat');
y=wave.data(:,2);

laserwidth=0.1;

noise=y;
for i=1:999

    if exist([num2str(i-1) '.dat'],'file')>0
    wave=importdata([num2str(i-1) '.dat']);
    x=wave.data(:,1);
    y=wave.data(:,2);
    guess=[0,443,52.3,5];


    x_crap=x(x<1e-10);
    x_crap_siz=size(x_crap,1);
    y_size=size(y,1);
    x=x(x_crap_siz+1:y_size);
    y=y(x_crap_siz+1:y_size);
    x=x.*1e10;
    y=y.*100;
    lb=[-1,-10,0,0];
    ub=[10,100,100,100];

    intensity(i,2)=trapz(x,y);
    waveltn=inifile([num2str(i-1) '.dat.metadata'],'read',{'laser', '',
'fundamentalwavelength'});
    intensity(i,1)=(str2double(waveltn{1}));
    motorpos=inifile([num2str(i-1) '.dat.metadata'],'read',{'laser', '',
'oscillatormotorposition'});
    intensity(i,3)=(str2double(motorpos{1}));
    end
```

```
end
plot(intensity(:,1),intensity(:,2))
for i=2:999
    if intensity(i-1,1)==0
        intensity(i-1,1)=intensity(i,1);
        intensity(i-1,3)=intensity(i,3);
        intensity(i-1,2)=intensity(i,2);

    end
    if intensity(i-1,2)==0
        intensity(i-1,1)=intensity(i,1);
        intensity(i-1,2)=intensity(i,2);
        intensity(i-1,3)=intensity(i,3);
    end
end

intensity(:,2)=intensity(:,2)/max(intensity(:,2))+0.02;

intensity(:,1)=4*10^-2./intensity(:,1);
%resolution=abs(intensity(11,1)-intensity(10,1));
% dlambda=resolutionnm/intensity(10,1);
% nu=4/(100*intensity(10,1));
% resolution=dlambda*nu;

%abso_spectrum=abs_spectrum(290,0.005,resolution);


for i=1:size(intensity,1)-1
    if intensity(i,1)-intensity(i+1,1)==0
        intensity(i+1,2)=(intensity(i+1,2)+intensity(i,2))/2;
        intensity(i,1)=0;
        intensity(i,2)=0;
        intensity(i,3)=0;
    end
end

intensity(all(intensity==0,2),:) = [];

B_x=1.922521;
D_x=6.193*10^-6;

B_B=1.9475;
D_B=6.1*10^-6;

B0=B_B-B_x;
D0=D_B-D_x;


T0=290;
P0=.005;
```

```
calc_spec=fixax(B0,D0,laserwidth,intensity,T0,P0);



resolution=calc_spec(11,1)-calc_spec(10,1);

addpart1=0:resolution:100;

addpart1=addpart1'+calc_spec(1,1)-100;

addpart2=0:resolution:100;

addpart2=addpart2'+max(calc_spec(:,1));



newsize=size(addpart1,1)+size(addpart2,1)+size(calc_spec,1);



calc_new=zeros(newsize,3);
ditdat=size(addpart1,1)+1:newsize-size(addpart2,1);
ditdat=ditdat';
calc_new(1:size(addpart1,1),1)=addpart1;
calc_new(newsize+1-size(addpart2,1):newsize,1)=addpart2;
calc_new(ditdat,1)=calc_spec(:,1);
calc_new(ditdat,2)=calc_spec(:,2);
calc_spec=calc_new;
x=calc_spec(:,1);
y=calc_spec(:,2);


w0=86916.16;
laserwidth_0=0.3;
P0=0.04;

minpkheight=0.03;
i0=9991;
j0=999;
residual=9e9;

J=1:500;

J=J';

sticks=J.*(J+1)*B0+J.^2.*(J+1).^2*D0;
stickloc=round((sticks)/resolution)+1;
```

```
for i=4:20
    for j=1:20

[pks,pkslocs]=findpeaks(smooth(y),'MinPeakDistance',i,'MinPeakHeight',minpkheight);
        io=max(find(x<86916.16));
        pkslocs=pkslocs-io;
        pkslocs(pkslocs<0)=[];
        pkslocs2=zeros(500,1);
        siz=size(pkslocs,1);
        pkslocs2(j:j+siz-1)=pkslocs;
        yy=abs(pkslocs2-stickloc);
        residual2=sum(yy);
        if residual2<residual
            i0=i;
            j0=j;
            residual=residual2;
        end
    end
end
i=i0;
j=j0;
findpeaks(smooth(y),'MinPeakDistance',i,'MinPeakHeight',minpkheight)
[pks,pkslocs]=findpeaks(smooth(y),'MinPeakDistance',i,'MinPeakHeight',minpkheight);
diff(pkslocs-io);

measured_loc=pkslocs-io;
pkslocs=pkslocs-io;
pkslocs(pkslocs<0)=[];

measured_loc(measured_loc<0)=[];

measured_energy=measured_loc*resolution;

physical_loc=stickloc(j:size(pkslocs,1)+j-1);
physical_energy=physical_loc*resolution;

fitt=polyfit(measured_loc,physical_energy,3);
aa0=fitt(3);
bb0=fitt(2);
cc0=fitt(1);
```

fit only laser-width

```
 lb=[86914,0,0.01];

 ub=[86918,10,0.4];

%lb=86900;
%ub=86925;
T0=1;
```

```
guess = [w0,1,0.12];

fitbarrier=86915;
%Typx=[86916,0.03,1e-2,1e-2,1e-2,0.1];
figure
hold on
%option=optimoptions('lsqcurvefit','MaxFunEvals',1000,'MaxIter',1000,'TypicalX',Typx)
[xx,resnorm,residual,exitflag,output,lambda,jacobian]=lsqcurvefit(@(param,
xdata)absorption_3(param(1),0.0334,0,0,param(2),param(3),fitbarrier,295,0.01,xdata),gu
ess,x,y,lb,ub);
plot(x,absorption_3(xx(1),0.0334,0,0,xx(2),xx(3),86915,295,0.01,x),x,y)
```

fit temp & laser width

```
 lb=[86914,0,0.01,200];

 ub=[86918,10,0.9,400];

%lb=86900;
%ub=86925;
T0=1;
guess = [w0,1,0.04,300];

fitbarrier=86915;

resolution=x(10)-x(9);

figure
hold on
[xx,resnorm,residual,exitflag,output,lambda,jacobian]=lsqcurvefit(@(param,
xdata)absorption_3(param(1),resolution,0,0,param(2),param(3),fitbarrier,param(4),0.173
,xdata),guess,x,y,lb,ub);
plot(x,absorption_3(xx(1),resolution,0,0,xx(2),xx(3),86915,xx(4),0.173,x),x,y)
```

fit temp, pressure & laser width

```
 lb=[86914,0,0.01,200,0.001];

 ub=[86918,10,0.5,400,0.05];

%lb=86900;
%ub=86925;
T0=1;
guess = [w0,1,0.2,300,0.01];

fitbarrier=86915;

figure
hold on
```

```
[xx,resnorm,residual,exitflag,output,lambda,jacobian]=lsqcurvefit(@(param,
xdata)absorption_3(param(1),aa0,bb0,cc0,param(2),param(3),fitbarrier,param(4),param(5)
,xdata),guess,x,y,lb,ub);
plot(x,absorption_3(xx(1),aa0,bb0,cc0,xx(2),xx(3),86915,xx(4),xx(5),x),x,y)
2),xx(3),xx(4),xx(5),xx(6),86915,295,xx(7),x),x,y)
```

Appendix B

Computation of excitation spectrum

```
function y=absorption_3(w0,aa,bb,cc,a,laserwidth,fitbarrier,T,P,x)

kb=1.38064852*10^-23;
m=1.66053904*10^-27*28.010;%mass CO molecule
c=299792458;
y_i=0.74*(295/T)^0.65;

abs(mean(diff(x)));
resolution=abs(x(11)-x(10));

x_new=x(1):0.001:max(x);
res_new=mean(diff(x_new));
x_new=x_new';

x_old=x;

x=x_new;

n=50;


B_x=1.922521;
D_x=6.193*10^-6;

B_B=1.9475;
D_B=6.1*10^-6;

B=B_B-B_x;
D=D_B-D_x;

for J=0:n-1
    Trot_x(J+1,2)=B_x*J*(J+1)-D_x*J^2*(J+1)^2;
    Trot_x(J+1,1)=J;
end

for J_x=1:n
    J=J_x-1;
    values_q(J_x,1)=B*J*(J+1)-D*J^2*(J+1)^2+w0;
    linestrth=1;

    pop=(2*J+1)*exp(-Trot_x(J_x,2)*1.98630*10^-23/(kb*T));
    values_q(J_x,2)=linestrth*pop;
end

values=values_q;

for i=1:size(values,1)
```

```
    if values(i,1)>max(x)
        values(i,2)=0;
        values(i,1)=0;
    end
    if values(i,1)<min(x)
        values(i,2)=0;
        values(i,1)=0;
    end
end

values(all(values==0,2),:) = [];

n=size(values,1);
x_total=x;
xxx=zeros(size(x_total,1),3);
xxx(:,1)=x_total;
x_total=xxx;

x_total=printvalues(values,x_total,1);

valuelocations=find(x_total(:,2));
valuelocatons=valuelocations(:,1);

stick=x_total;
x_total(:,2)=0;


for jj=1:size(valuelocations,1)
    i=valuelocations(jj);
    x=-1500:1500;
    x=x';
    x=x*res_new;
    sizex=(size(x,1)-1)/2;
    sizexx=size(x,1);

    x=x_total(i,1)+x;
    v_av=sqrt(8*kb*T*log(2)/(m*c^2));
    linewidth_doppler=1/2*v_av*values(jj,1);

    v_coll=P*y_i/2;

    y_l=v_coll;
    y_d=linewidth_doppler;
    y_v=0.5346*y_l+(0.2166*y_l^2+y_d^2)^0.5;
    x_1=y_l/y_v;
    y=abs(x-values(jj,1))/y_v;

    total_broad=values(jj,2).*((1-x_1).*exp(-0.693*y.^2)+x_1./(1+y.^2)+0.016.*x_1.*(1-
x_1).*(exp(-0.0841.*y.^2.25)-1./(1+0.0210.*y.^2.25)));

    x_total(i-sizex:i+sizex,2)=x_total(i-sizex:i+sizex,2)+total_broad;
```

```
end


sigma_laser=laserwidth/(2*sqrt(log(2)*2));
laser_y=normpdf(x_total(:,1),x_total(floor(size(x_total,1)/2),1),sigma_laser);
x_total(:,3)=conv(laser_y,x_total(:,2),'same');
x_total(:,3)=x_total(:,3).*a;

x_new=zeros(size(x_old,1),1);
x_new(1)=x_old(1);


i0=max(find(x_old<w0));

res_old=mean(diff(x_old));

x_new(1:i0)=x_old(1:i0);
for i=i0:size(x_old,1)

        if x_old(i-1)<w0+15

            x_new(i)=aa*(i-i0)+bb*(i-i0)^2+cc*(i-i0)^3+(w0);

        else
            x_new(i)=res_old+x_new(i-1);
        end

end

resolution=mean(diff(x_total(:,1)));
xxindexes=round((x_new-x_total(1,1))/resolution)+1;

indexes2=find(xxindexes>size(x_total,1))
xxindexes(indexes2)=size(x_total,1)-1;


y=x_total(xxindexes,3);

y(x_new<fitbarrier)=0;

end
```